Spring 2022

Development of an Interactive Robot for Overground Physical Human-Robot Interaction

Sambad Regmi
Missouri University of Science and Technology

Department: Mechanical and Aerospace Engineering

DEVELOPMENT OF AN INTERACTIVE ROBOT FOR OVERGROUND PHYSICAL HUMAN-ROBOT INTERACTION

by

SAMBAD REGMI

A DISSERTATION

Presented to the Graduate Faculty of the

MISSOURI UNIVERSITY OF SCIENCE AND TECHNOLOGY

In Partial Fulfillment of the Requirements for the Degree

DOCTOR OF PHILOSOPHY

in

MECHANICAL ENGINEERING

2022

Approved by:

Yun Seong Song, Advisor
Ashok Midha
Devin Burns
Douglas A. Bristow
K. Krishnamurthy

PUBLICATION DISSERTATION OPTION

This dissertation consists of the following four articles, formatted in the style used by the Missouri University of Science and Technology.

Paper I, found on pages 16-43, has been published in ASME Journal of Mechanisms and Robotics.

Paper II, found on pages 44-59, has been published in ASME International Mechanical Engineering Congress and Exposition.

Paper III, found on pages 60-87, has been submitted for publication in PLOS One.

Paper IV, found on pages 88-105, is in preparation and will be submitted for publication soon.

ABSTRACT

The overground interactive robots are potentially beneficial for humans in various areas, such as overground rehabilitation therapies and robotic interactive assistance. However, it is unclear what the expectations and challenges are for a robot to be physically interactive with a human during overground tasks, such as a robot helping an older adult walk. To develop such a robot, one must first build a clear understanding of how the human motor intent is communicated when interacting with another agent. Specifically, how do humans understand the leader's intention when being led?

Based on previous works, we hypothesized that humans modulate their arm impedance to measure interaction forces and motion sensitively. To study and test this hypothesis, it was required to measure the arm impedance during the human-agent interaction as precisely as possible and correlate the pattern of change in arm impedance with the pattern of fluctuation of interaction forces and motion. Because the existing interactive robots were not suitable for studying human arm impedance during overground interactive tasks, a new experimental robot – Ophrie – was developed that is capable of performing overground interaction with a human and can also measure arm impedance simultaneously.

Enabled by Ophire, an experiment was designed and conducted where the blindfolded human participants were asked to follow Ophire by holding its interactive handle. Arm stiffness were measured at the moment when A: the participants were compelled to listen to (or sense) haptic information from the robot, and B: when they were not compelled to. We found out that the arm stiffness of the participants at A was significantly lower compared to B. This outcome suggests that, as we hypothesized, the human nervous system modulates the arm stiffness to facilitate effective motor communication during overground physical interaction.

ACKNOWLEDGMENTS

At this point, a cassette tape of the past five years is playing in my head in slow-motion with every fine detail of everyone that has helped me shape this incredible academic journey. I want to thank all for supporting and motivating me throughout this journey.

Dr. Yun Seong Song, you are an amazing advisor. I will forever be indebted to you for your guidance, mentoring, and endless support. Your insightful advice and invaluable feedback have always helped me grow as a better researcher. I feel very fortunate and privileged to have gotten an opportunity to work with you. On a different note, your incredible personality has always taught me how to improve as a human being. Thank you for everything, Dr. Song. I am also grateful to my Ph.D. advisory committee members Dr. Ashok Midha, Dr. Devin Burns, Dr. Douglas A. Bristow, and Dr. K. Krishnamurthy for critically evaluating my research work and providing constructive feedback and suggestions.

Special thanks to all the faculty and staff members at Missouri S&T.

I want to give a huge shout-out to two of my friends: Sreevalsan – my partner in crime, who has always been my inspiration, and Chandreyee, who has always supported and cared for me as an elder sister does. Thank you both. A big thank you to my friends Abdul, Akhilesh, Anilas, Blaine, Devi, Divya, George, Meryem, Sayantan, and Sree Praveen for your efforts and everything you guys have done to make my stay at Rolla memorable.

Binod, Snigdha, sister – Rajani, brother-in-law – Radheshyam, and nephews – Rasik and Rivan, you have never let me feel that I am far from my home. I am indebted to you all. I am also grateful to the Nepali community at Rolla for providing a homely environment.

Nothing would have been possible without the consistent support, the motivations, and the blessings from my grandma – Dhana Kumari Regmi, my parents – Indira Regmi and Shambhu Raj Regmi, and my brother – my life-long friend, and the advocate to my every decision: Samrat Regmi. Hey all, we can proudly say that the dream that we dreamed of together will be true soon. I love you.

TABLE OF CONTENTS

Page

LIST OF ILLUSTRATIONS

PAPER IV

SECTION

LIST OF TABLES

NOMENCLATURE

Abbreviation	Description
AC	alternating current
ANOVA	analysis of variance
CLFLM	closed-loop five-links mechanism
CNS	central nervous system
DC	direct current
DOF	degrees of freedom
ED	effective damping coefficient
EI	effective inertia
EMG	Electromyography
HHI	human-human interaction
1D	one dimensional
Ophrie	The robot for the overground physical human-robot interaction
pHHI	physical human-human interaction
pHRI	physical human-robot interaction
PRBS	pseudo-random binary sequence
RCB	randomized complete block
2D	two dimensional

1. INTRODUCTION

Human communication and language skills have evolved concurrently with the human evolution process [1]. Communication, in general, is a complex phenomenon in which information moves from a sender to a receiver and, in the process, gets encoded and decoded as per necessity [2]. Over time, we, humans, have developed some patterns (or languages) that ensure the effective exchange of information among ourselves for better communication. Some of these languages are in the form of expressions, gestures, symbolic signs, and scripts. We use one or more such language forms to carry out social interaction tasks successfully.

While human communication is primarily studied based on social interaction tasks, it should not be forgotten that humans can communicate even without verbal or visual cues. Communication during physical human-human interaction (pHHI) tasks such as partnered dancing, assisting the elderly to walk, helping babies learn to walk (or even balance), or coordination while moving furniture can solely be performed through contact-based information exchange. Communication through physical interaction is not just limited to within human individuals. Knowingly or unknowingly, in our day-to-day life activities, we tend to accept information from the interacting external environment and make a decision based on the received information. For instance, we tend to stiffen our hands while driving through a rough road; we can walk holding a coffee mug full of coffee without spilling it; we can identify a specific key from a keychain in our pocket with the help of haptic sensing; a blind person can commute from one place to other just with the help of a cane, etc. Unlike pHHI, which is two-way communication, such human-environment interaction involves only one-way communication where the external environment provides some information, and the interacting human accepts it, processes it, and implements a freestanding control strategy; only one of those two interacting partners – i.e., human – is involved in developing and implementing a response action.

Having the external environment interact with the human partner and be actively involved in two-way communication, as we do during pHHI, can have many benefits. For example, if one wants to be replaced by a robot in assisting their elderly family member or wants to be helped to practice dance steps, it would be expected from the interacting robot to read and understand the motor intent of the human and respond similarly to how a human partner would do. Such physically interacting robots can significantly impact our quality of life by serving as robotic nurses, therapists, trainers, and caregivers.

MIT-Manus or phantom haptic interface [3, 4] are a few examples of such robots that are capable of performing physical interaction tasks with humans. These physically interactive robots are only used in seated physical interaction tasks for rehabilitation therapies and research. In addition, these robots can effectively control and modulate the interaction dynamics as per the need. While these robots have well justified their usefulness in the upper arm rehabilitation of stroke patients, other similar treatments, and research, their active involvement in our daily activities has largely been reduced due to their limited overground mobility.

Given that our daily activities involve a lot of overground physical interaction with others, these physically interactive robots could find many applications if brought overground. We, humans, can perform physical interaction effectively and comfortably, and in many cases, we communicate through physical interaction. Collaboration, cooperation, and assisting others are examples of the overground pHHI. Collaboration is an indirect contact-based interaction where two interacting partners execute a motor task independently while being connected through a haptic connection [5]. While during coordination, a motor task is accomplished by the interacting partners where the haptic contact can be direct (such as dancing) or indirect (such as moving furniture). Assistance to the elderly or disabled person and rehabilitation therapies require the interacting partner to maintain haptic contact directly. These interaction activities cannot be performed without effective information exchange. Hence, it would be desired to have a physically interacting overground robot that

can not only control the interaction dynamics but also understand the motor intent of the interaction partner. These robots would also be expected to communicate their motor intent to the interacting human.

What interaction characteristics can be instilled in the overground physically interactive robots to ensure that these robots not only interact but communicate during physical human-robot interaction (pHRI), similar to pHHI? If we know how humans communicate during pHHI tasks, we can replicate the same interaction characteristics in physically interactive robots. Some relevant prior works suggest that communication during pHHI involves the exchange of small forces and hand movements [5–10]. However, it is unclear how these forces and movements are exchanged during physical interaction and how the central nervous system (CNS) interprets this language of force and movements.

Measuring and then analyzing these forces and motions while humans interact can be one of the best possible ways to proceed. These two parameters should not be analyzed separately; these are the cause and effect of each other. Like how current or voltage changes based on electrical impedance in a circuit, a particular system's force and motion characteristics also change based on its mechanical impedance. Mechanical impedance of the human arm can be broadly defined as the overall resistive behavior of the arm to an external disturbance. It can be presumed to be characterized by the arm's effective mass, damping, and stiffness. Hence, analyzing how impedance is modulated during physical interaction can be crucial in understanding how humans communicate through physical interaction.

Human arm impedance has been studied for decades with a primary focus on how humans interact with an external environment and how a freestanding impedance control strategy is developed and implemented by the human nervous system to deal with any external disturbance(s) [11–15]. The pHRI experiments in these studies, in general, followed a standard protocol: a subject would be asked to sit in front of a robot and hold the end-effector of the robot's manipulator, they would be asked to maintain a pose or

follow a trajectory based on the objective of the experiment, their hand (at the interaction point) would be pushed using a force or position perturbation for a specific time at some predefined instant, the force and hand movement data would be recorded, and the impedance (or stiffness) would eventually be estimated using the recorded data and interpreted. A similar experimental protocol can be adopted for the experiment from which we intend to study haptic communication through physical interaction. Since most of the pHHI tasks are performed overground (i.e., not seated, for example, walking), it is beneficial to interpret the relationship between impedance and physical interaction for overground interaction scenarios. In this view, the tools used to measure arm impedance in the experiment protocol mentioned earlier cannot be used readily in their present form because they were designed and developed for seated experiments.

The situation demanded a new tool that can interact with humans – similar to the tools used in the seated experiments – and is also capable of recording parameters required for estimating arm impedance in an overground pHRI setting. Such a physically interactive tool (or robot) has to satisfy some unique characteristics that ensure its capability to measure human arm impedance while interacting with a human partner during an overground pHRI experiment. Our research team envisioned that such a robot could be built by combining two different robots: an interactive arm and a mobile base. A detailed methodology to design a robotic manipulator that satisfies the unique requirements, such as boasting very low endpoint impedance of the manipulator, being able to apply and measure force as low as 1N at the end effector, having a maximum end-to-end speed requirement of 2Hz within the manipulator workspace of 0.15x0.15 m^2, can be found in [16].

To measure human arm impedance using a robotic arm through a prior experiment, it is crucial to make sure that the impedance of the robotic arm itself is very low. Suppose the interaction force and the displacement of the interaction point are used to estimate the impedance – which generally is the case. In that case, the outcome is a shared impedance of the interacting system. If only the impedance of the interacting robotic arm is minimal,

we can conclude that the impedance measured reflects the arm impedance of the interacting subject. To ensure this, even before the prototype was developed, we derived the dynamics of the interactive arm using Euler Lagrange's method. We carried out some simulation experiments in MATLAB to estimate the impedance of the interactive arm itself. The simulation experiment confirmed that an interactive arm built based on our design will have low impedance characteristics. The details were presented in ASME IMECE 2020 and can be found in [17].

It was essential to emphasize the design and development of the interactive arm rather than the lower body when designing an overground robot for the pHRI experiment because the arm is expected to interact with the subject actively. In contrast, the rest of the body is only responsible for housing the necessary mechatronics and ensuring that the arm can be moved from one point to another alongside a human subject. Hence, after carefully designing and fabricating the arm, a mobile robot that can carry the load of both the frame of the robot and the interactive arm was purchased from an outdoor vendor. The mobile robot serves as a base for the entire robot and satisfies the angular and linear velocity requirements. A custom fabricated frame is placed on top of it, on top of which the arm is lodged. The frame was designed to house all the mechatronics – such as the controllers, power supplies, AC/DC converters, motor drivers, and other accessories – required for the mobile base robot and the interactive arm. The fully assembled robot is named Ophrie - the robot for the overground pHRI experiment.

The validation of the robot's aptness for using it in an overground pHRI experiment in a laboratory setting followed. Moreover, the robot's ability to record the parameters required for estimating arm impedance during pHRI tasks, move alongside humans as commanded through angular and linear velocity, and apply commanded force/position perturbation during the interaction was examined. Few pilot experiments ensured that the robot satisfied the last two criteria. Next, an experiment was designed and conducted with an experimental protocol similar to the aforementioned seated experiments and employing

the newly developed Ophire robot to examine the first criterion. This new experiment confirmed Ophrie's capability to record parameters necessary for estimating arm impedance in overground pHRI scenarios.

Estimating arm impedance in an overground pHRI scenario is challenging by itself. While estimating arm impedance during seated tasks, several constraints are generally imposed, such as constraining shoulder movement while maintaining a posture [18]. However, it is difficult to impose restrictions on any body part while performing an overground physical interaction task. In addition, there is no way to find a stable equilibrium point during the interaction, which makes the impedance measurement process more difficult. Because of these reasons, even though the methods used in previous studies for impedance measurements are far more intuitive and have been widely used, they cannot be readily used in overground pHRI experiments.

We proposed a new method to estimate the arm stiffness, especially applicable for overground interaction tasks. The method is well simplified by relaxing the dependency of the arm stiffness to the arm configuration and the direction of the disturbance. In addition, it eliminates the need for multiple trials to estimate arm stiffness. This simplified method helped us analyze the stiffness variation at the different instants of the same trial and the different trials of the same experiment. The details of Ophrie's overall design, the validation experiment, and the arm stiffness estimation method for overground pHRI experiments can be found in [19].

Finally, the experiment designed to test the hypothesis that humans modulate arm impedance to facilitate effective communication during overground physical interaction was conducted in our pHRI laboratory. Blindfolded human participants were asked to hold the end-effector of Ophrie's interactive arm and walk alongside leader Ophire, which was programmed to follow one of the few available trajectories. The end-effector was the only point of communication for the human participants. The trajectories were designed such that the participants would have to listen to the information from the robot's end-effector

(i.e., haptic communication) at some predefined point (let's say A) of the trajectory to follow Ophrie and complete the trial successfully. After they pass point A, they could complete the trial even without further information from the robot. Impedance was measured at point A or any other pre-specified point after point A. A comparison was made on how the arm stiffness varies with the 'need to communicate.' We observed that the stiffness is significantly different when the participants might have felt the dire 'need to communicate' compared to another scenario [20]. Similar observation were reported by Rashid et. al [21] for seated pHRI.

While the recent developments in socially interactive robots are making us more confident about how much more significant these machines can impact our quality of life, we expect nothing less from physically interactive overground robots shortly. Our research is expected to start an open discussion about overground pHRI, and the findings from our study will undoubtedly pave a path for building physically interactive overground robots. In addition, our robot – Ophrie, can serve as a valuable tool for other researchers who are studying overground pHRI and can be modified to be used as a rehabilitation robot for overground therapies such as guided walking therapies.

2. LITERATURE REVIEW

A task as simple as holding a coffee mug or as complex as a cooperative task of helping somebody walk, a human arm can accomplish them very effectively and seemingly effortlessly. To understand how our central nervous system takes care of these tasks so effectively, it is necessary to understand how and why are the task-specific motor commands generated. Does the motor control system have a pattern or a specific model of the arm that allows it to adopt/implement such sophisticated neural strategies?

2.1. MECHANICAL PROPERTIES OF A HUMAN ARM AND ITS RELATION TO MOTOR CONTROL

An upper limb consists of muscles, joints, ligaments, and tendons that collectively play a role in executing a motor control command. Hammond studied electromyographic (EMG) activity in forearm muscles, and the tension developed when externally forced, and found that the motor control behavior is directly related to the underlying physiological change in the muscles [22]. Researchers studied the response of the human arm to the input disturbance through experiments involving postural control tasks and point-to-point hand trajectory tracking tasks [23, 24]. The response was modeled as a second-order linear differential dynamics, and the output impedance was analyzed. The analysis of output impedance during slow trajectory tracking tasks showed that the reflex sensitivity was different when measured before, during, and after the movement [24]. Wadman et al. [25] carried out a fast goal-directed movement experiment to study the position, velocity, and acceleration of the wrist and the EMG activities of biceps and triceps after the movement is externally disturbed. He studied the activation patterns of agnostic and antagonistic muscles with respect to the proprioceptive information available. J. D. Cooke [26] presented an analogy between a simple mass-spring-damper system and the human limb where he indicated that some simple tracking movements in humans might be explained just using

the mechanical properties of the limb. The spring-like properties of the human arm was further underscored from the work of E. Bizzi [27], A. G. Feldman et al [28, 29], W. Abend et al [30], M. H. Vincken et al. [31], etc. Bizzi and the collaborators studied visually triggered head, and arm movements on deafferented monkeys during open-loop reaching tasks [27, 32, 33] and based on those studies, Bizzi proposed the equilibrium point hypothesis (α model) to describe the relationship between muscle force and length. The model suggested that the central motor control specifies a new intended equilibrium point between agonists and antagonists muscles based on the target. Feldman later elaborated the equilibrium-point hypothesis (λ model) for motor control [34] where he discussed the nonlinear spring-like behavior of muscles due to the presence of reflex in addition to the central control mechanism. He explained how the voluntary motor control process could differ from the involuntary process. He proposed three levels of muscle activity regulation that result in arm movement in humans, namely external load, stretch reflex and neuronal central (independent) influence upon the alpha and gamma motorneurons. He further stressed that the independence might be influenced by afferent signals from the muscles, such as force applied. Experiments similar to Feldman's were repeated by Vincent et al. [31]. They concluded that it is mainly reflex activity that determines the stiffness of the effector system. So far, the discussion on the mechanical properties of the effector system and the possible changes in these properties during posture maintenance or point-to-point movements were limited to muscle activation, muscle forces, and the change in the muscle lengths. The focus shifted from muscle level to joint level properties; M. H. Vincken et al. studied whether the motor control system controls the joint properties of the effector system [35]. The apparent stiffness around the elbow joint (invariant characteristics [34]) was estimated from the human experiments where the subjects were asked to move their hand towards the goal as fast as possible. The forearm was constrained to rotate only around the elbow joint. A force pulse was applied every time at some point after the onset of perturbation, and the subjects were instructed 'not to intervene' for the unexpected

force. They found out that the apparent stiffness and the decay of the apparent stiffness are coupled to the movement and thus concluded that the stiffness control is the part of the motor program where a fixed pattern is time-locked to the movement.

The spring-like behavior of the mechanical properties of the human arm as a whole – that is, the dynamics of the entire effector system propagated to the endpoint – was first analyzed by Hogan [36]. The group proposed a method to estimate the stiffness of the multi-joint system for posture maintenance tasks [18]. In their method, subjects were seated with their shoulder restrained and were instructed to maintain an arm posture at predefined positions. The wrist and the palm were bandaged to the apparatus to ensure a firm and rigid connection between the human arm and apparatus. At some point, position perturbation of 5mm or 8mm was exerted at any of the eight pre-specified directions. The force and the displacement data were recorded, and their ratio was obtained – i.e., stiffness. The stiffness of the arm was represented numerically, as a matrix, and graphically, as an ellipse. Their method was based on the previous equilibrium-point hypothesis; the magnitude of the elastic force generated by the arm muscles after the position perturbation depends on the hand's displacement from the equilibrium point.

During the multi-joint arm movements for reaching tasks, CNS specifies the equilibrium trajectory of the movement from the start to the end [29] – that is, the equilibrium point gradually changes over time, and the elastic restoring force will cause it to track the shifting equilibrium position. This also indicates that the mechanical property of the human arm depends on the velocity of the hand at that instant. The validity and implications of the equilibrium trajectory hypothesis in the context of reaching movements were investigated by [37] by simulating a mathematical model of the behavior of the arm tracking the equilibrium trajectories.

Stiffness - the static component of the arm impedance, is indeed the dominant factor in determining the multi-joint arm movement, but what and how do the other mechanical properties contribute? Dolan et al. [38] used a custom-developed testbed to extend the

experiment methodology proposed by [18] to measure the dynamic components of the arm impedance – which are viscosity and inertia. The experiment design was similar to [18] except for some cases in which bias force was present. After the position perturbation was applied, the time-series position and force data were recorded. The recorded force, the displacement, and the displacement derivatives were fitted to the linear second-order differential equation; the dynamics of the entire arm was assumed to be lumped at the human arm endpoint in the horizontal plane and was represented by a mass-spring-damper system. The endpoint mass, damping, and stiffness matrices of the arm model were identified using the recursive least square fitting method [39]. Similar to the arm stiffness representation, which was known to vary depending on the direction of the disturbance and hence used to be represented as ellipse, the mass and the damping were also reported to follow the same trend and were represented as ellipse. A similar method and the findings were also reported by Tsuji and his group investigating the hand impedance in multi-joint movements during maintaining a posture task [40, 41].

The time-varying mechanical behavior of multi-joint arm in humans was investigated by [42] where the pseudo-random binary sequence (PRBS) force perturbation, in contrast to the position perturbation, was applied to the elbow during a catching task. Bennett et al. used similar force input to study the elbow joint mechanical response [43]. Likewise, [44] applied torque pulses to the elbow during voluntary movement. The perturbed displacement was calculated by subtracting the perturbed trajectory with the mean unperturbed trajectory. Bennett used a similar method to calculate the unperturbed trajectory [45]. Unlike the previous method where he used force inputs as a perturbation, Bennett applied position perturbation with respect to the average unperturbed trajectory while investigating the relation between the movement speed and the mechanical properties of the arm. Gomi et al. suggested that the CNS uses the inherent spring-like properties for feed-forward control and is also required to conduct complex inverse dynamics computations [46]. The experiment utilized small force perturbation while the subjects performed multi-joint arm

movement to measure endpoint arm impedance. Burdet et al. pointed out the drawbacks of using existing methods for measuring stiffness during voluntary point-to-point movement tasks [47]. They proposed a method to estimate actual hand trajectory with respect to which position perturbation can be applied to measure arm stiffness in multi-joint arm movement. Because of the difficulty in estimating damping and inertia and their less significant role in human physical interaction and motor control, the investigation of these impedance characteristics has thinned out over time.

Gomi et al. investigated how the impedance behavior changes while interacting with the external environment [48]. They suggested that humans control directional characteristics of hand stiffness. The studies on how the nervous system learns arm impedance modulation to adapt to (or control) the interacting environment followed, such as while performing human-human cooperative task [49], learning to stabilize against external disturbance [11–13, 50, 51], etc. [50] suggested that CNS optimizes arm impedance when exposed to an unfamiliar unstable environment by maintaining large impedance in the direction of instability while maintaining lower impedance in the direction of hand movement. Most of these studies used a least-square or similar method to estimate the mass (inertia), spring (stiffness), and damper (viscosity) properties of the arm by using recorded force and displacement data while a force or position perturbed the subjects. Mainly, they focused on how these properties change to improve the accuracy of the task [51], to learn and adapt to unstable dynamics [11–15], in the presence or absence of visual information, with the magnitude of grasping power [52], etc. Different computational models of the multi-joint arm for movements in a horizontal plane were proposed, and the obtained arm impedance (or joint impedance) were compared (in most cases) with the arm impedance obtained from the actual human experiment [11, 53–56]. Few others that have modeled movement of the arm in 3D include the computational model form [57] and [58].

In contrast to the traditional impedance estimation method where an impulse perturbation is generally applied such as in [18, 46], Davide et al. [59] perturbed arm with a randomized force pulse during movement and used time-frequency analysis to estimate endpoint stiffness. They tried to explain why high stiffness is reported in posture maintaining tasks and low stiffness is reported in movement tasks. Recently, Mark et al. [60] analyzed time-varying joint impedance using kernel-based regression and non-parametric decomposition.

In short, we humans modulate our endpoint impedance to control and adapt to the external environment through changing posture and muscle co-contraction. In addition, the entire human arm can be broadly represented by a lumped mass-spring-damper system (at least for the movement in the 2D plane), and its system parameters – endpoint inertia, endpoint damping, and endpoint stiffness – might be the ones that are being controlled by the central nervous system.

2.2. COMMUNICATION THROUGH PHYSICAL INTERACTION

So far, the review focus has been on the mechanical properties of the human arm; mainly on how it can be represented, how it can be estimated, and how it can be used to explain the learning and adaption behavior of the human nervous system when introduced to disturbances, uncertainties or when asked to learn a novel activity. However, there is a possibility that arm impedance modulation plays a vital role in communication during pHHI activities as well [21].

An interaction is a two-way phenomenon where the information exchange occurs on a give-and-take basis [61]. During overground pHHI, we interact through arms and, meanwhile, should be exchanging some information. Previous research on overground pHHI and pHRI suggested that small forces and motions are exchanged through interactions [8,

62, 63], and it is reported that the arm impedance is relatively low during that process [8]. Hence, the investigation of impedance modulation might provide insight into how motor intent is communicated during overground pHHI tasks.

2.3. APPLICATIONS

Undoubtedly, the characteristics that we try to instill in robots are inspired by how our body works. One of the many examples is the impedance control theory [64]. For decades, it has played a crucial role in shaping and controlling the dynamics between humans and the interacting external environment. This theory revolutionized the control for the industrial robots in several applications like painting, welding, etc. [65].

On the other hand, the robots such as MIT Manus [3], and phantom haptic interface [66] – which were developed for human arm impedance studies in a research setting, and Kinarm [67] – which was developed to measure arm stiffness in monkeys, proved to be a perfect match for rehabilitation therapies, especially for upper arm rehabilitation after stroke.

Rahman and colleagues measured human arm impedance characteristics during the human-human cooperative task and tried to replicate those in a robot [49]. The impedance control approach has also found its usage in teleportation and remote manipulation. In most cases, the real-time human arm impedance (or stiffness) is measured and is replicated in the remote machine [68]. In a different context, handshake in humans was modeled and was replicated in robots by Wang et al. [69].

2.4. DESIGN OF AN INTERACTIVE ARM FOR MEASURING THE HUMAN ARM IMPEDANCE

The interacting arm used for early movement studies employed two links parallel manipulandum similar to MIT Manus [3, 18, 70]. Dolan et al. designed a two-degree of freedom SCARA configuration, direct-drive robot arm [38]. Gomi and the colleagues

developed a closed-loop five-link mechanism with two thin links driven by two wide links, which are eventually driven by two electric motors separately [46]. This manipulandum was widely used afterwards in experiments that involved measuring and analyzing human arm impedance [12, 13, 47, 48, 50, 71, 72]. Beckers and the group also used a similar design but with narrower proximal links [73].

Most of these above-mentioned robotic arms were designed to have thin, rigid, and lightweight links. The mentioned manipulandums have also influenced our interactive arm's design; it is a two-degree of freedom closed-loop five-link mechanism driven by two servo motors. Before finalizing the design, we investigated optimizing the length – and hence mass – of the links based on unique requirements on the interactive arm's workspace and its inherent impedance characteristics [16, 17].

PAPER

I. DESIGN METHODOLOGY FOR ROBOTIC MANIPULATOR FOR OVERGROUND PHYSICAL INTERACTION TASKS

Sambad Regmi, Yun Seong Song

Department of Mechanical and Aerospace Engineering, Missouri University of Science and Technology, Rolla, MO 65401

ABSTRACT

We present a new design method that is tailored for designing a physical interactive robotic arm for overground physical interaction. Designing such robotic arm presents various unique requirements that differ from existing robotic arms, which are used for general manipulation, such as being able to generate required forces at every point inside the workspace and/or having low intrinsic mechanical impedance. Our design method identifies these requirements and categorizes them into kinematic and dynamic characteristics of the robot, and then ensures that these unique considerations are satisfied in the early design phase. The robot's capability for use in such tasks is analyzed using mathematical simulations of the designed robot, and discussion of its dynamic characteristics is presented. With our proposed method, the robot arm is ensured to perform various overground interactive tasks with a human.

Keywords: Physical human-robot interaction, Manipulator design, Effective impedance, Parallel direct drive mechanism

1. INTRODUCTION

Following their success in many industries, robots are now moving to applications that directly affect human movement, such as applications in medicine [1] and healthcare [2, 3]. For example, robots have been applied to the rehabilitation and recovery of movement in stroke patients [4–6] or in medical surgery [3, 7, 8] and have been successful in the past few decades. These more recent applications of robots require them to physically interact with the human body and have further triggered the vision of human-like interactive robots that are capable of safe and effective interaction with humans, even with frail populations.

Imagine a robot helping an elderly person to walk to their day-to-day activities, or a robotic partner helping a person prepare to dance: these human replacements could make a large positive impact on an individual's quality of life. Currently available physical interactive robots cannot readily be used in these overground applications, as they are developed to be stationary for seated rehabilitation programs that are intended for the arms only [4–6]. On the other hand, robotic walking partners can prove their usefulness in enhancing gait balance and postural stability, such as in patients suffering from Parkinson's disease [9]. Such overground physical human robot interaction (pHRI) requires a novel robot with an ability to carry out physical interaction tasks while walking alongside a human.

Despite the potential benefits, it is yet unclear what the expectations and challenges are for a robot to be physically interactive with a human during overground tasks. In order to develop such a robot, one must first understand how humans interact with other humans– epitome for accomplishing physical interaction tasks with or without any verbal and/or gestural information exchange [10, 11]. Therefore, if robots are to replicate the interaction characteristics of humans and hence be used in pHRI, a clear prior understanding of humans-complex biological systems, and their ways of communicating motor intent is needed.

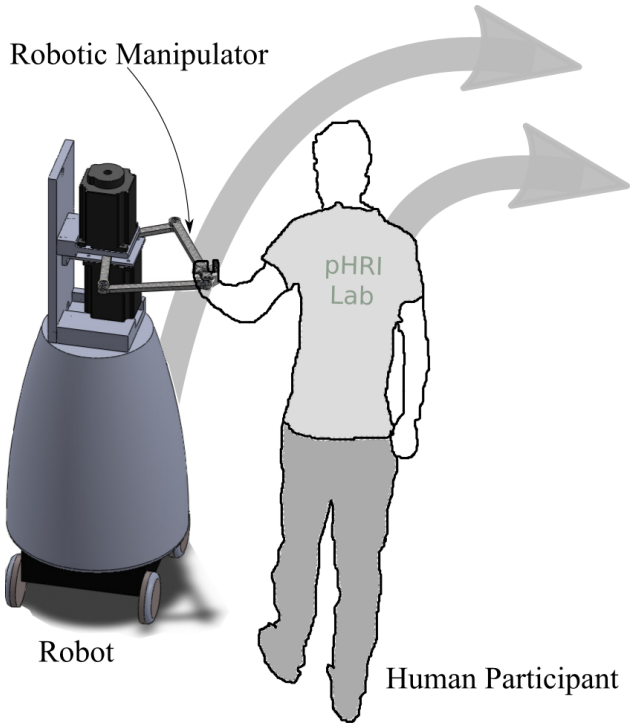

Figure 1. Envisioned pHRI Experiment

What specific human interaction characteristics are we seeking? An interaction is a two-way phenomenon where the information exchange occurs on a give-and-take basis [11]. In many cases, the interaction happens through the arms, through which both power and motor intent is exchanged. Previous physical human-human interaction (pHHI) experiments [12–14] have hinted that arms are used for exchanging motor intent in the form of force and motion during assigned interactive tasks. This view is consistent with an interactive robot controller based on impedance [15] that relates motion to force, rather than considering motion and force independently. Similarly, [16] has suggested the relationship of low arm impedance with interaction tasks through small force. Thus, analyzing the real-time impedance of the human arm during small-force physical interaction may be the first critical step to understand the force and motion exchange attributes during physical interactions.

Unfortunately, the existing interactive robots are not suitable for studying human arm impedance during overground interactive tasks. Interactive robot arms such as the Haptic Masters [17], phantom haptic interface [18, 19], KINARM [5, 20], and MIT Manus [6, 21] are fixed to a specific location and are best fitted for traditional seated interaction experiments [4–6, 11, 13, 19, 21]. On the other hand, mobile robots [16, 22] are not preferable because of their incapability to measure arm impedance of its partner human. Therefore, a new experimental robot is needed that is capable of over-ground interaction and yet is able to measure arm impedance at the same time. We envision that the robot will consist of a wheeled mobile base and a highly interactive arm (see Figure 1), where the former part will only be used for locomotion and does not have to consider small interaction forces or impedance measurement; in fact, several available robotic platforms fulfill the overground mobility requirements and hence can be used for the robot's body. On the other hand, the interactive robotic arm is expected to exchange sophisticated interaction with a human partner. Hence, the majority of the design effort should be focused on the interactive robotic manipulator arm.

This paper presents the unique design procedure for the robotic manipulator arm as part of an overground interactive robot. We present the unique and unconventional static and dynamic requirements of the interactive robotic arm in the perspective of measuring human arm impedance during overground interaction tasks, and thus, present a new design method for physically interactive robotic arm for human arm impedance measurement.

2. DESIGN REQUIREMENTS

The envisioned overground robot will perform as an interactive system to measure human arm impedance during overground physical interaction. Until now, the design requirements for such robots have not been discussed specifically for overground robots, especially when considering small interaction forces. It is clear that one cannot adopt the same design principles that are used for industrial robots, since the application is

vastly different. With our specific goal in mind, we consulted prior literature on stationary interactive robots, light interaction forces, and impedance measurement to devise the unique mechanical design requirements as follows:

2.1. R1: WORKSPACE REQUIREMENT

Interaction characteristics information shared in the 2D ground plane may be analyzed with the help of a 2D plane robotic arm aligned in a plane parallel to the ground. As a start, we will consider interaction in a 2D plane, and hence a 2D plane parallel robotic arm is chosen over a 3D robotic arm as used in many rehabilitation robots [4–6].

The workspace of our robotic arm was chosen to be $150 \times 150\ mm^2$. Based on an earlier work on similar framework (overground pHRI during walking, [22]), the distance between the robot and the human partner varied less than 300 mm, where most of the displacement is due to the human arm length change. This suggests that the robot arm is not expected to change lengths as much as the human arm does. Considering a factor of 50%, the robot arm is expected to move less than 150 mm. Hence, our $150 \times 150\ mm^2$ workspace is expected to be sufficient for our pHRI task, at least as an initial assessment.

2.2. R2: FORCE REQUIREMENT

Our robot must be able to deliver enough force during pHRI. The magnitude of the required force would be comparable to the interaction forces during pHHI, such as in overground walking tasks [14, 16] or social handshake [23]. In these work, interaction forces are typically around 10 N with peak forces around $15 \sim 25\ N$. Hence, we set the requirement that our robotic arm must be able to generate interaction forces in the range of 10 N. In other words, the rated force output would be around 10 N with occasional peak force of around 20 N. The robotic manipulator end must satisfy the minimum force requirement at every point inside the workspace, unlike typical manipulator design, which focuses on satisfying the maximum output force only at certain points.

2.3. R3: ENDPOINT SPEED REQUIREMENT

The robots involved in the experiment must be able to produce a speed that is similar to human arm movement during an interaction. [24] has implied that the frequency range of human arm movement is around 2 Hz. Considering a cycle of a corner to corner diagonal movement with the frequency of 2 Hz, the speed requirement inside the workspace is 0.8485 m/s.

2.4. R4: IMPEDANCE REQUIREMENT

The planar robotic arm must have a low intrinsic mechanical impedance in order to be interactive (back-drivability). This also helps with the human arm impedance measurement, because with low impedance, the robot arm will feel smoother and less cumbersome, and consequently, the human partner will more naturally interact with the robot without artificially stiffening his/her arm. While the apparent mechanical impedance of a robotic manipulator can be reduced by feedback control, it is nonetheless preferable to have low passive impedance to begin with, such as having low inertia or damping.

3. KINEMATIC CONSIDERATIONS

3.1. LINKAGE DESIGN

Manipulators, based on the serial drive mechanism, are more popular than their closed loop chain counterparts because parallel mechanisms are less intuitive to implement due to their complex geometry, nonlinear dynamics, and workspace constraints. However, when considering factors such as high speed, high accuracy, high precision, high acceleration, high stiffness, high load carrying capacity, and/or low inertia, these parallel manipulators may be advantageous over manipulators that are based on the serial drive mechanism [25]. One can find useful examples in various applications: industrial applications such as Hexapods or Delta Robots, medical applications such as the Stewart Platform

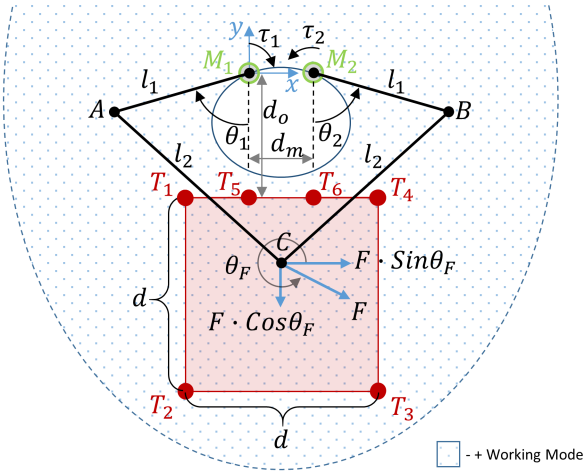

Figure 2. Sketch of the robot arm and its workspace.

for precision surgery, and space application such as satellite trackers for better orientation are just a few examples for these type of manipulators [26]. For our application, a platform manipulator [25] – Closed Loop Five Links Mechanism (CLFLM) – is selected so that, in addition to satisfying planar design requirement in R1, it will also extricate robotic links from carrying heavy motors.

We note that the workspace of the closed loop robotic linkage is smaller than that of similar-sized serial robot manipulators [25, 27, 28]. This is due to the singularities in the closed loop linkage mechanism that restricts the smooth and continuous use of reachable workspace. Despite this workspace restriction, due to the aforementioned advantages and in order to measure small impedances precisely and accurately, parallel manipulators are preferable [25].

First and foremost, the CLFLM has to satisfy the workspace area requirement in R1 that governs the design's final length of the links. Furthermore, the length of the links have to be tailored to their optimal value in order to minimize the inertia. Figure 2 shows a schematic representation of the robotic arm (M_1ACBM_2) with its end effector (C) inside the workspace ($T_1T_2T_3T_4$). Let one motor (M_1) be lodged at the origin represented in the

Table 1. Nomenclature of parameters used in the robotic manipulator

Symbols	Parameters
l_i	Length of a link ($i = 1, 2$)
τ_j	Torque applied by the motors ($j = 1, 2$)
θ_k	Angle made by a link ($k = 1, 2$)
d_0	Distance from the origin to the top of the workspace
d	Length and width of the workspace
F	Force applied on the end effector
θ_F	Angle at which force (F) is applied
d_m	Offset distance between the motors

Note:
- All angles are measured in CCW direction with respect to the positive x-axis.
- Torque convention is positive in CCW direction.

global coordinate system and another motor (M_2) at any other point (X_0, Y_0) in the 2D space. Table 1 includes the symbols for various parameters that are used for the robotic manipulator.

Based on preliminary knowledge of CLFLM and their previous use in human-robot interaction experiments, the following considerations are made regarding the length of the links:

3.1.1. A1: Symmetricity of the Mechanism. The robotic arm should be unbiased with respect to the motor locations. This means that the human must not receive any clues of the end effector's location due to the asymmetry of the design itself. Even parallel manipulators used in industries for pick and place operations generally make use of the direct drive mechanism to justify their two degrees of freedom (DOF) requirement, and they are symmetric as well [29]. In this view, a parallel direct drive mechanism based robotic manipulator that is symmetric with respect to its mid axis between the motors is desired.

3.1.2. A2: Avoid Singularities.

- A2 (a): The workspace defined by forward kinematics does not differentiate various segments of the workspace that are divided by singularities. In [28, 30, 31], the authors have distinguished three different types of singularities – type 1, type 2, and type 3, and [27] has classified the workspace into four different segments inside which the mechanism does not suffer any singularity. Out of four segments in [27], only the working modes "− +" or "+ −" can be used if A1 has to be satisfied. However, larger dexterous workspace can be exploited using mode "− +" than by using "+ −". Hence, choosing the convex pentagon structure (the working mode "− +") yields the largest workspace segment (dotted space in Figure 2) while satisfying A1, and avoiding singularities as well.

- A2 (b): Restricting the internal angle between the crank link and coupler link to be greater than 15° and less than 165° avoids type 1 singularity, whereas imposing the same condition for the angle between coupler links avoids type 2 singularity.

3.1.3. A3: Other Kinematic Considerations.

- A3 (a): Keeping all other parameters constant, the workspace area is inversely proportional to the offset distance between the motors (d_m) (ground link M_1M_2 in Figure 2) [27]. It is thus preferable to have small d_m.

- A3 (b): [32] discussed the advantages of using small crank (proximal link, l_1) in five bar linkages. On the other hand, the small crank to ground link ratio (l_1/d_m) is desirable for favorable mechanical advantage and minimizing inertia [33]. However, A3 (a) discourages the use of the ground link with higher length. Hence, a trade-off between the length of the crank (l_1) and the length of the ground link (d_m) has to be made.

- A3 (c): an arbitrary safe distance (d_0) from the motor to the workspace must be assumed.

In addition to A3 (b), which requires the length of the crank (l_1) to be minimum, minimizing the length of the distal links (l_2) is also crucial in order to decrease the overall inertia of the robotic arm. The method of inequality is deployed to estimate the minimum length of the links. To begin with, the initial approximation of the length of the links is taken from [34]. The approximated length of the links, which is 25 mm for proximal links, and 40 mm, and 45 mm for distal links, are linearly magnified by four times to align with R1. Using the forward kinematics of the robotic manipulator, an iterative process is followed on those magnified lengths, which is 100 mm for proximal links, and 160 mm, and 180 mm for distal links, so as to approximate the appropriate location of the workspace on the 2D plane. The iterative approximation process suggested that the safe working distance (d_0) can be 95 mm (A3 (c)). Given A1, we picked equal proximal links and equal distal links. Considering A3 (a) and A3 (b) during the iterative process helped us approximate the length of the ground link for our robotic arm (d_m) to be 40 mm.

Given that we have the length of the ground link and the safe workspace distance, we can properly specify motor positions and the location of the workspace in a 2D space. The relationship between the length of the links and the location of the workspace can now be represented in terms of inequality.

$$l_1 + l_2 > M_1 T_i \tag{1}$$

$$l_1 - l_2 < M_1 T_i \tag{2}$$

$$l_1 > 0 \ , \ and \ l_2 > 0 \tag{3}$$

To align with the angle constraint on A2 (b), further inequality has to be added:

$$\frac{\pi}{180}15^\circ < \cos^{-1}\left(\frac{l_1^2 + l_2^2 - M_1T_i^2}{2\ l_1\ l_2}\right) < \frac{\pi}{180}165^\circ \tag{4}$$

where M_1T_i is the shortest distance between motor one (i.e. origin) and the different points selected on the boundary of the workspace, where $i = 1, 2, 3, 4, 5, 6$. The former four points represent the four corners of the workspace, and the latter two are chosen such that they fall on the upper boundary of the workspace right below the motors. It is to be noticed that the farthest and the nearest point of the workspace from the origin (i.e. M_1) are respectively T_3 and T_5, and so are T_2 and T_6 respectively from M_2.

Equation 1 through Equation 4 give a total of 26 inequalities – 6 from Equation 1, 6 from Equation 2, 2 from Equation 3, and 12 from Equation 4 – that have to be plotted, and the common region that satisfies all of them has to be identified. Solving the inequality constraints result in the common region with different pairs of the length of links (l_1, l_2). However, if any pair (l_1, l_2) satisfies Equation 4, it eventually satisfies Equation 1 and Equation 2; plotting only the latter two inequalities Equation 3 and Equation 4) will give a set of solutions. The solution that we want among the set of feasible solutions – (l_1, l_2) – is one that satisfies small crank requirement (A3 (b)) as well.

The common solution (see Figure 3) is governed only by the following 4 inequalities (out of 26) and the solution also obtained satisfies all the other 22 inequalities discussed earlier.

$$\frac{\pi}{180}15^\circ < \cos^{-1}\left(\frac{l_1^2 + l_2^2 - M_1T_5^2}{2\ l_1\ l_2}\right) \tag{5}$$

$$\cos^{-1}\left(\frac{l_1^2 + l_2^2 - M_1T_3^2}{2\ l_1\ l_2}\right) < \frac{\pi}{180}165^\circ \tag{6}$$

$$l_1 > 0\ ,\ and\ l_2 > 0$$

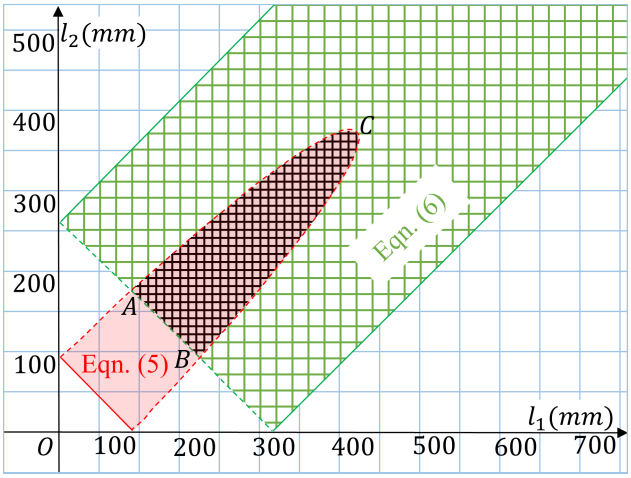

Figure 3. The inequalities plotted in the $l_1 - l_2$ space.

The shaded region ABC in Figure 3 is the common solution, and any pair (l_1, l_2) that falls inside the region meets R1, A1, A2(a), A2(b), A3(a), and A3(c). Considering A3(b), the length of the links $(87.74, 177.51)(mm)$ has to be selected. However, we wanted to have a safe margin to type I singularity, even safer than the constraint proposed in A2 (b), that lead us to choose the length of links to be $(110, 175)(mm)$. The finalized length of the links – proximal links $(l_1) = 110\ mm$, and distal links $(l_2) = 175\ mm$ – are in a comparable range to that of the approximated length of the links after magnification, as mentioned earlier.

It is to be noted that the idea to deploy an iterative process to find the workspace location (d_m and d_0) and then the method of inequality to find the length of the links may not be the only possible and effective way to do so. However, this seems to be a simpler way to obtain the approximate minimum length of the links and the workspace location. Moreover, regardless of how those parameters are obtained, it is to be understood that the overall mechanism has to qualify all the dynamic considerations (as in Section 4) and hence satisfy the impedance requirement (R4). In this view, starting with a simple and intuitive iterative process and using inequalities may be sufficient for our work – especially when the identified length of the links satisfies dynamic considerations as will be shown in Section 4.

In a pursuit to find the approximate minimum length of links and the workspace location with teachings from prior art, the loop closure equation method [35] was also investigated. This numerical iteration technique makes use of equations based on the trigonometric relationship of the mechanism on different configurations. In order to get a unique solution, the number of equations used must be equal to the number of unknowns to be solved. If this is not the case, the difference between available equations and unknowns can be chosen as free choices, as per our design requirements. However, those free choices have to be chosen carefully so that there should be a viable mechanism available with the choices. In our context, we had too many unknowns to be solved using a few equations leading toward many free choices that had to be assumed.

In the aforementioned work that uses the method of inequality, an iterative process had to be deployed even before deploying the method to approximate d_m and d_0. If these two constants in the method of inequality are compared to the free choices in the loop closure equation method, then it should be well understood that the process of picking the free choices itself is going to be computationally difficult and time consuming, even before starting to solve the equations using the loop closure equation method. In addition, being a numerical iteration technique, the variables whose values are sought have to be assumed beforehand and should be in close proximity to the values of the original solution.

With 10 equations and 14 unknowns to solve for our direct drive CLFLM, we were left to pick 4 free choices and 10 initial guesses. It is very difficult to choose 4 free choices that comprise a real mechanism as well as 10 initial guesses that need to be in a close proximity range to their respective real solution. To some extent, this hassle can be minimized by constraining the CLFLM to one DOF system – such as in [35]. However, constraining DOF is not feasible in direct drive mechanisms. Hence, the idea to use the loop closure equation method seems tedious and overly complicates the design process for our direct drive CLFLM robotic arm.

3.2. MOTOR SELECTION

For the end effector to satisfy R2 and R3, the selection of a right motor – based on torque and angular speed – is crucial. This implies that a proper relationship between the linear speed and force requirement of the end effector needs to be converted to the minimum torque and angular speed requirement of the motors, respectively. Moreover, these requirements must be satisfied for each and every configuration defined inside the workspace; unlike industrial robot design, where a specific force is required at a small number of endpoint positions, our robotic arm must satisfy the force and velocity requirements within the whole workspace. This is because human-robot interaction can occur at any given configuration of the robot.

We begin with the kinematic equations:

$$\tau = J^T \ F \tag{7}$$

$$\omega = J^{-1} \ V \tag{8}$$

where $[\tau_1(\theta_1, \theta_2, F, \theta_F) \ \ \tau_2(\theta_1, \theta_2, F, \theta_F)]^T \triangleq \tau$, $J(\theta_1, \theta_2) \triangleq J$, $[\omega_1(\theta_1, \theta_2, V, \theta_F) \quad \omega_2(\theta_1, \theta_2, V, \theta_F)]^T \triangleq \omega$, F and V are torque vector, Jacobian matrix, angular speed vector, external force vector, and linear velocity vector at the effector, respectively.

In order to solve for τ (motor torque required to produce an output force F) and ω (motor angular velocity required to produce end-effector velocity of V) within the entire workspace, it is unrealistic to attempt to find closed-form solutions due to the presence of motor angle (θ_1, θ_2) dependent Jacobian matrix. Instead, a close-enough solution is sought by sampling a finite number of endpoint positions and solving Equation 7 and Equation 8 at these specific points. This notion of selecting a finite number of endpoint positions to form a sampling region is similar to the work with feasible point-to-point trajectories in [30].

131×131 uniformly distributed sample points were chosen from the workspace such that each point represents the combinations of angular displacement of motors (motor M_1 and motor M_2) in 1° increments within their operational range. Considering the length of the links and other parameters (d, d_0, and d_m) obtained in Section 3.1, we determined that the operational range for θ_1 and θ_2 is between 135.6° (end-effector at points T_2 and T_3) and 7.6° (end-effector at points T_5 and T_6). Then, if S_1 and S_2 are sets of angles of θ_1 and θ_2 respectively, each sample point can be identified as the combination of elements from these two sets.

$$S_1 = \{136°, 135°, \ldots\ldots, 6°\} \tag{9}$$

$$S_2 = \{136°, 135°, \ldots\ldots, 6°\} \tag{10}$$

In addition, at any specified point inside the workspace (for example, $\theta_1 = 100°$ and $\theta_2 = 100°$), the torque requirement of the motor is dependent on the magnitude as well as the direction of F, and so is for the angular speed requirement of motor, which is dependent on the magnitude as well as the direction of V. This direction dependency of torque and angular speed necessitates the introduction of the third set (S_3) that addresses the direction of application of specified magnitude of force or velocity at the end effector.

$$S_3 = \{0°, 1°, \ldots\ldots, 359°\} \tag{11}$$

A configuration set S of triples taking each element form S_1, S_2, and S_3 is constructed and is shown in Equation 12. The motor torque(τ) and the angular speed (ω) will depend on which element in set S we are considering with a total of $131 \times 131 \times 359 = 6,160,799$ scenarios.

$$S = \big\{(136°, 136°, 0°), (136°, 136°, 1°), (136°, 136°, 2°), \ldots, (136°, 135°, 0°), \ldots, (6°, 6°, 359°)\big\} \tag{12}$$

3.2.1. Force Requirement. To find the motor torques, given the estimated typical magnitude of F of 10 N (as in R2), using Equation 7 (kinematic equation), an online solver is designed that updates the required parameters in Equation 7 and calculates the torque requirement of the motor for each and every triple in the set S. The output of the solver is a torque matrix T such that the first row constitutes all possible τ_1 values and the second row constitutes all possible τ_2 values (see Figure 2) calculated for each element of the set S.

$$T = \begin{bmatrix} \tau_{11} & \tau_{12} & \tau_{13} & \dots & \tau_{1k} \\ \tau_{21} & \tau_{22} & \tau_{23} & \dots & \tau_{2k} \end{bmatrix}$$

where $k = 6, 160, 799$. Each column of the matrix can be visualized as the torque vector τ that is required to resist/produce F force applied at a specific angle θ_F at the end effector for a specific configuration (θ_1, θ_2) of the robotic arm. The element-wise max norm of the matrix T ($\|T\|_{max}$) gives the torque required for motors that the satisfy minimum force requirement (R2) at each and every point inside the workspace.

3.2.2. Velocity Requirement. Similar to the torque solver, given the maximum magnitude of V of 0.8485 m/s (as in R3), a separate solver is designed that updates the required parameters in Equation 8 and calculates the angular speed requirement of the motor for each and every triple in set S. The output of the solver is a speed matrix W such that the first row constitutes all possible ω_1 values, whereas the second row constitutes all possible ω_2 values for each element of set S.

$$W = \begin{bmatrix} \omega_{11} & \omega_{12} & \omega_{13} & \dots & \omega_{1k} \\ \omega_{21} & \omega_{22} & \omega_{23} & \dots & \omega_{2k} \end{bmatrix}$$

Each column of the matrix W can be visualized as the speed vector ω that is required to produce V velocity at the specific angle θ_F at the end effector for a specific configuration (θ_1, θ_2) of the robotic arm. The element-wise max norm of the matrix W ($\|W\|_{max}$) gives the angular speed required for motors that satisfy the endpoint speed requirement (R3) at each and every point inside the workspace.

The motors' minimum output torque requirement and minimum angular speed requirement based on the force requirement (R2) and the linear speed requirement (R3) were found to be 1.2581 Nm and 401.5697 rpm, respectively. The motor BLY343D-48V-3200-7200SI (Anaheim Automation, Inc.), which has a rated output of 1.4 Nm and a rated speed of 2700 rpm, is chosen.

4. DYNAMICS CHARACTERISTICS

In this section, a mathematical simulation model that resembles the real physical system is developed using the dynamics of the robotic arm in order to observe the mechanical impedance characteristics and thereby scrutinize the robotic manipulator's efficacy in precise and accurate impedance measurement tasks (R4).

Inertial and frictional losses are inevitable in any robotic system. However, when we discuss about very low interaction forces and impedances, reducing these losses as low as possible is strongly preferable. While one can reduce the apparent inertia and damping through feedback control, it is nonetheless preferred to have a low intrinsic (passive) inertia and damping to begin with.

To examine the passive mechanical impedance of our robot arm, we want to analyze the effective inertia (EI) and the effective damping coefficient (ED). The dynamics of a robot is defined by its equations of motion. Since most robotic arms do have complex dynamics, it is often not a necessity to derive such equations unless a robotic simulator model of the manipulator is desired. In some circumstances, such as this work where a

Table 2. Values for parameters used in the robotic simulator

Parameter	Value
Mass of each proximal link of the manipulator	$0.11\,kg$
Mass of each distal link of the manipulator	$0.175\,kg$
Rotor inertia of each motor	$0.00016\,kg\,m^2$
Width of individual link	$0.015\,m$
Inner diameter of the bearings	$0.008\,m$
Outer diameter of the bearings	$0.014\,m$
Frictional damping coefficient (b) of the bearings	$0.0169\,kg\,m^2/s$

Note:
- SMR148 bearings (Boca Bearing Company) are used in robotic joints.
- The frictional damping coefficient (b) of the individual bearing is approximated based on frictional power loss vs rolling speed relationship plots in [36].

robotic simulator is required beforehand to examine its inertia and damping behavior, or sometimes for designing the nonlinear control strategies (such as backstepping controllers and sliding mode controllers), equations of motion are necessary to be derived.

It is a common practice to apply the Euler Lagrangian method to develop the equations of motion of the complex system by using energy equations. All the parameters associated with the robotic arm (such as masses of individual links, frictional damping coefficient, and rotor inertia of the motors) have to be defined beforehand. These parameters for our robotic arm are given in Table 2. The developed coupled second-order equation resembles the standard robotic manipulator equation as given in Equation 13.

$$M(\theta)\ \ddot{\theta} + V_m(\theta, \dot{\theta})\ \dot{\theta} + \tau_r(\dot{\theta}) + G(\theta) + \tau_d = \tau + J^T(\theta)\ \lambda \tag{13}$$

where $\theta(t) \in [\theta_1\ \theta_2]^T$ is the joint space coordinate vector, $\tau(t) \in [\tau_1\ \tau_2]^T$ is the control input vector, $M(\theta(t))$ is the inertia matrix, $V_m(\theta(t), \dot{\theta}(t))$ is the Coriolis/Centripetal matrix, $\tau_r((t))$ are the friction terms, $G(\theta(t))$ is the gravity vector, and τ_d represents disturbances. $J(\theta)$ is the Jacobian matrix associated with the contact surface geometry, and λ (the so-called 'Lagrange multiplier') is a vector of contact forces exerted on the external environment.

Considering an ideal condition, any disturbances ($\tau_d = 0$) will not be taken into account. Likewise, the effect of gravity is also ignored, considering its planer 2D geometry that will be placed parallel to the ground $G(\theta(t)) = 0$.

$$M(\theta)\ \ddot{\theta} + V_m(\theta, \dot{\theta})\ \dot{\theta} + \tau_r(\dot{\theta}) = \tau + J^T(\theta)\ \lambda \tag{14}$$

All the matrices, M, V_m and J, and the vector τ_r, do have complex non-linear terms in them and require the parameters from Table 2 to be substituted in addition to the values of parameters defined in Table 1, which are mostly configuration dependent. All these parameters are already obtained in the previous sections of this paper.

An exception to all known parameters is the frictional damping coefficient for the bearing used, which we estimated using prior work. The friction on a mating surface (ball and bearing's surfaces) in a ball bearing is a function of surface and load applied only, and does not depend upon the system's dynamic characteristics. The friction in the bearing surface, however, is a function of angular velocity as well [36, 37]. Due to the lack of literature on computing friction of deep groove ball bearing, we used the relation established by [36] on the deep groove ball bearing SKF-6205, which has an inner diameter (ID), outer diameter (OD), and width (h) of 25 mm, 52 mm, and 15 mm, respectively. By assuming the maximum rolling speed for our bearing SMR148, the respective maximum bearing friction power loss under zero circumference radial preload (CRP) and no lubrication was obtained. Since the dimension of SKF-6205 bearing does not match with the dimension of our bearing, which has ID, OD, and h of 8 mm, 14 mm, and 3.5 mm respectively, we linearly reduce the result obtained by 16 times. Now the linear relationship between the angular speed and the power loss was exploited to calculate the maximum damping coefficient of the system and is given in Table 2.

The model (as shown in Equation 14) can now be used to study EI and ED of the physical robotic systems. However, since EI and ED depend not only on the configuration (such as S defined in Section 3.2) but also on velocities and accelerations, it is unrealistic to attempt to calculate EI and ED for every possible scenario. Instead, we considered a number of hypothetical, representative interaction tasks and found EI and ED at the initiation of these tasks only. In these tasks, we assume that a human applies a force at a number of initial configurations (details presented hereafter in this section). This can be interpreted as the opposing force the human subject feels when an interaction is initiated on a passive robot arm.

Considering no externally applied torque at the actuators ($\tau = 0$ in Equation 14), we will analyze only the y-component of both EI and ED when a constant force $F = 10\ N$ is applied on the end effector through the center of the workspace ($\theta_1 = \theta_2$) at an angle of 270° CCW with respect to positive x-axis as shown in Figure 4a. In this scenario, due to the symmetricity of the system (A1) and force being applied through its mid axis, the change in position of the links at any instant becomes symmetric, and so is the angle pair (θ_1, θ_2), where $\theta_1 = \theta_2 = 34.29°, ..., \ 102.97°$,(notated as (θ_s, θ_s) here onward) for any configurational geometry in the end effector's path. Even though it does not remove the nonlinearity in the system, it will comparatively simplify the task to analyze EI and ED; it is easier to relate the inertial and damping behavior when they are applied in a specific direction and through a symmetric pathway.

The experimental case designed here is solely a representative experiment and hence, we do not expect them to fetch generalized EI and ED values for entire arm configuration. Nonetheless the respective representative values help us find out the overall effectiveness of the robotic arm. Furthermore, this analysis scenario is likely to happen in the actual HRI experiment as well; during pHRI experiment, we intend to study the process of the

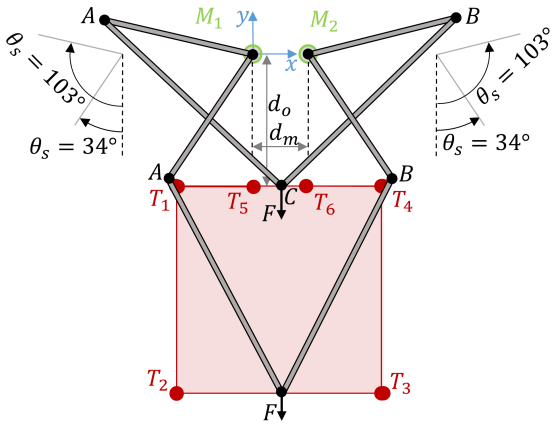

(a) Robotic manipulator at angles $\theta_s = 103°$ and $\theta_s = 34°$

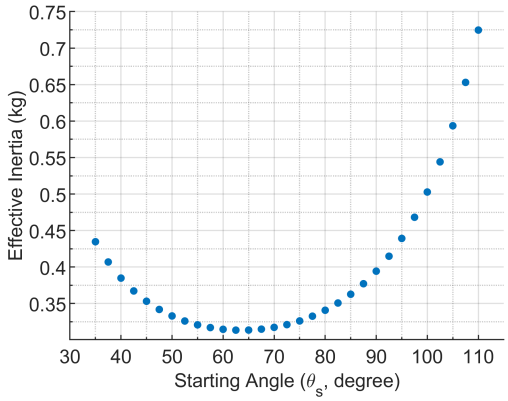

(b) Effective Inertia (EI) vs Starting Angle θ_s

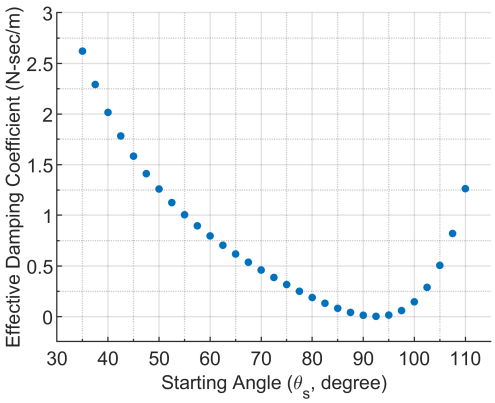

(c) Effective Damping Coefficient (ED) vs Starting Angle θ_s

Figure 4. Mathematical simulation setup and results.

information exchange in a direction aligned parallel to the symmetric mid-axis of the robotic arm. The techniques to obtain EI and ED values for more complex scenarios is discussed in Section 4.1.

Our procedure for estimating EI and ED for an ideal experimental case designed earlier is as follows. For every (θ_s, θ_s), we assume zero initial velocity, apply force F at the end effector, simulate the resulting position, velocity and acceleration during a short time interval, $t = [0, 0.05]\ s$, and then calculate EI and ED based on the linear force-velocity-acceleration relationship observed at this time interval.

In order to estimate EI, we first assume an undamped system where the passive impedance is solely due to the inertia only. Using an ideal undamped robotic arm similar to Equation 15, we select (θ_s, θ_s) configuration, and apply the aforementioned interaction scenario. The EI for the specific configuration was estimated by using linear force-acceleration relationship as given in Equation 16. Repeating the procedure for all individual starting configurations $(\theta_s = 103°, 102°, 101°, \ldots, 34°)$, we found EI as shown in Figure 4b.

Next ED is further estimated as follows. A similar procedure was carried out with a damped simulator system (Equation 14). A separate set of velocity and acceleration data were calculated. We used configuration dependent EI values found previously along with the new velocity and acceleration data to calculate the purely velocity-dependent interaction, from which ED can be estimated using Equation 17.

$$M(\theta)\ \ddot{\theta} + V_m(\theta, \dot{\theta})\ \dot{\theta} = J^T(\theta)\ \lambda \tag{15}$$

$$EI = \frac{F}{a_u} \tag{16}$$

$$ED = \frac{F - EI\ a_d}{v_d} \tag{17}$$

where a_u, a_d, and v_d are accelerations of the undamped system, acceleration of the damped system and velocity of the damped system, respectively, each measured at 0.05 s after the force had been applied on the (θ_s, θ_s) configuration. It is to be noted that the effective damping force for any specific configuration can be calculated by Equation 18.

$$Damping\ Force = ED\ v_d \tag{18}$$

The cumulative mass of the robotic manipulator links at rest is 0.57 kg. In Figure 4b, the range of EI is found to be within an average value of 0.396922 kg with the maximum value being 0.7247 kg. The maximum ED during initiation of interaction is found to be 2.6 $N-s/m$ at 34° starting angle. Taking the maximum velocity to be 0.8485 m/s (R3), the maximum effective damping force that the user will feel during an interaction is estimated to be 2.2061 N . The result shows that the robotic arm will not be too bulky while initiating the interaction and is acceptable for pHRI experiments.

4.1. INTERPRETATION OF THE SIMULATION RESULTS

Some values for ED in Figure 4c are very low, even as low as zero. This suggests that the damping force felt on those specific configurations may be negligible. This may be explained by the fact that some earlier literature have pointed out the existence of negative damping at low velocities [37, 38]. Our approach in estimating EI and ED may not be the most reliable for continuous motions of the end effector. Nonetheless, our approach provides us with reasonable expected values of EI and ED near the center of the workspace which is where most interactions will occur. We used the simulated dynamics to estimate the EI and ED at the initiation of an interaction task, and not during the time course of the interaction task. This was deliberately planned to avoid nonlinear effects that may complicate the analysis. For example, different EI and ED values may be obtained from the same endpoint position if the accelerations and velocities are different, complicating the

interpretation of the result. In fact, our prior, prolonged and extensive attempts on obtaining EI and ED over a continuous longer period of time and displacement was unsuccessful, possibly due to the high complexity of the dynamics.

Earlier in this section, we used a technique to calculate EI, and ED values for ideal representative case designed to simplify the analysis. The technique can also be extended to any general scenarios in order to compute EI and ED values for complex unsymmetrical configurations. Given a point on the workspace, one can apply forces in 2 or more directions and find the 2-by-2 EI and ED matrices as follows.

The Equation 16 and Equation 17 has to be modified accordingly to Equation 19 and Equation 20, respectively.

$$\begin{bmatrix} F_x \\ F_y \end{bmatrix} = \begin{bmatrix} EI_{xx} & EI_{xy} \\ EI_{xy} & EI_{yy} \end{bmatrix} \begin{bmatrix} a_{ux} \\ a_{uy} \end{bmatrix} \tag{19}$$

$$\begin{bmatrix} F_x \\ F_y \end{bmatrix} = \begin{bmatrix} EI_{xx} & EI_{xy} \\ EI_{xy} & EI_{yy} \end{bmatrix} \begin{bmatrix} a_{dx} \\ a_{dy} \end{bmatrix} + \begin{bmatrix} ED_{xx} & ED_{xy} \\ ED_{xy} & ED_{yy} \end{bmatrix} \begin{bmatrix} v_{dx} \\ v_{dy} \end{bmatrix} \tag{20}$$

where $a_{u.}$, $a_{d.}$, and $v_{d.}$ are accelerations of the undamped system, acceleration of the damped system, and velocity of the damped system, respectively in x or y direction, each measured at 0.05 s after the force had been applied at the endpoint at the configuration of interest. F_x, and F_y are the components of force applied in x and y direction, respectively. With 2 force directions and two resulting acceleration vectors, one can solve for the four elements of EI matrix in Equation 19. Then, with two more application of forces and their resulting acceleration and velocity vectors, one can solve for the four elements of ED matrix in Equation 20. One may also choose to apply more than 2 directions of forces to either or both Equation 19, and Equation 20 and apply linear least squares regression to find the elements of EI and ED matrices [39].

5. FUTURE WORKS

Our next step is to build a real physical system based on the design requirements set in this paper. Furthermore, we will continue our work to develop the control strategies required for physical interaction with a human. After the robotic arm is built, we will apply our methods discussed in Section 4 with the built robotic arm as well. It is also of utmost importance to find a proper mobile robotic platform base on top of which the developed robotic arm will be lodged. The base also has to ensure that the function of the robotic arm will not be affected during the overground movement. During the assembly of the arm and the base, proper coordination between them has to be ensured as well. The robotic arm in combination with a mobile robotic platform will be used in our future overground pHRI experiments and expected to be an efficient tool to sufficiently capture human interaction characteristics.

REFERENCES

[1] Presing, B., Hsia, T. C., and Mittelstadt, B., 1991, "A literature review: robots in medicine," IEEE Engineering in Medicine and Biology Magazine, **10**(2), pp. 13–22.

[2] Broadbent, E., Stafford, R., and Macdonald, B., 2009, "Acceptance of Healthcare Robots for the Older Population: Review and Future Directions," International Journal of Social Robotics, **1**(4), pp. 319–330.

[3] Kim, J., Gu, G. M., and Heo., P., 2016, *Robotics for Health Care*, Vol. 9 of Biomedical Engineering: Frontier Research and Converging Technologies, Springer, Cham, pp. 489–501.

[4] Chang, W. H. and Kim, Y.-H., 2013, "Robot-assisted therapy in stroke rehabilitation," Journal of stroke, **15**(3), pp. 174–181.

[5] Dukelow, S. P., Herter, T. M., Moore, K. D., Demers, M. J., Glasgow, J. I., Bagg, S. D., Norman, K. E., and Scott, S. H., 2010, "Quantitative assessment of limb position sense following stroke," Neurorehabilitation and neural repair, **24**(2), pp. 178–187.

[6] Krebs, H. I., Palazzolo, J. J., Dipietro, L., Ferraro, M., Krol, J., Rannekleiv, K., Volpe, B. T., and Hogan, N., 2003, "Rehabilitation robotics: Performance-based progressive robot-assisted therapy," Autonomous robots, **15**(1), pp. 7–20.

[7] Nishihara, S., Sugano, N., Nishii, T., Tanaka, H., Nakamura, N., Yoshikawa, H., and Ochi, T., 2004, "Clinical accuracy evaluation of femoral canal preparation using the ROBODOC system," Journal of Orthopaedic Science, **9**(5), pp. 452–461.

[8] Honl, M., Dierk, O., Gauck, C., Carrero, V., Lampe, F., Dries, S., Quante, M., Schwieger, K., Hille, E., and Morlock, M. M., 2003, "Comparison of robotic-assisted and manual implantation of a primary total hip replacement: a prospective study," JBJS, **85**(8), pp. 1470–1478.

[9] Hackney, M. E. and Earhart, G. M., 2009, "Effects of dance on movement control in Parkinson's disease: a comparison of Argentine tango and American ballroom," Journal of rehabilitation medicine, **41**(6), pp. 475–481.

[10] Knapp, M. L., Hall, J. A., and Horgan, T. G., 2013, *Nonverbal communication in human interaction*, Cengage Learning.

[11] Feth, D., Groten, R., Peer, A., Hirche, S., and Buss, M., 2009, "Performance related energy exchange in haptic human-human interaction in a shared virtual object manipulation task," *World Haptics 2009-Third Joint EuroHaptics conference and Symposium on Haptic Interfaces for Virtual Environment and Teleoperator Systems, Slat Lake City, UT, USA , March 18-20*, IEEE, pp. 338–343.

[12] Stefanov, N., Peer, A., and Buss, M., 2009, "Role determination in human-human interaction," *World Haptics 2009-Third Joint EuroHaptics conference and Symposium on Haptic Interfaces for Virtual Environment and Teleoperator Systems, Slat Lake City, UT, USA , March 18-20*, IEEE, pp. 51–56.

[13] Reed, K. B. and Peshkin, M. A., 2008, "Physical collaboration of human-human and human-robot teams," IEEE Transactions on Haptics, **1**(2), pp. 108–120.

[14] Sylos-Labini, F., d'Avella, A., Lacquaniti, F., and Ivanenko, Y., 2018, "Human-Human interaction forces and interlimb coordination during side-by-side walking with hand contact," Frontiers in physiology, **9**, p. 179.

[15] Hogan, N., 1987, "Stable execution of contact tasks using impedance control," *Proceedings International Conference on Robotics and Automation, Raleigh, N.C, USA, March 31-April 3*, Vol. **4**, IEEE, Raleigh, N.C, USA, pp. 1047–1054.

[16] Sawers, A., Bhattacharjee, T., McKay, J. L., Hackney, M. E., Kemp, C. C., and Ting, L. H., 2017, "Small forces that differ with prior motor experience can communicate movement goals during human-human physical interaction," Journal of neuroengineering and rehabilitation, **14**(1), p. 8.

[17] van der Linde, R. Q. and Lammertse, P., 2003, "HapticMaster–a generic force controlled robot for human interaction," Industrial Robot: An International Journal, **30**(6), pp. 515–524.

[18] Massie, T. H., Salisbury, J. K., et al., 1994, "The phantom haptic interface: A device for probing virtual objects," *Proceedings of the ASME winter annual meeting, symposium on haptic interfaces for virtual environment and teleoperator systems, Chicago, IL, USA, November*, Vol. 55, Citeseer, pp. 295–300.

[19] Salisbury, J. K. and Srinivasan, M. A., 1997, "Phantom-based haptic interaction with virtual objects," IEEE Computer Graphics and Applications, **17**(5), pp. 6–10.

[20] Scott, S. H., 1999, "Apparatus for measuring and perturbing shoulder and elbow joint positions and torques during reaching," Journal of neuroscience methods, **89**(2), pp. 119–127.

[21] Hogan, N., Krebs, H. I., Charnnarong, J., Srikrishna, P., and Sharon, A., 1993, "MIT-MANUS: a workstation for manual therapy and training II," *SPIE Applications in Optical Science and Engineering, Boston, MA, USA, March 26*, Vol. 1833, Telemanipulator Technology, pp. 28–34.

[22] Chen, T. L., Bhattacharjee, T., McKay, J. L., Borinski, J. E., Hackney, M. E., Ting, L. H., and Kemp, C. C., 2015, "Evaluation by expert dancers of a robot that performs partnered stepping via haptic interaction," PloS one, **10**(5), p. e0125179.

[23] Wang, Z., Yuan, J., and Buss, M., 2008, "Modelling of human haptic skill: A framework and preliminary results," *Proceedings of the 17th IFAC World Congress, Seoul, Korea, July 6-11*, Vol. **41**, pp. 14761–14766.

[24] Schaal, S., Sternad, D., Osu, R., and Kawato, M., 2004, "Rhythmic arm movement is not discrete," Nature neuroscience, **7**(10), pp. 1136–1143.

[25] Pandilov, Z. and Dukovski, V., 2014, "COMPARISON OF THE CHARACTERISTICS BETWEEN SERIAL AND PARALLEL ROBOTS." Acta Technica Corvininesis-Bulletin of Engineering, **7**(1), pp. 143–160.

[26] Patel, Y. D. and George, P. M., 2012, "Parallel manipulators applications - a survey," Modern Mechanical Engineering, **2**(3), pp. 57–64.

[27] Campos, L., Bourbonnais, F., Bonev, I. A., and Bigras, P., 2010, "Development of a five-bar parallel robot with large workspace," *Proceedings of the ASME 2010 IDETC/CIE, Montreal, Quebec, Canada, August 15-18*, Citeseer, pp. 917–922.

[28] Alici, G., 2000, "Determination of singularity contours for five-bar planar parallel manipulators," Robotica, **18**(5), pp. 569–575.

[29] Asada, H. and Youcef-Toumi, K., 1984, "Analysis and design of a direct-drive arm with a five-bar-link parallel drive mechanism," ASME Journal of dynamic systems, measurement, and control, **106**(3), pp. 225–230.

[30] Chablat, D. and Wenger, P., 1999, "Regions of feasible point-to-point trajectories in the Cartesian workspace of fully-parallel manipulators," hal-00145125, pp. 1–6.

[31] Bonev, I. and Gosselin, C. M., 2001, "Singularity loci of planar parallel manipulators with revolute joints," *Proceedings of the 2nd Workshop on Computational Kinematics, Seoul, Korea, May 20–22*, Vol. **41**, pp. 219–299.

[32] Basu, P. S. and Farhang, K., 1994, "Kinematic analysis and design of two-input, five-bar mechanisms driven by relatively small cranks," ASME Journal of Mechanical Design, **116**(4), pp. 1108–1114.

[33] Midha, A., Cipra, R., and Farhang, K., 1985, "Analysis and Design of Basic Linkages for Harmonic Motion Generation," ASME Journal of Mechanisms, Transmissions, and Automation in Design, **107**(4), pp. 499–506.

[34] Song, Y. S. and Hogan, N., 2015, "A novel interactive exoskeletal robot for overground locomotion studies in rats," IEEE Transactions on Neural Systems and Rehabilitation Engineering, **23**(4), pp. 591–599.

[35] Midha, A. and Zhao, Z.-L., 1985, "Synthesis of planar linkage via loop closure and nonlinear equations solution," Mechanism and Machine theory, **20**(6), pp. 491–502.

[36] yu Chao, W., yuan Xin, H., Wei, W., and jia Rong, L., 2017, "Frictional analysis of deep-groove ball bearings with varying circumference radial preloads," Advances in Mechanical Engineering, **9**(5), p. 1687814017703895.

[37] Armstrong, B., 1988, "Friction: Experimental determination, modeling and compensation," *Proceedings. 1988 IEEE International Conference on Robotics and Automation, Philadelphia, PA, USA, April 24-29*, Vol. 3, IEEE, pp. 1422–1427.

[38] Quach, N. and Liu, M., 2000, "Friction torque estimation and compensation for robot arms," *Proceedings of the Australia, Conference on Robotics and Automation, Melbourne, Australia, August 30 – September 1*, Citeseer, pp. 211–216.

[39] Flash, T. and Mussa-Ivaldi, F. A., 1990, "Human arm stiffness characteristics during the maintenance of posture," Experimental Brain Research, **82**(2), pp. 315–326.

II. ESTIMATION OF ENDPOINT IMPEDANCE OF A 2D PARALLEL MANIPULATOR USING NUMERICAL SIMULATION EXPERIMENTS

Sambad Regmi, Yun Seong Song

Department of Mechanical and Aerospace Engineering, Missouri University of Science and Technology, Rolla, MO 65409

ABSTRACT

While endpoint impedance of manipulators can be modulated through feedback control, it may not be feasible to reduce it below a certain bound that is dictated by the inherent mechanical characteristics of the robot. In applications where the endpoint impedance of a robot arm needs to be modulated within a large range, it is beneficial to have a method that can estimate the passive characteristics (endpoint inertia and endpoint damping) of the robot arm as early as in the design phase, and use this information to modify the design, if necessary, before building the prototype. In our previous work, we developed a numerical simulation method to estimate 1-D endpoint impedance that is applicable only to limited scenarios. In this article, we present a new numerical simulation method to estimate the 2-D endpoint impedance for any general 2-D manipulators at various locations inside the workspace. We show that our method accurately estimates the endpoint inertia and presents feasible estimates of endpoint damping through numerical simulations. An analysis of the feasibility of using the robot for interaction tasks – based on the obtained impedance characteristics – is also discussed. With our method, robot output impedance can be tailored as early as in the design phase.

Keywords: Endpoint impedance, parallel manipulator, numerical simulation of dynamics, physical human-robot interaction

NOMENCLATURE

l_i	Length of the links (i = 1,2).
τ_j	Torque applied by the motors (j=1,2).
θ_k	Angle made by the links (k = 1, 2).
d_0	Distance from the origin to the top of the workspace.
d	Length and width of the workspace.
F	Force applied on the end effector.
θ_F	Angle, measured in CCW direction with respect to the positive x-axis, at which force (F) is applied.Angle, measured in CCW direction with respect to the positive x-axis, at which force (F) is applied.
d_m	Offset distance between the motors.

1. INTRODUCTION

Robot and human interaction has progressed over time. The progression has demanded the need of physically interacting robots in some situations, if not many, such as the COVID-19 situation in 2020 that has heightened the need for interacting robots to play a role in managing public health and infectious diseases [1]. Such robots have long been the topic of discussion in sectors such as rehabilitation of stroke patients via movement tasks [2] and in the assistance and guidance of the old and/or frail population.

The physical interaction between a robot and a human, similar to human-human interaction (HHI), is usually carried out through arms – in robotics, these are often called robotic manipulators. During HHI, the communication of intent between interacting partners is crucial; the cause and effect in such a process are the information being exchanged and the interaction, respectively. In order to interact like humans do, a robotic manipulator has to communicate its intent as similar as the human arms do. Previous studies on HHI [3–5] have stressed the use of force and motion through arms for physical interaction, which

aligns with the concept of endpoint impedance control [6] – the process of varying the endpoint position in order to obtain the desired force output – in robots. Therefore, during the physical human-robot interaction (pHRI), it is essential to vary the endpoint impedance of the robotic manipulator whenever necessary to accomplish interaction behavior that is similar to HHI.

Endpoint impedance can be regulated from a very small to a very large value with the help of effective control strategies. However, for the stable control output, the lower boundary threshold of the apparent impedance at the end-effector is constrained due to its inherent impedance behaviors such as endpoint inertia (EI) and endpoint damping (ED); the apparent inertia at the end-effector can not be lowered below half of its inherent endpoint inertia [7]. Hence, it is often desired to have a low inherent endpoint impedance in a manipulator to begin with. The stability is determined using control techniques such as the location of pole and zeros, Nyquist plots, etc. In addition, the performance of the interacting robotic manipulator can be rated from the "feel" of the interacting human [7]. And, to achieve better interaction performance, the human-robot interaction not only demands the robot not to provide inadvertent cues that can bias the natural interaction phenomenon, but also requires a lighter manipulator so that it will not be felt bulky during the process of interaction. Since these two measures – hence the inherent endpoint impedance – are directly affected by parameters like inertia, damping, and stiffness, it may be a good idea to estimate the endpoint impedance in the design phase itself, so that we can go back and work on these parameters if deemed necessary before working on impedance control strategies.

Furthermore, estimating the endpoint impedance can be beneficial to cross-validate the safety boundary as well. The safety boundary of the endpoint impedance for a manipulator, that governs the maximum force allowed during human-robot interaction tasks, varies depending on the users' requirement and the type of collaboration environment. Nonetheless, whatever the safety boundary is, it can be crosschecked with the value obtained from the simulation to validate the effectiveness of the developed manipulator.

In our earlier work [8], an experimental robot was designed that is intended to be used for future pHRI experiments that will be carried out in our lab. The robot was built based on the design requirements of the pHRI, and the overall goal was to develop a manipulator that has low passive endpoint impedance (specifically EI and ED). The process of early estimation of characteristics that govern the endpoint impedance of this robot is even critical because it is expected to interact with humans during the pHRI experiment and is supposed to record impedance characteristics of the human arm. Previously, a parallel manipulator was chosen specifically due to its low inherent inertia compared to serial manipulators. The developed robot is a closed-loop five-link parallel manipulator whose end-effector has a predefined workspace area inside which the manipulator is constrained to interact. With that being said, there are a finite but a large set of configurations that the manipulator can pose while retaining the given workspace constraints. In [8], we had developed a numerical simulation model based on the robot's dynamics. We also tried estimating EI and ED for the robot but with some constraints in mind; to make the analysis easier, we constrained the analysis only to the symmetric configuration of the manipulator and when the force on the end-effector is applied along the line of symmetry. As a result, we were able to estimate only a scalar (1-dimensional: 1D) value of the inertia and damping. However, a robot workspace is rarely 1D, and thus a scalar value of EI (or ED) presents only partial information about the robot's endpoint impedance. Because endpoint inertia (or damping) at a point can feel lower in certain directions than in another direction of movement, having a single value of EI or ED presents an incomplete assessment of the robot's true endpoint impedance. In addition, the estimated impedance values were not cross-validated with analytically obtainable terms, such as the endpoint inertia. Hence, our earlier method was limited in its interpretations and applications.

In order to relax the constraints, this article presents and implements a method to estimate 2x2 EI and ED matrices, which was suggested in the same aforementioned work, but was never experimentally scrutinized by analyzing both the symmetrical and asymmetrical

configurations of the manipulator. Our new method presented in this work is for any 2-D manipulators and in any configuration defined by the user. Our method of estimating EI and ED is inspired from the method of estimating human arm stiffness during the maintenance of posture developed by Flash and Mussa-Ivaldi [9], in which human arm stiffness was estimated using multiple-direction perturbation in force and linear regression analysis. The validity of our method was investigated by comparing the EI found using our method with the EI calculated theoretically using the method suggested in [10]. Finally, based on the estimated parameters (i.e. the norm of the EI and ED matrices), the endpoint impedance is analyzed to draw a conclusion on the robot's feasibility in using it for interaction tasks.

2. METHODS

The diagrammatic representation of the closed loop five-link mechanism used for this study is shown in Figure 1. In the figure, $T_1T_2T_3T_4$ represents the Cartesian workspace of the end-effector C of the manipulator M_1ACBM_2. The manipulator is a 2D plane robotic arm actuated by two motors – the first (M_1) at origin and the second (M_2) at (X_0, Y_0) from the origin in the 2D space that is co-planar to the robot plane. The nomenclature for parameters associated with the robot is provided in the nomenclature section and the values for various parameters associated with the parts of the robot is tabulated in Table 1.

The Euler–Lagrangian Method was exploited to come up to a second order equation for robot dynamics and can be molded to take the standard robotic equation form as in Equation 1, which is the function of actuator angles $\theta(t) \in [\theta_1\ \theta_2]^T$ and their derivatives, actuator torques $\tau(t) \in [\tau_1\ \tau_2]^T$ and the external force $F \in [F_x\ \ F_y]^T$ that is applied at the end effector.

$$M(\theta)\,\ddot{\theta} + V_m(\theta,\dot{\theta})\,\dot{\theta} + \tau_r(\theta)\,\dot{\theta} = \tau + J^T(\theta)\,F \tag{1}$$

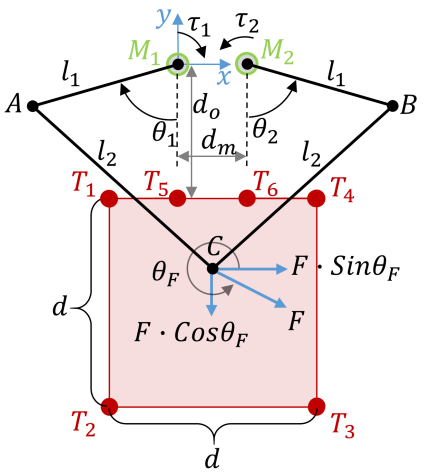

Figure 1. Sketch of the robot arm and its workspace.

where $M(\theta(t))$ and $V_m(\theta(t), \dot{\theta}(t))$ represent the Inertia matrix and Coriolis/ Centripetal matrix, respectively, and $\tau_r(\theta)$ is a vector accommodating friction terms. Equation 1 does not consider the gravity effect(because of the 2D planar geometry of the manipulator) as well as disturbance terms (due to the ideal case assumption) unlike the standard robot equation. $J(\theta)$ is the Jacobian matrix associated with the contact surface geometry.

As stated before, the primary intention of deriving the dynamic equations is to estimate the robot's effective inertia (EI) and effective damping (ED) at the endpoint. This requires transformation of the robot dynamics in Equation 1 from polar form to Cartesian form as in Equation 2:

$$EI\ \ddot{X} + ED\ \dot{X} = F \tag{2}$$

where, X, EI, and ED represent the endpoint displacement in 2D, the effective endpoint inertia matrix, and the effective damping matrix, respectively.

Since EI is the function of manipulator configuration only, using Equation 3, it can be calculated theoretically for any configuration that satisfies the Cartesian workspace constraint of the end-effector [10]. However, ED is the function of motion parameters (i.e. velocity, frictional coefficient e.t.c) along with manipulator configuration as shown in

Table 1. Values for parameters associated with different parts of the robot

Parameter	Value
Mass of each proximal link of the manipulator	$0.11\,kg$
Mass of each distal link of the manipulator	$0.175\,kg$
Rotor inertia of each motor	$0.00016\,kg\,m^2$
Width of individual link	$0.015\,m$
Inner diameter of the bearings	$0.008\,m$
Outer diameter of the bearings	$0.014\,m$
Frictional damping coefficient (b) of the bearings	$0.0169\,kg\,m^2/s$

Note:
- SMR148 bearings (Boca Bearing Company) are used in robotic joints.
- Refer to [8] for the details on how to estimate b.

Equation 4), and hence should be calculated numerically using appropriate experimental techniques:

$$EI = J(\theta)^{-T}\, M(\theta)\, J(\theta)^{-1} \tag{3}$$

$$ED = J(\theta)^{-T}\, [\, M(\theta)\, J(\theta)^{-1}\, \dot{J}(\theta) + V_m(\theta, \dot{\theta}) + \tau_r(\theta)\,]\, J(\theta)^{-1}. \tag{4}$$

As mentioned previously, there are large number of configurations whose endpoint characteristics can be examined while also satisfying the workspace criterion of the manipulator. For this study, a sample set of some configurations were taken into consideration. The uniformly sampled configurations approximately generalize the overall manipulator-workspace combinations. The following section presents the details about the experimental implementation of the numerical simulation model to estimate the manipulator endpoint impedance.

The sketch of an experimental setup is shown in Figure 2. The workspace-manipulator pair in Figure 1 is redrawn displaying different end-effector's positions; in other words, the figure exhibits the initial manipulator configurations in which we want to

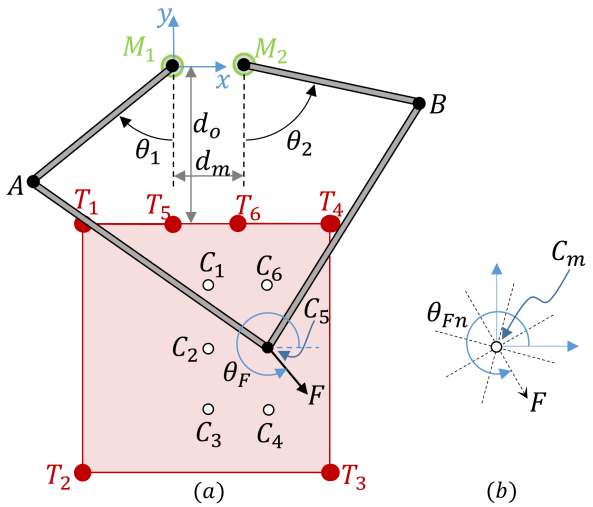

Figure 2. (a) Schematic representation of experimental setup, (b) Direction of force application

estimate the endpoint impedance. The manipulator can now be represented as $M_1AC_mBM_2$, where C_m is the end-effector position. At each location C_m, we carry out 'n' different trials totaling the number of trials in this simulation experiment to be m x n. Let's name each trial as T_{mn}.

For simulation experiment trial T_{11}, the configuration of interest to initiate the trial is $M_1AC_1BM_2$. Now, to begin the trial T_{11}, we start at zero initial velocity, apply a constant force (F) on the end effector at an angle of θ_{F1} (i.e. θ_{Fn} with n = 1) measured CCW with respect to the positive x-axis of the 2D plane, and record the respective motion parameters (position, velocity, and acceleration) for a short interval of time (t = 0.05 sec). A similar procedure can be followed for all T_{1n} trials. After 'n' trials are completed, EI and ED can be calculated for $M_1AC_1BM_2$ configuration.

As mentioned earlier, EI is only configuration dependent. Hence, for this manipulator configuration $M_1AC_1BM_2$, EI_1 (i.e. EI_m with m = 1) can be calculated using Equation 3 without even using recorded data from any of the trials T_{1n}. Now the recorded data ($\ddot{X}$, $\dot{X}$, and F) from all 'n' trials and the recently calculated EI_1 can be substituted to solve the Equation 2 in order to calculate ED_1 (i.e. ED_m with m = 1). It is crucial to understand

that the experiments are conducted in 2D, and hence ED and EI are matrices; Equation 2 is a coupled equation. The method of linear regression can be deployed to solve all the equations (n x 2 equations) obtained by using recorded data from 'n' trials to calculate ED_1 matrix for this configuration $M_1AC_1BM_2$. A similar procedure can be followed for all $M_1AC_mBM_2$ configurations .

In general, for any manipulator configuration $M_1AC_mBM_2$, EI can be theoretically calculated using Equation 3 and can be represented using Equation 5:

$$EI_m = \begin{bmatrix} EI_{xx} & EI_{xy} \\ EI_{xy} & EI_{yy} \end{bmatrix}_m \tag{5}$$

where EI_m represents the endpoint inertia matrix for $M_1AC_mBM_2$ configuration (i.e. when the end-effector is at C_m location).

To calculate ED_m matrix using linear regression, linear force-velocity- acceleration relationship as given in Equation 2 can be used. Expanding and rearranging Equation 2 for 2D experiments, we get Equation 6:

$$\begin{bmatrix} ED_{xx} & ED_{xy} \\ ED_{xy} & ED_{yy} \end{bmatrix}_m \begin{bmatrix} \dot{X}_{xn} \\ \dot{X}_{yn} \end{bmatrix}_m = \begin{bmatrix} F_{xn} \\ F_{yn} \end{bmatrix}_m - \begin{bmatrix} EI_{xx} & EI_{xy} \\ EI_{xy} & EI_{yy} \end{bmatrix}_m \begin{bmatrix} \ddot{X}_{xn} \\ \ddot{X}_{yn} \end{bmatrix}_m \tag{6}$$

where $ED_m = \begin{bmatrix} ED_{xx} & ED_{xy} \; ; \; ED_{xy} & ED_{yy} \end{bmatrix}_m$ represents the endpoint damping matrix for $M_1AC_mBM_2$ configuration, F_{xn} and F_{yn}, $\ddot{X}_{xn}$ and $\ddot{X}_{yn}$, and $\dot{X}_{xn}$ and $\dot{X}_{yn}$ are the components of F, $\ddot{X}$, and $\dot{X}$ in x and y directions, respectively, for the force applied in θ_{Fn} direction. In Equation 6, $\dot{X}$ and $\ddot{X}$ are the vectors that represent the velocity and acceleration of the end-effector, respectively, at 0.05s time after the force is applied on the end-effector of the configuration of interest ($M_1AC_mBM_2$).

In this article, out of many possible manipulator configurations that we could potentially choose, we chose six different configurations, which were represented by six different positions of end-effector C_m (with m = 1,2,. . . ,6) as shown in Figure 2a. These are the configurations in which T_{mn} numerical simulation experiment initiates. Out of these six configurations, three configurations (end-effector at C_1, C_2, and C_3) are symmetric and are aligned vertically on the mid-plane of the workspace. The other three configurations (end-effector at C_4, C_5, and C_6) are offset to the right by 0.0375m. The six configurations in Figure 2a can be represented as (θ_1, θ_2) = {(85.52°, 85.52°), (66.66°, 66.66°), (51.56°, 51.56°), (38.52°, 61.99°), (51.04°, 79.37°), (62.32°, 98.81°)}, each referring to configuration when the end-effector is at C_m = {C_1, C_2, C_3, C_4, C_5, C_6} position, respectively. We assume here that the configuration with same offset to the left produces similar results compared to the offset to the right. Also, we chose the number of trials per configuration to be 8 (θ_{Fn} = {20°, 65°, 110°, 155°, 200°, 245°, 290°, 335°}, with n = 1,2, . . . , 8). The directions of force application for all 'n' trials can be visualized in Figure 2b. In this study, a step input force of 10N is chosen as the external force applied to the end-effector (i.e. F = 10N) that initiates the experiment.

Instead of estimating EI theoretically using Equation 3, EI can also be calculated using numerical experiments as well. To compute EI numerically, the previously designed numerical simulation model needs to be modified to an undamped robotic manipulator's numerical simulation model. Now, similar numerical simulation experiment trials can be conducted and acceleration data can be recorded while simulating this new undamped numerical model. For this undamped system, ED becomes 0 in Equation 2 and hence, Equation 6 can be modified to Equation 7. Deploying the method of linear regression to solve n x 2 equations obtained by substituting acceleration and force data that were recorded from 'n' trials per configuration in Equation 7, EI can be calculated for that

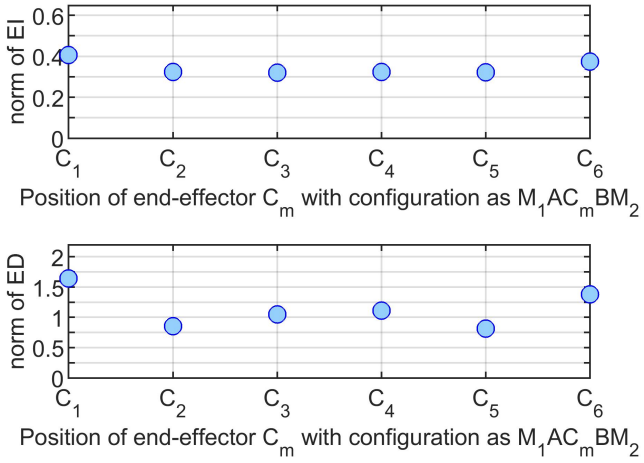

Figure 3. Magnitude of EI and ED for different manipulator configuration when the end-effector "C" is at C_m location

specific configuration:

$$\begin{bmatrix} EI_{xx} & EI_{xy} \\ EI_{xy} & EI_{yy} \end{bmatrix}_m \begin{bmatrix} \ddot{X}_{xn} \\ \ddot{X}_{yn} \end{bmatrix}_m = \begin{bmatrix} F_{xn} \\ F_{yn} \end{bmatrix}_m . \tag{7}$$

This extra work to calculate EI numerically provided us an opportunity to cross-verify the effectiveness of our proposed numerical simulation model as well as the method; that is, the EI obtained from this numerical simulation experiment for the undamped case can be compared to the EI calculated theoretically. The results from both the methods (i.e. numerically and experimentally) are desired to be in comparable range.

3. RESULTS

As discussed previously, and as shown in Equation 5 and Equation 6, EI and ED are 2x2 matrices. In this study, for simplicity, the norm (of the EI and ED matrix) is reported as the magnitude of endpoint EI and ED. The magnitudes for all manipulator configurations considered in this study (i.e m = 6) are shown in Figure 3.

EI estimated using our numerical simulation experiment method and by using the undamped numerical simulation experiment agrees with the theoretical value of the 2x2 inertia (EI_m) obtained using Equation 3; for instance, at C_1, the endpoint inertia obtained theoretically and by using the numerical simulation method were $EI_1 = \begin{bmatrix} 0.3376 & 0 \\ 0 & 0.3976 \end{bmatrix}$ (norm(EI_1) = 0.3976) and $EI_1 = \begin{bmatrix} 0.3415 & 0 \\ 0 & 0.4057 \end{bmatrix}$ (norm(EI_1) = 0.4057), respectively. This suggests that our proposed simulation method accurately estimates the true inertia, which further implies that the ED found using our method is an acceptable prediction of the endpoint damping.

There are two other factors that can affect the end result of the numerical simulation method; first, the choice of directions (θ_{Fn}) and second, the type of force (F) considered in the experiment. With that being said, the satisfactory results with respect to EI as discussed in the previous paragraph were obtained while using force application directions to be θ_{Fn} = {20°, 65°, 110°, 155°, 200°, 245°, 290°, 335°} and the type of force to be step input. In contrast, ramp input of force – in lieu of step input of force – was also examined, keeping all other simulation arrangements the same. The EI estimated using the ramp input of force was offset by a notable amount compared to EI calculated theoretically using Equation 3 and and also numerically using step input of force in the simulation experiment. Likewise, some other different combinations of force application, for example θ_{Fn} = {0°, 45°, 90°, 135°, 180°, 225°, 270°, 315°}, were used while maintaining all other simulation arrangements same. The result in this case had notable offset too.

With reference to Table 1, the total mass of the numerical simulation model is at least 0.57 Kg (when the mass of all the links are added). When the same parameters as given in Table 1 are used in robotic simulator, the average EI of all six configurations is found to be 0.3443 Kg, with maximum EI reaching to 0.4057 Kg for the case when an experiment is started with the end-effector at C_1. Likewise, the maximum ED was found to be 1.6456 N·s/m for the same configuration, $M_1AC_1BM_2$. Considering the maximum velocity of interaction to be 0.8485 m/s [8], the maximum ED the subject will feel when an

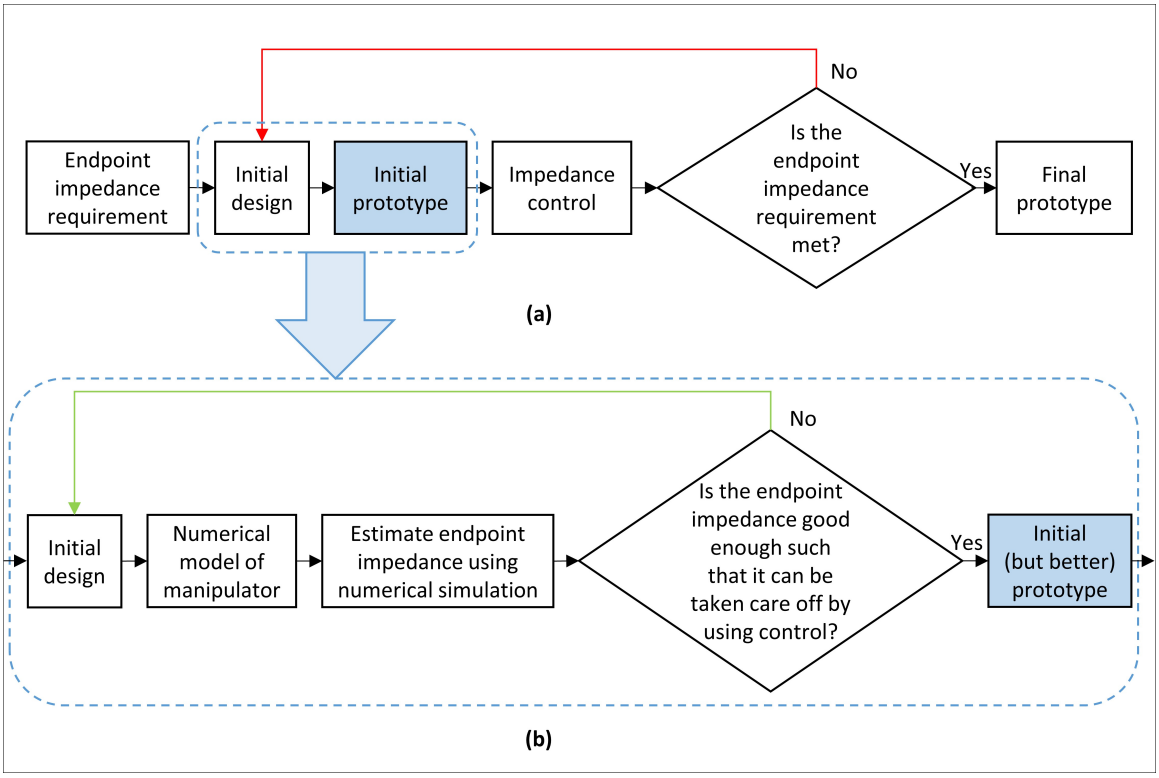

Figure 4. (a) Typical manipulator development process with impedance requirement, (b) Our endpoint impedance method incorporated into the process. The number of costly design loop (red) can be reduced by adding a low-cost design loop (green) enabled by our method.

interaction is initiated is found to be 1.3963 N. The results indicate that the endpoint EI for our robot can go even lower than than the total added mass of the manipulator, which itself is low. The endpoint ED values also seem to be in a reasonable range. This might indicate that the robot will not be felt bulky while initiating the interaction.

The inherent endpoint impedance behaviour based on the estimated EI and ED values is acceptable for human-robot interaction tasks. It should also be remembered that the EI of any robotic manipulator can be further reduced to as low as half of the open loop value (while also maintaining stability), using impedance control strategies [7]. Hence the robot can be considered as a probable candidate for carrying out pHRI tasks.

4. DISCUSSION

While the method employed here in this paper is appropriate, there are a few details that needs to be discussed before coming to a conclusion. First, one can always consider using a greater number of configurations and/or more number of directions of force application. Second, estimation of damping is highly dependent on the estimated b [8], which may not be accurate, since b is non-linear in general. Nonetheless, because the estimated ED seems reasonable, we believe our estimation of b was reasonable as well. Third, during physical experiments, it is difficult to apply step input of force. Physical experiments designed in a similar way to our method may thus give different values than our numerical estimation. The similar analysis for physical experiment involving human subjects will be followed as our succeeding work. Finally, although EI could be calculated using Equation 3, estimating EI using our method still serves an interesting purpose; to determine the best set of parameters and settings (such as the imposed force profile) for the numerical simulations. If the obtained values of EI, after conducting physical experiments (in future), are in comparable range to values obtained from the simulation experiments and also from theoretical calculations using Equation 3, then we can directly use the experimental procedure to analyze the impedance behaviors in the existing manipulators without deriving the complicated dynamics of the manipulator.

On the other hand, instead of considering our method as an integral part of design process, we would like to call it a validation step after an initial design is developed to examine the endpoint impedance of the robotic manipulator. The flowchart in Figure 4a shows a general manipulator development process, which may involve multiple prototype development steps that is both time and cost intensive. On the other hand, the flowchart in Figure 4b represents the development process which incorporates our impedance estimation method. Because impedance estimation can be performed prior to prototype development, our method allows minimizing the number of prototype development. After the robotic manipulator is designed and the parameters such as link lengths, their mass, type and size

of bearings, motors and their rotor inertia etc. are decided, but before the raw materials and parts are purchased, one can run our numerical simulation model and carry out the proposed numerical experiment in order to estimate the EI and ED that characterize the endpoint impedance of the manipulator. If it is found that EI and ED meets your own specification, one can confidently proceed to the fabrication. On the other hand, if one finds out that EI and/or ED is too high for your application, one can go back to the design step. One can repeat this process as much as needed until EI and ED meets the specifications.

5. CONCLUSION

The method to estimate the inherent endpoint impedance, which was proposed in our previous work, and the experimental setup designed and implemented in this article are reasonable. It can be used as a method to cross validate, as early as in the design phase, the effectiveness and the safety of the robotic manipulator to be used in human-robot interaction tasks based on its endpoint impedance characteristics.

REFERENCES

[1] Yang, G.-Z., Nelson, B. J., Murphy, R. R., Choset, H., Christensen, H., Collins, S. H., Dario, P., Goldberg, K., Ikuta, K., Jacobstein, N., et al., 2020. Combating COVID-19 -The role of robotics in managing public health and infectious diseases, March. DOI 10.1126/scirobotics.abb5589.

[2] Krebs, H. I., Palazzolo, J. J., Dipietro, L., Ferraro, M., Krol, J., Rannekleiv, K., Volpe, B. T., and Hogan, N., 2003. "Rehabilitation robotics: Performance-based progressive robot-assisted therapy". *Autonomous robots,* ***15***(1), July, pp. 7–20.

[3] Stefanov, N., Peer, A., and Buss, M., 2009. "Role determination in human-human interaction". In World Haptics 2009-Third Joint EuroHaptics conference and Symposium on Haptic Interfaces for Virtual Environment and Teleoperator Systems, Slat Lake City, UT, USA , March 18-20, IEEE, pp. 51–56.

[4] Reed, K. B., and Peshkin, M. A., 2008. "Physical collaboration of human-human and human-robot teams". *IEEE Transactions on Haptics,* ***1***(2), July, pp. 108–120.

[5] Sylos-Labini, F., d'Avella, A., Lacquaniti, F., and Ivanenko, Y., 2018. "Human-human interaction forces and interlimb coordination during side-by-side walking with hand contact". *Frontiers in physiology,* ***9***, March, p. 179.

[6] Hogan, N., 1985. "Impedance control: An approach to manipulation: Part I Theory; part II Implementation; part III Applications". *ASME Journal of Dynamic Systems, Measurement, and Control,* ***107***(1), March, pp. 1–24.

[7] Buerger, S. P., and Hogan, N., 2007. "Complementary Stability and Loop Shaping for Improved Human–Robot Interaction". *IEEE Transactions on Robotics,* ***23***(2), April, pp. 232–244.

[8] Regmi, S., and Song, Y. S., 2020. "Design Methodology for Robotic Manipulator for Overground Physical Interaction Tasks". *Journal of Mechanism and Robotics,* ***12***(4), August, p. 041002.

[9] Flash, T., and Mussa-Ivaldi, F. A., 1990. "Human arm stiffness characteristics during the maintenance of posture". *Experimental Brain Research,* ***82***(2), October, pp. 315–326.

[10] Hogan, N., 1987. "Stable execution of contact tasks using impedance control". In Proceedings International Conference on Robotics and Automation, Raleigh, N.C, USA, March 31-April 3, Vol. **4**, IEEE, pp. 1047–1054.

III. A ROBOT FOR OVERGROUND PHYSICAL HUMAN-ROBOT INTERACTION EXPERIMENTS

Sambad Regmi[1], Devin Burns[2], Yun Seong Song[1]

[1]Department of Mechanical and Aerospace Engineering, Missouri University of Science and Technology, Rolla, MO 65409

[2]Department of Psychological Science, Missouri University of Science and Technology, Rolla, MO 65409

ABSTRACT

Many anticipated physical human-robot interaction (pHRI) applications in the near future are overground tasks such as walking assistance. For investigating the biomechanics of human movement during pHRI, this work presents Ophrie, a novel interactive robot dedicated for physical interaction tasks with a human in overground settings. Unique design requirements for pHRI were considered in implementing the one-arm mobile robot, such as the low output impedance and the ability to apply small interaction forces. The robot can measure the human arm stiffness, an important physical quantity that can reveal human biomechanics during overground pHRI, while the human walks alongside the robot. This robot is anticipated to enable novel pHRI experiments and advance our understanding of intuitive and effective overground pHRI.

1. INTRODUCTION

Present-day robots can perform specialized and sophisticated tasks around humans. Advancements in robotics technology have improved the robot's interaction with humans, in both social and physical interactions [1–4]. In particular, the development in the understanding of physical human-robot interaction (pHRI) has made a significant impact on how

physically interactive robots can be employed in various aspects of human life [5, 6]. One of the many areas where these interactive machines may find their application is to provide assistance in overground walking. In contrast to those that don't have to interact physically with humans, these robots can always be questioned about their safety, intuitiveness, and effectiveness. For this, it is desired and expected that pHRI robots will have human-like interaction characteristics.

However, it is yet unclear what characteristics to instill in a robot to make it more human-like in overground pHRI. In physical human-human interaction (pHHI), humans do physical interaction solely through haptic-based information exchange even without any verbal communication [7–10]. Whether the contact is directly between humans, such as while dancing or assisting the elderly, or is through an object such as while moving a piece of furniture together, pHHI studies [7, 9–13] suggest that the motor intent is communicated in the form of coupled forces and movements. Other studies have identified human arm impedance modulation to be a key phenomenon during pHHI tasks [9, 10]. Since impedance prescribes the dynamic relationship between forces and movements, these works suggest that the human arm impedance may be related to the motor communication during pHHI and pHRI.

Prior investigations of human arm impedance were focused on identifying its relationship with the motor control strategies of the upper arm in constrained seated pHRI tasks. At first, single joint impedance and muscle mechanical properties were studied using electromyography (EMG) signals [14, 15]. The multi-joint endpoint impedance of a human arm was first experimentally estimated from the recorded dynamic response of the arm after applying position perturbation during a maintained posture task [16]. Since then, the relationship between the modulation of endpoint arm impedance and how the central nervous system (CNS) executes the motor control strategies has been studied in relation to arm stability, learning novel dynamics, reaching tasks, and grasping force [11, 17–27]. In

all these works, robots played a crucial role since they allowed both applying perturbations and recording forces and movements which provided a direct method to measure the human arm impedance.

In this view, a specialized robot capable of measuring and analyzing the dynamics of overground physical interaction is the key to understanding human motor communication during overground pHRI. This robot will be faced with unique conditions and challenges that are not present in seated pHRI studies mentioned above, such as increased kinematic freedom of human arm postures as compared to the fixed posture in [16]. Nonetheless, this robot should also possess the interactive-ness demonstrated by the seated pHRI robots in earlier studies, such as the low output impedance [5, 28] or the ability to provide precise perturbations [16, 17, 29].

To this end, this paper presents (a) the design and implementation of Ophrie – the robot for overground pHRI experiments (Figure 1), (b) an experimental demonstration of the interactive characteristics of the robot during overground pHRI, particularly in measuring the human arm stiffness, and (c) discussion on experimental settings with Ophrie that may affect future overground pHRI experiments. In addition, unique challenges of overground pHRI experiments are presented and discussed in the perspective of arm impedance measurement, which is a potentially impactful application of Ophrie in the near future.

2. MATERIALS AND METHODS

2.1. THE “OPHRIE" ROBOT

The developed overground pHRI robot (Ophrie) consists of an interactive robotic arm and a wheel mobile base – that served the purpose of locomotion (Figure 1). It is expected to exchange interaction information with a human partner via hand, similar to the apparatuses used in seated pHRI experiments [6, 16, 28]. The unique requirements for an overground interaction for Ophrie were identified and discussed in detail in a prior

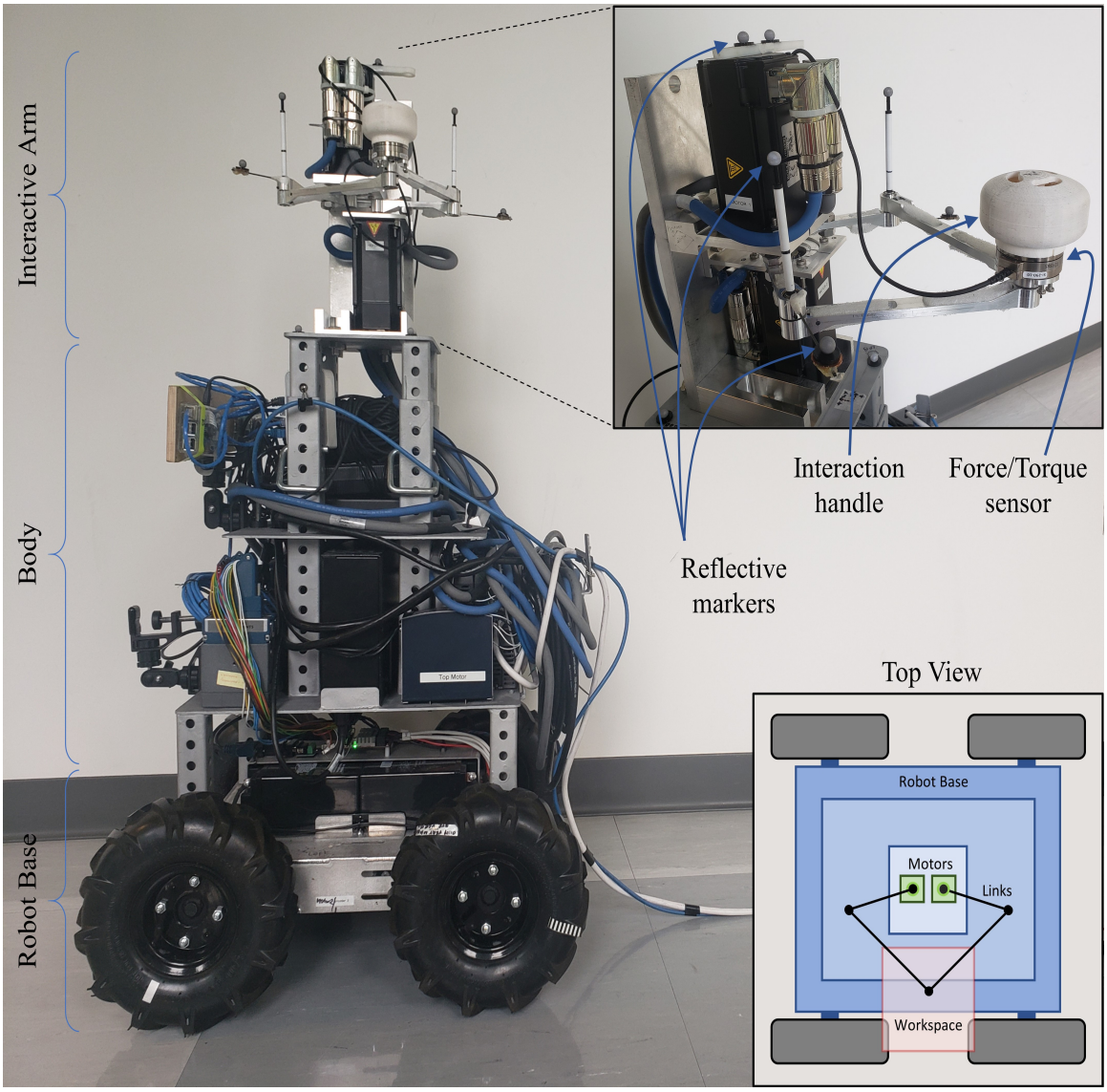

Figure 1. Ophrie robot. The picture of the robot with the interactive arm magnified in the inlet, and the schematic diagram of the top view shown in the bottom right.

work [30]. These include the ability to apply and measure small interaction forces (<10 N) as well as inherently low endpoint impedance. The force requirement was achieved by selecting the appropriate actuators and sensors. The inherent impedance requirement was achieved by incorporating lightweight links and bearings and avoiding gear reductions. In order to verify this requirement as early as in the design phase, a computer simulation model of the robotic arm was developed, and a novel simulation method to estimate the endpoint

impedance of a manipulator was proposed [31]. The feasibility of the designed arm in using it for the pHRI experiment was validated based on the estimated impedance of the robot arm.

A separate mobile robot capable of taking velocity commands was used for the robot base. The robot arm is lodged on top of the mobile base with a custom-made body frame in between for housing the electronics as shown in Figure 1. The body is height adjustable allowing human subjects with varying heights to interact with the robot without discomfort that may arise from height differences. The robot is approximately 100 cm in height, which is smaller than other robots used in overground pHRI studies such as in [12].

2.1.1. Ophrie's Mechatronics System. The interactive arm is a 2D closed-loop five-link mechanism formed by two equal-sized distal links (0.175 m), two equal-sized proximal links (0.110 m), and a ground link (0.040 m). This direct drive 2D mechanism is driven by two servo motors (AKM32E-ANCNAA00: Kollmorgen Corp., VA, USA) placed on either side of the ground link. Each servo motor requires a servo drive (AKD-P00606-NBEC-0000: Kollmorgen Corp., VA, USA) for power supply, encoder feedback, and control. These servo drives are controlled through a central real-time controller (cRIO 9045: NI, TX, USA). A force/torque sensor (mini45: ATI Industrial Automation, NC, USA) is lodged on top of the joint of two distal links at the end of the robotic manipulator. A custom-made interaction handle is placed on top of the sensor as shown in Figure 1. The servo drives and force/torque controller are AC powered, whereas cRIO uses a 24V DC power supply through AC to DC converter. Two additional 24V power supply modules (PS-16: NI, TX, USA) are required to provide the logic power to the servo drives. All these mechatronics units are placed on the robot's body and are powered by an external AC source via wire. The mobile base is a four-wheel differential drive robot (IG52-DB4 Heavy duty chain and sprocket kit: SuperDroidRobots, NC, USA). A 12V DC supply powers it

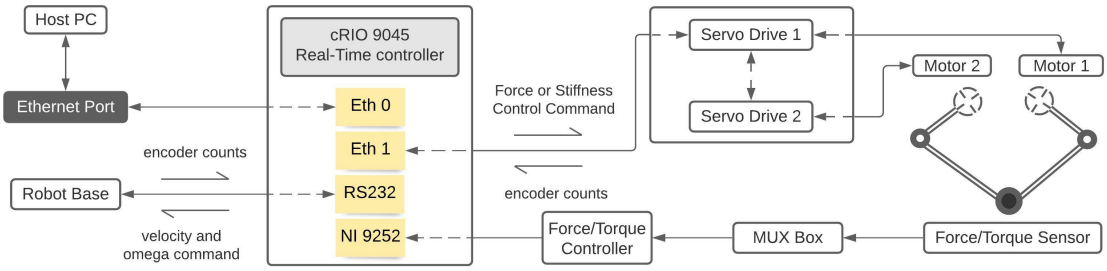

Figure 2. The flowchart for Ophrie's mechatronics system.

through two rechargeable lithium-ion batteries seated on top of its frame. It is controlled using a micro-controller (RoboClaw 2x30A: Basicmicro Motion Control, CA, USA) which ultimately receives the command from the central controller.

The central controller is a central processing unit. It communicates with servo drives through a master-slave EtherCAT protocol and the base micro-controller through RS-232 serial communication protocol. It also accepts analog voltage data from the force sensor via force/torque controller (ATI Industrial Automation, NC, USA); a C-series module (9252 voltage input module: NI, TX, USA) is required to input voltage data to the controller. For monitoring the health of the force/torque controller, a separate digital input-output module (9401 module: NI, TX, USA) is required. Figure 2 shows the flowchart for Ophrie's mechatronic system.

LabVIEW programming language (LabVIEW 2018 with SoftMotion and Real-Time module: NI, TX, USA) is used to deploy the commands to the central controller from the remote computer. The designated computer and the real-time controller (on the robot) are connected through Ethernet maintaining the same subnet mask.

2.1.2. Data Acquisition. To study the interaction dynamics during a pHRI experiment, it is essential to measure and record the interaction forces at the end effector as well as the subject's hand location kinematics. The forces at the end effector can be measured with respect to the force sensor axis and can later be transformed into the robot axis using an

appropriate rotation matrix. The motor position can be recorded using a single-turn absolute Biss sine encoder (2048 LPR) embedded in the servo motors. The point of interaction, which is the end of the manipulator or the hand position, can be calculated from the motor positions by using the forward kinematics of the robotic arm. The data are recorded with a sampling rate of 1kHz.

When necessary, the arm length – as presented in section 'OBSERVATIONS FROM OPHRIE-HUMAN INTERACTION' – can be obtained from the Vicon motion capture system (Vicon Motion Systems Ltd., Oxford, UK). For this purpose, reflective markers can be placed in the hand and the shoulder. This data is then be processed afterward using Vicon Nexus and Vicon PorCalc Software. The sampling rate of the Vicon system is 200 Hz.

If the Vicon data were used for the analysis, the data from the robot was decimated to 200Hz before combining the two data. Then, the angular position provided by the motor encoders was compared with the respective position obtained from the Vicon system, which is estimated with the help of 6 reflective markers attached to the robot arm (see Figure 1).

2.1.3. Robot Control. The robot arm can be programmed to provide force or position modulation with PID control with 1 kHz. The robot can also provide force perturbations (<10 N) when needed. The position modulation can be used to provide a spring-like background force field towards the center of the workspace such that the handle position (and thus the human hand position) is kept away from the edges of the workspace. This background stiffness can be low (e.g., 50~100 N/m) to allow smooth interaction with the user. Having this background stiffness is particularly important for an overground robot because, unlike in most seated pHRI tasks, it is very easy for the human user to move the handle outside the robot arm's workspace. Sufficient yet gentle background stiffness is thus crucial to help the endpoint of the robot arm to remain within the workspace during overground pHRI tasks.

The robot base is independently controlled and takes an input command of linear and angular velocity. The quadrature encoder reading from the motors of the robot's rear wheels is used for determining the instantaneous position, which later can be used for velocity control of the robot. The iteration rate for base control was 40 Hz.

2.2. VALIDATION EXPERIMENT

Ophrie robot's ability to perform pHRI experiments and measure the dynamics of the interaction was validated with an experiment. Specifically, the pHRI experiment addressed Ophrie's ability to apply force perturbations to human hands and measure the resulting kinematics during overground pHRI. In addition, the experiment sought to investigate the effect of experimental conditions, such as human behavior, and robot settings in this specific pHRI experiment and suggest desired robot settings for future pHRI experiments.

A crucial and necessary feature of the robot is to allow arm stiffness estimation during overground pHRI tasks. To do this, Ophrie is designed to apply force perturbations and measure the hand displacement, similar to the methods used in [19, 32]. The procedure is described later in the section 'Experiment Procedure' and the more detailed discussion can be found in the section 'OBSERVATIONS FROM OPHRIE-HUMAN INTERACTION'.

The robot settings may affect the interaction dynamics of the overground pHRI. Different levels of the perturbation force and the background stiffness of the robot (as explained in the section 'Experiment Procedure') may affect the measurements. In addition, the experimental protocol may affect human behavior during pHRI, such as the availability of vision. The effects of these settings and conditions were tested in the proposed overground pHRI experiment.

2.2.1. Subjects. A total of 5 healthy young adults (3 male and 2 female, 27.4±1.817 years) without any self-reported neurological disorder took part in the study. Subjects signed a written consent form before participating in the experiment. The research protocol was approved by the Institutional Review Board of the University of Missouri System.

2.2.2. Experiment Procedure. The experiment was designed to have twelve different cases defined by the various combinations of the following three variables: (a) visual condition (eyes open or eyes closed), (b) the background stiffness level of the robotic arm (50 N/m, 75 N/m, or 100 N/m), and (c) the level of force perturbation (3 N or 5 N). Trials were performed in four blocks, each randomly arranging the twelve cases mentioned above. The total number of trials per subject was 48. In this study, Ophrie acted as a leader, considering the complexities that have to be dealt with when the robot acts as a follower (see the section 'OBSERVATIONS FROM OPHRIE-HUMAN INTERACTION').

After necessary preparation for motion capture, subjects were detailed about what was expected from them during the experiment. The robot's height was then adjusted to align the interaction handle to the subject's elbow level. Subjects were informed that the robot would stop if the interaction handle goes out of the workspace – a 0.15x0.15m^2 region inside which the subjects were asked to keep the hand while interacting with the robotic arm. The presence of the background stiffness helped with this. The level of background stiffness differed for different trials based on experiment design. At the beginning of each trial, the subjects were asked to stand upright next to Ophrie by holding the interaction handle (see Figure 3). Subjects were informed whether they had to keep their eyes closed or open for the upcoming trial and then were asked to shake the handle three times in the y-axis (see Figure 3) for data synchronization purposes. The process was followed by activating the background stiffness controller; it positioned the robotic arm to the center of the workspace. Subjects were asked to relax the arm and let Ophrie position its interaction handle to the center of the workspace during this process. Lastly, they were asked to start walking alongside Ophrie, as shown in Figure 3. The robot was programmed to maintain a constant linear velocity of 0.5 m/s throughout the 5.7 m straight-line trajectories. At the midway of the trajectory, the robot applied a force perturbation (1 second) in the axis perpendicular to the robot's movement direction and towards the interacting subject (- y in Figure 3). The stiffness control loop was disabled and replaced by the force controller

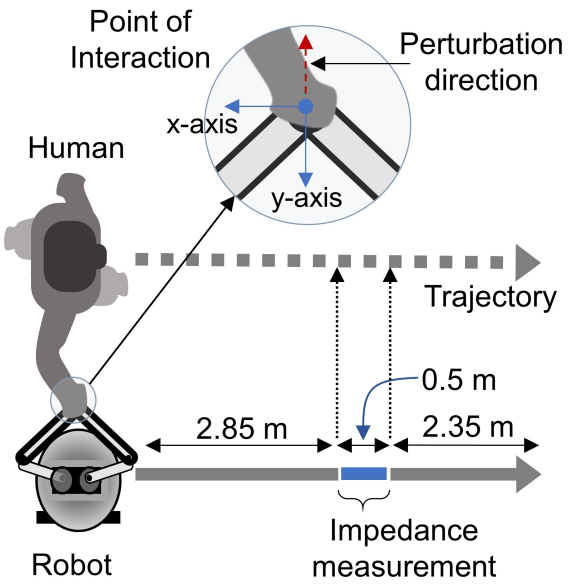

Figure 3. Schematic of the overground pHRI experiment.

during the perturbation. For each trial, the amount of force perturbation was different. The magnitude was determined by adding (i) the interaction forces due to the background stiffness control at the instant when the perturbation was to be applied and (ii) the level of perturbation commanded (i.e., 3 N or 5 N). Subjects were asked to follow the robot with a relaxed arm throughout the entire trial except during the perturbation period in which they were asked to keep their hand within the workspace of the robot arm. Each trial took approximately 20 seconds.

For each trial, the manipulator's endpoint position (which is identical to the human hand position), the manipulator's endpoint velocity (which is identical to the human hand velocity), and the interaction forces between the robot and the human hand were obtained. The endpoint position and forces were measured directly from the motor encoders and the force sensor, respectively. The velocity was obtained from the position data after applying the second-order Butterworth low-pass zero-lag filter with 40 Hz cutoff frequency using Matlab (The MathWorks Inc., MA, USA).

2.2.3. Estimation of the Arm Stiffness. From the obtained forces and kinematics, the interaction dynamics can be estimated. For initial validations, this work used one of the simplest and widely used models, which involves passive, linear, and time-invariant second-order dynamics, such that:

$$f - f_0 = m\ (\ddot{x} - \ddot{x}_0) + b\ (\dot{x} - \dot{x}_0) + k\ (x - x_0) \tag{1}$$

where f is the interaction force measured after the perturbation onset and x, $\dot{x}$, and $\ddot{x}$ are the position, velocity and acceleration of the interaction point after the perturbation, respectively. m, b, and k are the endpoint impedance parameters namely inertia, damping and stiffness, respectively [33–35]. Here, m incorporates the inertia of both the human arm and the interaction handle, whose mass is (~0.05 kg). x_0, $\dot{x}_0$, and $\ddot{x}_0$ are the mean hand position, velocity, and acceleration of the interaction point just before the perturbation, respectively. The data of 0.1 second window before the perturbation onset was used for averaging and are used as the operating point from which all deviations are measured. For simplicity, only the kinematics in the direction of the force perturbation are considered, such that the parameters m, b, and k as well as the kinematics x, $\dot{x}$, $\ddot{x}$, x_0, $\dot{x}_0$, and $\ddot{x}_0$ are scalars.

The measured kinematics and forces were fitted on the Equation 1 using Matlab fitlm function to estimate m, b, and k. The intercept was constrained to zero to match the linear model in fitlm with Equation 1. Otherwise, default settings were used such that modelspec was set to linear and the observation weights were set to one. The stiffness value (k) was the main outcome of interest, while the inertia (m) and damping (b) values were used to verify that the regression result was acceptable (e.g., both m and b are positive and realistic). This regression method is similar to the ARX model regression used in [35]. Further details and justifications can be found in the discussion section 'Assumptions and Challenges', and in the supplementary material. Lastly, the equilibrium point for each trial was obtained by

applying the estimated m, b, and k values into Equation 2, which represent the interaction dynamics just before the perturbation:

$$f_0 = m\,\ddot{x}_0 + b\,\dot{x}_0 + k\,(x_0 - x_{eq}) \tag{2}$$

where x_{eq} is the position of the equilibrium point of the hand.

2.2.4. Statistical Analysis. The experiment was conducted in four blocks with a randomized complete block (RCB) design. Each trial from the experiment produced one scalar stiffness value along the axis of the perturbation (y-direction, see Figure 3), which was always perpendicular to the robot movement. Out of 240 trials across all subjects, five trials that resulted in a negative stiffness and one other trial whose data was lost due to exporting error were discarded. From the remaining data, outliers – defined as the values three times the inerquartile range past the 25^{th} and the 75^{th} quartiles – were screened out using JMP statistical software (SAS Institute Inc., NC, USA). There were a total of 3 outliers that were excluded from further analysis. The effects of the robot settings (background stiffness level and the magnitude of the perturbation force) and the effect of the experimental condition (eyes open/closed) were tested on the remaining 231 trials using ANOVA (JMP statistical software). The hypothesis was that the robot settings do not affect the overground pHRI dynamics, but the availability of vision affects the human response and alters the overground pHRI dynamics. A significance level of p = 0.05 was used.

3. RESULTS

All subjects successfully completed all 48 trials without fatigue or safety concerns. They quickly became accustomed to the protocol. There were no noticeable obstructions to the experiment due to the hesitance or reluctance of the subjects.

As explained in the section 'Experiment Procedure', the background stiffness is present during the entire trial except when the perturbation is applied. The average interaction force of all the subjects and all trials due to background stiffness just before the perturbation was observed to be 2.063±1.108 N at 0.746±1.529 rad counterclockwise from the interacting subject's mediolateral direction (i.e., - y in Figure 3). That is, on average, the subjects were pushing the robot away from their trunk at approximately 2 N of force. This force is similar to the interaction force between two humans in a similar task to this study (overground walking while holding a sensor together) [36] and lower than the interaction forces between two humans while walking side-by-side on treadmills [37].

The participants' hand positions before the onset of the perturbation were near the origin of the workspace as seen in Figures 4, and 5B and D. The hand velocity was nearly zero at the onset of the perturbation (Figures 5A and C). A typical pattern was observed in the hand velocity time series in almost all trials of all subjects. Shortly after the force perturbation onset, the hand velocity along the y-direction decreased as the hand was pushed away from the robot until it reached a negative peak. Then the velocity increased towards the robot until it passed zero and reached a positive peak at around 250~450 ms after the onset of the perturbation. We did not observe any noticeable pattern across trials after the second peak, but this pattern of negative-to-positive peaks was present in all trials in all subjects. For example, for a trial of subject 5, the interaction force, handle displacement, and the velocity after the perturbation onset is shown in Figure 6. For this specific trial, the second peak of the velocity was at 274 ms (Figure 6C). The average time of the second peak of all the trials was observed to be 335.646±81.676 ms for all subjects.

This pattern resembles the velocity response of a passive second-order system given a step input. Thus, we hypothesize that the period between the onset of the perturbation to the second peak of the velocity contained the passive dynamics and can be used to analyze the interaction dynamics (Equation 1). The interaction dynamics were estimated using linear regression as discussed in the section 'Estimation of the Arm Stiffness'. The estimated

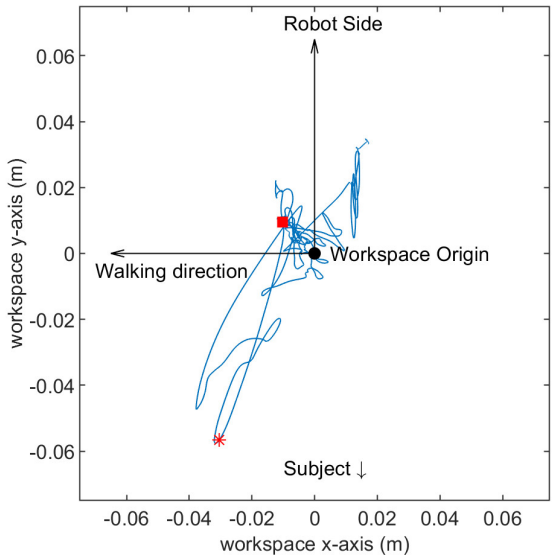

Figure 4. The trajectory of the interaction handle/hand in 2D for a representative trial performed by subject 5. Red square represents the instant when force perturbation initiated, and the red star represents the handle/hand position after 200ms of the perturbation).

stiffness was found to be 235.255± 113.581 N/m, 199.893± 92.442 N/m, 174.958± 97.043 N/m, 149.107± 67.358 N/m, and 123.195±63.871 N/m, respectively for subjects 1 to 5. Since the robot arm does not have inherent stiffness elements, this stiffness may be interpreted as the stiffness of the arm of the human user. Indeed, the values were comparable with the arm stiffness reported in the previous seated experiments [22, 34]. The average of inertia estimated from all 48 trials of all the subjects was found to be 0.473±0.249 kg. The average damping was observed to be 3.270±4.741 Ns/m. The low positive values of inertia and damping were as expected since the combined inertia and damping of the robot arm and human arm would not be very high. The inertia, damping, and stiffness estimated for all 48 trials performed by subject 5 are plotted in Figures 7A, B, and C, respectively. In addition, the equilibrium point of the participant's arm per trial was also estimated. On average, the equilibrium point was 0.031±0.031 m away from the center of the manipulator workspace towards the robot. The mean and standard deviation of the R^2 values of the estimated dynamics of all 48 trials for each subject were 0.521±0.083

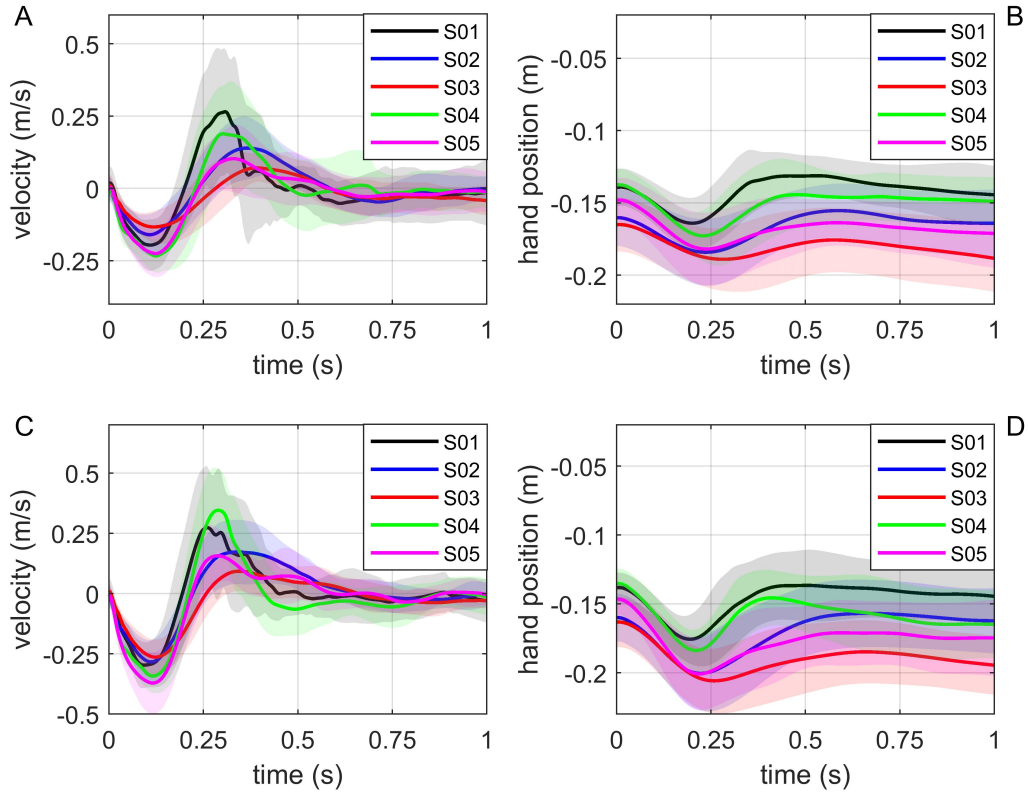

Figure 5. Mean and standard deviation of hand velocity, and hand position with respect to workspace center for all five subjects during the perturbation period (1 sec). (A) and (B) represent trials with 3N perturbation, and (C) and (D) represent trials with 5N perturbation.

(subject 1), 0.489±0.072 (subject 2), 0.559±0.124 (subject 3), 0.549±0.050 (subject 4), and 0.567±0.092 (subject 5). These values are higher than the R^2 values typically reported in biomechanics literature, such as [38].

A two-way ANOVA between subjects and trial groups (earlier – first 24 trials, and later – last 24 trials) was performed to check for a possible learning effect between earlier trials and later ones. After observing no significant interaction effect between subjects and trial groups ($p>0.219$), we found no significant difference between the trial groups ($p>0.869$), indicating no apparent evidence of learning or adaptation as the trial number

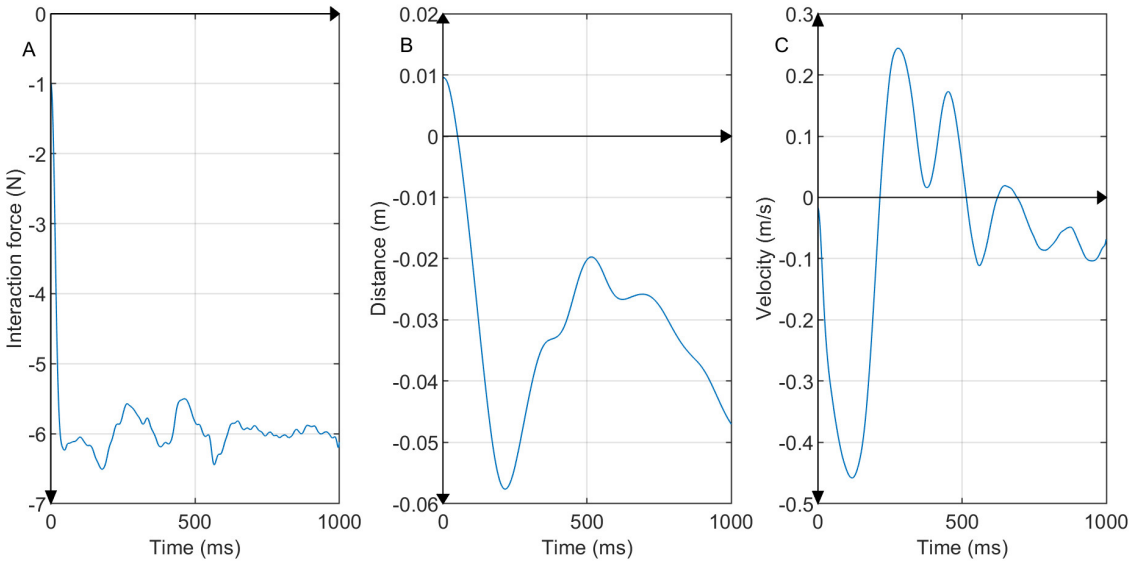

Figure 6. Measurements during force perturbation of a representative trial of subject 5. (A) The interaction force between the robot arm and the human subject, (B) the position of the hand/handle with respect to the origin of the workspace in y-direction, (C) the velocity of the handle in y-direction.

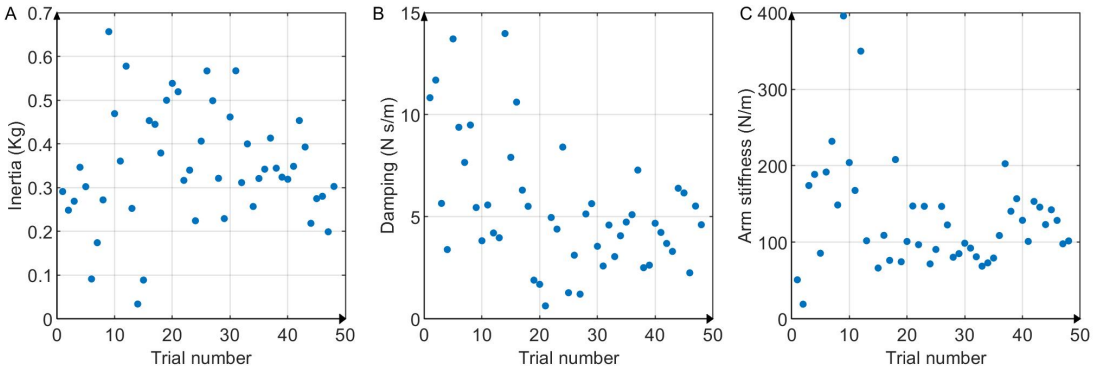

Figure 7. The interaction dynamics of the subject 5 in y-direction in all trials. (A) inertia, (B) damping, and (C) stiffness components identified through Equation 1.

increased. The stiffness parameter for trials belonging to the earlier and latter groups was 176.924.591 N/m and 174.360 N/m, with a standard deviation of 103.407 N/m and 88.430 N/m, respectively.

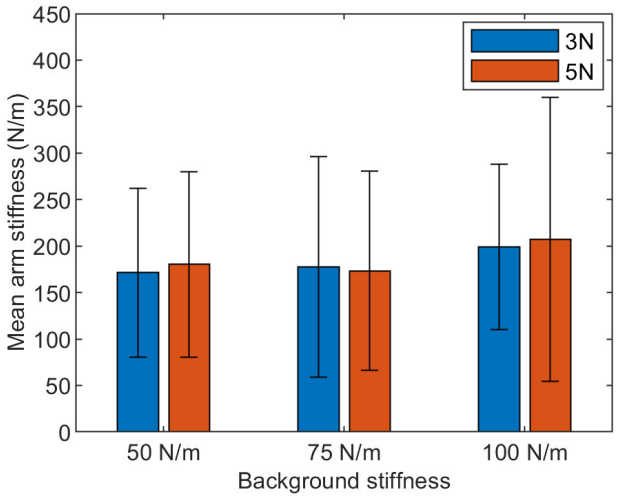

Figure 8. Average stiffness and standard deviation among all subjects for different robot settings.

The overground pHRI experiment presented in this work was designed as a three factorial experiment (visual condition – 2 levels, level of force perturbation – 2 levels, and level of stiffness in the robot arm – 3 levels). Including subject as a factor, the resultant experiment design can be represented as a four factorial experiment (subject – 5 levels). A four-way ANOVA was performed with all four factors to analyze whether the robot settings and/or the experiment conditions affected the estimation of the interaction dynamics. The omnibus test showed that at least one combination of those four factors (out of 60) resulted in a significantly different stiffness value than with other combinations (p=0.034, Table 1a). The effect of the robot settings on arm stiffness of different subjects can be seen in Figure 8. Further analysis showed that there is no interaction between the factors (Table 1b). The main effects of the visual condition (p>0.155), the level of perturbation (p>0.955), and the level of background stiffness (p>0.295) were all not significant, implying that neither the robot setting nor the experimental condition (eyes open/closed) affected the human arm stiffness measurement. In contrast, the main effect of the subject was significant (p<0.001), implying that, like most biomechanics experiments, large inter-subject variability exists.

Table 1. The results from the four-way ANOVA. It analyzed the effect of the subject, the level of perturbation, the level of background stiffness, and the vision (as the factors) to human arm impedance measurement.

(a) Analysis of Variance

Source	DF	Sum of Squares	Mean Square	F Ratio
Model	59	705584.6	11959.1	1.4525
Error	170	1399651.9	8233.2	**Prob>F**
C. Total	229	2105236.5		**0.0338***

(b) The main and the interaction effects

Source	Nparm	DF	Sum of Squares	F Ratio	Prob>F
Subject	4	4	350824.94	10.6527	**<.0001***
Visual Condition (VC)	1	1	16788.14	2.0391	0.1551
Level of Perturbation (LP)	1	1	26.25	0.0032	0.9550
Background Stiffness (BS)	2	2	20257.85	1.2302	0.2948
Subject∗VC	4	4	64032.19	1.9443	0.1053
Subject∗LP	4	4	16899.21	0.5131	0.7262
Subject∗BS	8	8	62781.47	0.9532	0.4745
VC∗LP	1	1	188.80	0.0229	0.8798
VC∗BS	2	2	38342.52	2.3285	0.1005
LP∗BS	2	2	4110.66	0.2496	0.7794
Subject∗VC∗LP	4	4	11684.79	0.3548	0.8404
Subject∗VC∗BS	8	8	55189.09	0.8379	0.5705
Subject∗LP∗BS	8	8	43300.14	0.6574	0.7283
VC∗LP∗BS	2	2	15288.33	0.9285	0.3972
Subject∗VC∗LP∗BS	8	8	9637.51	0.1463	0.9968

4. DISCUSSION

4.1. OBSERVATIONS FROM OPHRIE-HUMAN INTERACTION

Overall, the robot base's movement and the robot arm's dynamics were accepted well by the subjects. The forward velocity of the robot (0.5 m/s) appeared adequate while the subjects comfortably followed Ophrie. The background stiffness of the robot arm (50

to 100 N/m) was able to keep the human hand position near the origin of the robot arm's workspace most of the time. However, in some trials, the perturbation force pushed the hand to the outside of the workspace, in which case the trials were discarded and repeated. Although it rarely occurred, this happened more with low background stiffness (50 N/m) and high perturbation force (5 N) when the human hand position at the onset of the perturbation was in the $-y$ direction. Since the robot settings did not significantly affect the interaction dynamics (Table 1b), it is recommended to avoid the lowest background stiffness (50 N/m) and use the lower perturbation force (3 N) settings for future experiments with Ophrie.

The equilibrium point of the human arm was estimated to be 0.031 ± 0.031 m from the workspace center towards the robot. Figure 5B and D show that the average hand position right before the perturbation for all the subjects was towards the estimated equilibrium point. That is, the preferred equilibrium position of the hand was not at the center of the workspace where the interaction force would have been zero. This would not be a result of the human standing too close to the robot, because they were free to choose however close or far they could be with the robot. Instead, they all preferred to maintain a small pushing force between them and the robot. Since the equilibrium point location is decided by the central nervous system [39], it could be argued that it is the natural preference of humans to maintain a gentle push with Ophrie.

The unique challenge in arm stiffness measurement during overground interaction tasks (compared to the traditional seated interaction tasks) comes from the lack of stationary 'ground'. During seated pHRI experiments, the upper body of the subjects is stationary and assumed to be the reference from which the hand position can be obtained. The change in arm length due to perturbation is thus equal to the difference in the hand position at before and after the perturbation. On the other hand, during overground pHRI tasks, it is possible for the shoulder to also move during the force perturbation at hand. However, while following Ophrie by holding its handle as it moves forward with no turning, with the help of the arm movement recording from Vicon camera system, we observed that the interacting

human partner's shoulder move in a sinusoidal pattern in the mediolateral direction (due to the mediolateral sway during walking). As a result, the unperturbed arm length also followed the sinusoidal pattern since the shoulder position predominantly determined the arm length. When a force perturbation is applied at hand, this sinusoidal pattern may shift in response to the force. However, it was found that the shoulder did not deviate from its original sinusoidal pattern in the presence of the force perturbation. That is, the shoulder position seemed unaffected by the perturbation at hand. Hence, in our experiment, the change in arm length is equal to the change in hand position, which can be obtained from the encoders on the motors even when the shoulder position is not fixed with respect to the robot. In such a case, the shoulder and hand position recording (such as from Vicon camera system) is not required.

Since the availability of visual feedback during the experiment did not significantly affect the arm stiffness measurement as explained in the section 'Results', there is not a preference in eyes-open or closed conditions while designing an overground pHRI experiment in the future similar to this work. The same is true for different robot setting. Hence, any combinations of background stiffness (50, 75, or 100 N/m), perturbation level (3 or 5 N), or vision condition (eyes open or closed) could be used to measure the arm stiffness while designing an experimental protocol for the overground pHRI experiments in future. Nonetheless, as mentioned earlier, it was preferred by the study team to avoid the lowest background stiffness (50 N/m) as well as the higher level of perturbation (5 N) to minimize the possible occurrence of the hand being pushed out of the workspace of the robot arm.

Many pHHI and pHRI work discuss the effect of roles (leader or follower) in dyadic tasks [40]. In this work, Ophrie may not be a suitable follower since the wheeled base of Ophrie is not ideal for feedback control for adapting to quick changes in the commands (e.g. slow control loop). In addition, the wheel controllers have a predefined velocity profile along which the velocity increases or decreases. Nonetheless, this is acceptable for when the robot is leading and the human partner is following. While a hierarchical controller

that takes advantage of the fast and accurate robot arm control may allow Ophrie to take a follower role in the future, the current work focused on assigning the leader role to the robot. This also helped reduce variability in the experimental trials that may arise from variable robot trajectories. Having Ophrie as the leader also simulates a potential pHRI task of assisting people to walk.

4.2. ESTIMATING THE DYNAMICS DURING OVERGROUND PHRI EXPERIMENTS

4.2.1. Perturbation Method. A perturbation is provided for estimating the dynamics of physical interactions while the response is collected and interpreted. Two types of perturbations exist – force or position perturbations. Position perturbation has widely been used for human arm stiffness estimation since it was first introduced in mid 80's [16, 17, 20–27, 29, 34]. Position perturbation is useful when the expected movement trajectory of the hand is known, such as when the arm is at rest or when the unperturbed trajectory is provided [21]. However, in overground experiments similar to one presented in this work, predicting the unperturbed trajectory of the human arm/hand is nearly impossible due to the variability of the human movement while walking alongside the robot (as seen in Figure 4). Hence position perturbation may not be applicable.

Given this unique situation in overground pHRI, force perturbation is the only alternative for estimating the interaction dynamics; the recorded resultant displacement and the known applied force can be used for system identification assuming the arm dynamics to be linear second-order model. Force perturbation may be applied in the form of continuous perturbations with rich frequency components. [41] and [18] used pseudo-random binary sequence (PRBS) force inputs continuously for the entire period of the trial to estimate the joint mechanical properties in limb motion tasks. These studies used multiple repeated trials to obtain the ensemble mean trajectory from which deviations are calculated for estimating the impedance parameters. Alternatively, time-frequency analysis was performed

using force pulse to measure arm stiffness – which eliminated the requirement of multiple trials. For example, [42] used the estimates of body segment parameters that require a rich understanding of the inertial characteristics of the arm. In contrast, another [43] did not require such parameters. It used a parametric and a non-parametric estimator to estimate the continuous-time linear time-varying system of the arm dynamics. These methods require continuous mechanical perturbations in mostly stationary body segments. However, for the proposed pHRI experiment in this work, the arm configuration can neither be consistent within a trial nor between the trials. Hence the continuous force perturbation may not be applicable.

Because of these constraints, this work tested the feasibility of applying a single force perturbation instead of continuous force pulses and then using system identification similar to the methods used in previous studies by [19] and [32]. This would not intervene with the continuous overground physical interaction process throughout the entire trial as well as eliminate the need for baseline unperturbed trajectory. To this end, in this work, we propose a method to estimate the stiffness within one trial, as presented in the section 'Estimation of the Arm Stiffness'.

4.2.2. Assumptions and Challenges. The biggest challenge of the above method is to ensure that, at the time of the perturbation, the state of the system is similar across trials. For example, if the perturbation was applied at the middle of the trial, the arm configuration better be identical at that instant across all trials. However, it is nearly impossible to achieve this during overground pHRI tasks because the arm cannot be constrained due to the nature of the task. As a result, in this experiment, the perturbation may have been applied to the hand at varying arm configurations. This may have resulted in the stiffness parameter's relatively large variance along with inter-subject variabilities such as the muscle cross-sectional area and co-contraction. Nonetheless, acknowledging the possible sources

of deviations, larger sample sizes (or the number of trials) may help discern subtle changes in the parameters between experimental conditions. Indeed, as shown in Table 1b, statistical significance can be tested and discerned despite the potential variability.

A substantial assumption of the proposed method of estimating the dynamics of overground pHRI is that the dynamics is passive second-order as represented in Equation 1. While simple, this model, which was previously used in [41], served as a starting point in estimating the pHRI dynamics during overground tasks for the first time. Other studies, such as [33–35], have also used a similar mathematical model to represent the human arm dynamics. Consistent with the assumed model, the velocity response showed the characteristics of passive second-order dynamics between 0 ms and 250-400 ms. This allowed the estimation of the inertia, damping, and stiffness parameters of Equation 1. The estimated stiffness values were reasonable, with only five occurrences of below-zero stiffness out of 239 trials. These few aberrant values may have occurred due to the inherent variability of the overground pHRI experiment. The estimated damping and inertia values were also reasonable, although the variability seemed higher than for stiffness (Figure 7). This was somewhat expected since the first- and second-derivatives of the hand position are inevitably noisier than the position data. Hence, in this work, we used these parameters as indicators of the performance of the linear regression and the resulting stiffness estimate. The estimated inertia values were mostly positive and similar to the expected inertia of the lower arm (0.3~0.5 Kg). Also, the average damping was low and mostly positive, as expected. It was also comparable to the damping reported in [35]. Thus we concluded that the proposed method for estimating the dynamics is informative despite the simplicity.

4.3. ESTIMATED STIFFNESS

As mentioned earlier, the estimated stiffness from Equation 1 may be interpreted as the stiffness of the human arm due to the inherently low mechanical impedance of the robot arm and the absence of a passive elastic element in the robot. When the force perturbation

is applied in order to measure the arm stiffness, the CNS may modulate the arm stiffness in response to it. Hence the arm stiffness before and after CNS intervention may differ. In this view, our stiffness estimation method in the section 'Estimation of the Arm Stiffness' helps capture the pre-CNS intervention stiffness of the arm since the method uses the arm displacement data before typical neural delay (approx. 50~200 ms) even though the dynamics hasn't settled down to a steady-state.

In the seated pHRI experiments, it was reported that the human CNS tends to increase the arm stiffness in the direction of unstable dynamics or disturbance [22, 24, 25]. For example, in [22], the arm stiffness was higher in the direction of instability (up to 750 N/m) compared to when there was no disturbance (as low as 160 N/m). In this view, if the additional degree of freedom of the arm in overground pHRI (allowed by the unconstrained upper body of the human subject) was interpreted as an additional factor aiding instability, it may show up as increased stiffness. However, the measured arm stiffness in y-direction was similar to the lower values in [22]. This implies that the CNS may not view the increased freedom of arm movement in overground pHRI as a drawback. Instead, it may maintain the low arm stiffness for the arm to be more sensitive to the small changes in the interaction forces [38]. However, because the stiffness estimation in this work warrants further development, the implications of such low arm stiffness values during overground pHRI remain a topic for future research.

4.4. PROSPECTIVE BENEFITS

When physically interacting robots were first introduced for seated pHRI experiments, they quickly became invaluable tools not only for research but also for rehabilitation and physical therapies [5, 44]. We expect Ophrie to provide a similar impact and benefit to overground pHRI research. Key research questions may be addressed such as motor communication during overground physical interaction or to develop intuitive and effec-

tive walking assistance in the future. The demonstration of Ophrie's ability to perform an overground pHRI experiment and to estimate the interaction dynamics in this work is an important first step.

REFERENCES

[1] Robins, B., Amirabdollahian, F., Ji, Z., and Dautenhahn, K., 'Tactile interaction with a humanoid robot for children with autism: A case study analysis involving user requirements and results of an initial implementation,' in '19th International Symposium in Robot and Human Interactive Communication,' IEEE, 2010 pp. 704–711.

[2] Chang, W. H. and Kim, Y.-H., 'Robot-assisted therapy in stroke rehabilitation,' Journal of stroke, September 2013, **15**(3), pp. 174–181.

[3] Hieida, C., Abe, K., Attamimi, M., Shimotomai, T., Nagai, T., and Omori, T., 'Physical embodied communication between robots and children: An approach for relationship building by holding hands,' in '2014 IEEE/RSJ International Conference on Intelligent Robots and Systems,' IEEE, 2014 pp. 3291–3298.

[4] Saunderson, S. and Nejat, G., 'How robots influence humans: A survey of nonverbal communication in social human–robot interaction,' International Journal of Social Robotics, 2019, **11**(4), pp. 575–608.

[5] Hogan, N., Krebs, H. I., Charnnarong, J., Srikrishna, P., and Sharon, A., 'Mitmanus: a workstation for manual therapy and training ii,' in 'SPIE Applications in Optical Science and Engineering, Boston, MA, USA, March 26,' volume 1833, Telemanipulator Technology, 1993 pp. 28–34.

[6] Massie, T. H., Salisbury, J. K., *et al.*, 'The phantom haptic interface: A device for probing virtual objects,' in 'Proceedings of the ASME winter annual meeting, symposium on haptic interfaces for virtual environment and teleoperator systems, Chicago, IL, USA, November,' volume 55, Citeseer, 1994 pp. 295–300.

[7] Reed, K. B. and Peshkin, M. A., 'Physical collaboration of human-human and human-robot teams,' IEEE Transactions on Haptics, July 2008, **1**(2), pp. 108–120.

[8] Feth, D., Groten, R., Peer, A., Hirche, S., and Buss, M., 'Performance related energy exchange in haptic human-human interaction in a shared virtual object manipulation task,' in 'World Haptics 2009-Third Joint EuroHaptics conference and Symposium on Haptic Interfaces for Virtual Environment and Teleoperator Systems, Slat Lake City, UT, USA , March 18-20,' IEEE, March 2009 pp. 338–343.

[9] Mojtahedi, K., Whitsell, B., Artemiadis, P., and Santello, M., 'Communication and inference of intended movement direction during human–human physical interaction,' Frontiers in neurorobotics, 2017, **11**, p. 21.

[10] Zwijgers, E., *The effect of partner performance on arm impedance modulation during haptic human-human interaction*, Master's thesis, University of Twente, 2019.

[11] Stefanov, N., Peer, A., and Buss, M., 'Role determination in human-human interaction,' in 'World Haptics 2009-Third Joint EuroHaptics conference and Symposium on Haptic Interfaces for Virtual Environment and Teleoperator Systems, Slat Lake City, UT, USA , March 18-20,' IEEE, March 2009 pp. 51–56.

[12] Chen, T. L., Bhattacharjee, T., McKay, J. L., Borinski, J. E., Hackney, M. E., Ting, L. H., and Kemp, C. C., 'Evaluation by expert dancers of a robot that performs partnered stepping via haptic interaction,' PloS one, May 2015, **10**(5), p. e0125179.

[13] Takagi, A., Ganesh, G., Yoshioka, T., Kawato, M., and Burdet, E., 'Physically interacting individuals estimate the partner's goal to enhance their movements,' Nature Human Behaviour, 2017, **1**(3), pp. 1–6.

[14] Nichols, T. and Houk, J., 'Improvement in linearity and regulation of stiffness that results from actions of stretch reflex,' journal of Neurophysiology, 1976, **39**(1), pp. 119–142.

[15] Vincken, M., Gielen, C., and van der Gon, J. D., 'Stiffness control after fast goal-directed arm movements,' Human Movement Science, 1984, **3**(3), pp. 269–280.

[16] Mussa-Ivaldi, F. A., Hogan, N., and Bizzi, E., 'Neural, mechanical, and geometric factors subserving arm posture in humans,' Journal of Neuroscience, 1985, **5**(10), pp. 2732–2743.

[17] Bizzi, E., Mussa-Ivaldi, F., and Hogan, N., 'Regulation of multi-joint arm posture and movement,' in 'Progress in brain research,' volume 64, pp. 345–351, Elsevier, 1986.

[18] Lacquaniti, F., Carrozzo, M., and Borghese, N., 'Time-varying mechanical behavior of multijointed arm in man,' Journal of neurophysiology, 1993, **69**(5), pp. 1443–1464.

[19] Gomi, H. and Kawato, M., 'Human arm stiffness and equilibrium-point trajectory during multi-joint movement,' Biological cybernetics, 1997, **76**(3), pp. 163–171.

[20] Conditt, M. A., Gandolfo, F., and Mussa-Ivaldi, F. A., 'The motor system does not learn the dynamics of the arm by rote memorization of past experience,' Journal of Neurophysiology, 1997, **78**(1), pp. 554–560.

[21] Burdet, E., Osu, R., Franklin, D., Yoshioka, T., Milner, T., and Kawato, M., 'A method for measuring endpoint stiffness during multi-joint arm movements,' Journal of biomechanics, 2000, **33**(12), pp. 1705–1709.

[22] Burdet, E., Osu, R., Franklin, D. W., Milner, T. E., and Kawato, M., 'The central nervous system stabilizes unstable dynamics by learning optimal impedance,' Nature, 2001, **414**(6862), pp. 446–449.

[23] Burdet, E., Tee, K. P., Mareels, I., Milner, T. E., Chew, C.-M., Franklin, D. W., Osu, R., and Kawato, M., 'Stability and motor adaptation in human arm movements,' Biological cybernetics, 2006, **94**(1), pp. 20–32.

[24] Franklin, D. W., Liaw, G., Milner, T. E., Osu, R., Burdet, E., and Kawato, M., 'Endpoint stiffness of the arm is directionally tuned to instability in the environment,' Journal of Neuroscience, 2007, **27**(29), pp. 7705–7716.

[25] Krutky, M. A., Trumbower, R. D., and Perreault, E. J., 'Effects of environmental instabilities on endpoint stiffness during the maintenance of human arm posture,' in '2009 Annual International Conference of the IEEE Engineering in Medicine and Biology Society,' IEEE, 2009 pp. 5938–5941.

[26] Kadiallah, A., Franklin, D. W., and Burdet, E., 'Generalization in adaptation to stable and unstable dynamics,' PLoS one, 2012, **7**(10), p. e45075.

[27] Takagi, A., Xiong, G., Kambara, H., and Koike, Y., 'Endpoint stiffness magnitude increases linearly with a stronger power grasp,' Scientific Reports, 2020, **10**(1), pp. 1–9.

[28] Scott, S. H., 'Apparatus for measuring and perturbing shoulder and elbow joint positions and torques during reaching,' Journal of neuroscience methods, July 1999, **89**(2), pp. 119–127.

[29] Bennett, D. J., 'Torques generated at the human elbow joint in response to constant position errors imposed during voluntary movements,' Experimental Brain Research, 1993, **95**(3), pp. 488–498.

[30] Regmi, S. and Song, Y. S., 'Design Methodology for Robotic Manipulator for Overground Physical Interaction Tasks,' Journal of Mechanism and Robotics, August 2020, **12**(4), p. 041002.

[31] Regmi, S. and Song, Y. S., 'Estimation of endpoint impedance of a 2d parallel manipulator using numerical simulation experiments,' in 'ASME International Mechanical Engineering Congress and Exposition,' volume 84522, ASME, 2020 p. V005T05A066.

[32] Milner, T. E., 'Dependence of elbow viscoelastic behavior on speed and loading in voluntary movements,' Experimental Brain Research, 1993, **93**(1), pp. 177–180.

[33] Dolan, J. M., Friedman, M. B., and Nagurka, M. L., 'Dynamic and loaded impedance components in the maintenance of human arm posture,' IEEE transactions on systems, man, and cybernetics, 1993, **23**(3), pp. 698–709.

[34] Tsuji, T., Morasso, P. G., Goto, K., and Ito, K., 'Human hand impedance characteristics during maintained posture,' Biological cybernetics, 1995, **72**(6), pp. 475–485.

[35] Rahman, M., Ikeura, R., and Mizutani, K., 'Control characteristics of two humans in cooperative task and its application to robot control,' in '2000 26th Annual Conference of the IEEE Industrial Electronics Society. IECON 2000. 2000 IEEE International Conference on Industrial Electronics, Control and Instrumentation. 21st Century Technologies,' volume 3, IEEE, 2000 pp. 1773–1778.

[36] Holmes Jr, G. L., *Trajectory control of a wheeled robot using interaction forces for intuitive overground human-robot interaction*, Missouri University of Science and Technology, 2020.

[37] Sylos-Labini, F., d'Avella, A., Lacquaniti, F., and Ivanenko, Y., 'Human-human interaction forces and interlimb coordination during side-by-side walking with hand contact,' Frontiers in physiology, March 2018, **9**, p. 179.

[38] Rashid, F., Burns, D., and Song, Y. S., 'Sensing small interaction forces through proprioception,' Scientific Reports, 2021, **11**(1), pp. 1–10.

[39] Bizzi, E., Hogan, N., Mussa-Ivaldi, F. A., and Giszter, S., 'Does the nervous system use equilibrium-point control to guide single and multiple joint movements?' Behavioral and brain sciences, 1992, **15**(4), pp. 603–613.

[40] Mörtl, A., Lawitzky, M., Kucukyilmaz, A., Sezgin, M., Basdogan, C., and Hirche, S., 'The role of roles: Physical cooperation between humans and robots,' The International Journal of Robotics Research, 2012, **31**(13), pp. 1656–1674.

[41] Bennett, D., Hollerbach, J., Xu, Y., and Hunter, I., 'Time-varying stiffness of human elbow joint during cyclic voluntary movement,' Experimental brain research, 1992, **88**(2), pp. 433–442.

[42] Piovesan, D., Pierobon, A., DiZio, P., and Lackner, J. R., 'Experimental measure of arm stiffness during single reaching movements with a time-frequency analysis,' Journal of neurophysiology, 2013, **110**(10), pp. 2484–2496.

[43] van de Ruit, M., Cavallo, G., Lataire, J., Van Der Helm, F. C., Mugge, W., van Wingerden, J.-W., and Schouten, A. C., 'Revealing time-varying joint impedance with kernel-based regression and nonparametric decomposition,' IEEE Transactions on Control Systems Technology, 2018, **28**(1), pp. 224–237.

[44] Salisbury, J. K. and Srinivasan, M. A., 'Phantom-based haptic interaction with virtual objects,' IEEE Computer Graphics and Applications, September 1997, **17**(5), pp. 6–10.

IV. HUMANS MODULATE ARM STIFFNESS TO FACILITATE MOTOR COMMUNICATION DURING OVERGROUND PHYSICAL HUMAN-ROBOT INTERACTION

Sambad Regmi[1], Devin Burns[2], Yun Seong Song[1]

[1]Department of Mechanical and Aerospace Engineering, Missouri University of Science and Technology, Rolla, MO 65409

[2]Department of Psychological Science, Missouri University of Science and Technology, Rolla, MO 65409

ABSTRACT

We, humans, are able to accomplish overground physical interaction tasks adeptly. These interaction tasks do not necessarily require visual and verbal communication, which suggests that the interacting partners might exchange the kinematic information to communicate. To understand the process of motor intent exchange, we present an overground robot-guided walking experiment designed and conducted to capture human biomechanic response during the interaction. We tested the hypothesis that the nervous system lowers the arm stiffness to sensitively exchange forces and motions. The outcome of the experiment agrees with our hypotheses.

Keywords: arm stiffness, physical human-robot interaction (pHRI), overground, force perturbation, motor communication, interaction force

1. INTRODUCTION

We can do physical interactions such as assisting an elderly walk or partnered dancing without verbal communication. How are we able to accomplish such physical interactions so adeptly? The nervous system executes a freestanding control strategy while interacting with an external environment – not a human. It first adapts to and learns from instabilities,

then develops a strategy and executes it in similar future instances [1–3]. Holding a coffee mug without spilling the coffee, even when the posture gets unstable for a moment, is a perfect example of the freestanding control strategy. The central nervous system (CNS) optimizes impedance – resistance to imposed motion and force – to stabilize such unstable dynamics [1]. Particularly, the increase in arm stiffness – a component of impedance – has been observed in the direction of the instability [3].

The arm stiffness has largely been studied in relation to motor control for stability and reaching tasks [1–8]. Such studies investigated interaction tasks where subjects were mostly seated – the subject's degree of freedom was constrained, and the interacting environment did not play an active role in the control process. However, the physical human-human interaction (pHHI) tasks are usually overground, and the coupled system cooperates to accomplish a common goal. Such stable interaction would not be possible without an efficient exchange of sophisticated information between the interacting individuals.

It has been observed that we use arms during physical interaction as a medium for two-way motor communication [9–11]. Even though visual or verbal feedback may aid the physical interaction process, they are not an absolute necessity [12, 13]. Moreover, we exchange small forces via hand, which is also the point of interaction, and our nervous system analyzes these movements – resulting due to the small interaction forces – to decode the exchanged information [14]. Intuitively, the decoding process could have been aided by the increased sensitivity of the arms to interaction force (i.e., resulted movement). Hence, people may lower the mechanical impedance of their arms for increased sensitivity to interaction force for communicating motor intent as pointed by [15]. In this view, understanding the process of arm impedance modulation may be the crucial first step to understanding overground physical interaction characteristics in humans.

Since the existing tools and the experimental protocols to measure arm impedance were limited to the seated physical human-robot interaction (pHRI) experiments [1–3, 12, 16], a robot dedicated to the overground pHRI experiments was developed, and an

experimental protocol that can record the human arm movement data and estimate the arm impedance using those was previously proposed by our group [17]. The experimental protocol and the ability of the robot to estimate the arm impedance from the force-motion data recorded were validated through an overground pHRI experiment.

Using the experimental protocol suggested in [17], we investigated the hypotheses "human arm stiffness is modulated to promote motor communication", and "low arm stiffness is a way to sense interaction force more accurately through the large changes in the kinematics". Clearly, it was crucial to design an experiment that includes tasks with a high chance of modulation for arm impedance. In the absence of verbal or visual information feedback, humans are compelled to listen (or sense) to the haptic information provided by the interacting partner during overground physical interaction tasks. In this view, the overground pHRI experiment presented in this paper examined two contrasting cases – (a) which compels the human subjects to listen to the haptic information and (b) where humans might not feel as compelled as before – was designed and conducted. The analysis of variance (ANOVA) was then performed to statistically analyze if there is any evidence of arm stiffness modulation when humans listen to haptic cues compared to when they do not.

2. METHODS

2.1. PARTICIPANTS

A total of 10 healthy young adults (1 female, 1 left-handed, 27.6±2.41 years) without any self-reported neurological disorder took part in the study. Subjects signed a written consent form before participating in the experiment. The research protocol was approved by the Institutional Review Board of the University of Missouri System.

2.2. EXPERIMENT PROTOCOL

A guided walking experiment was designed wherein the human participants were asked to walk alongside the robot Ophri – that acted as a leader – during the trials. Ophri was specially designed for the overground pHRI experiments. Its manipulator inherits some unique characteristics that are critical to the overground physical interaction experiments, such as low inherent endpoint impedance, ability to apply and measure small force perturbation (<10N), and capability of endpoint movement with a speed of 2Hz [17, 18].

At the beginning of the experiment, the subjects were detailed about what was expected from them. During each trial, the human participants were asked to stand upright next to Ophri by holding its interaction handle using their right hand as shown in Figure 1b. The robot's height was adjusted beforehand such that the interaction handle was aligned to the subject's elbow level. Also, the subjects were informed that the position based background stiffness controller would be activated after they are ready, and hence they should relax their arm to let the robotic arm position the handle to the center of its workspace – a 0.15x0.15 m^2 2-dimensional space parallel to the ground plane (see Figure 1a). The subjects were informed that after they hear the command START, the robot would start to move, and they had to follow the robot with their eyes closed throughout the entire trial. The robot was programmed to go on a straight trajectory for 1.5m. It would either continue in the straight trajectory or turn towards or away from the subject in the mediolateral direction after 1.5m. As shown in Figure 1a, if the robot did turn, it would turn back to a straight trajectory parallel to the starting trajectory after 3.8s and would maintain that for the rest of the trial. The path for the these three different trajectories were marked on the floor using colored tapes to ensure that the subjects clearly understood (a) where the robot might turn and (b) the experiment design that "if the robot turns once, there is no more turning". Given their eyes were closed, the subjects were expected to listen to haptic information through the interaction handle to sense the speed of the robot and the deviation in the trajectory when the robot turned. After the robot stopped, the subjects were asked to

tell in which direction the robot deviated based on their judgment before opening their eyes. Throughout the entire trial, the robot was programmed to maintain a constant linear velocity of 0.5m/s. It maintained the angular velocity of 0.45rad/s while turning. The robotic arm applied a force perturbation of 3N (0.8 seconds) when it reached B if it was not supposed to turn, or at E or H if it did turn (see Figure 1a). The direction of force perturbation was either towards the direction of movement or towards the subject's mediolateral direction. Subjects were aware that the robot might turn and will also apply a slight push at some point on the trajectory but were unaware of the direction of the turn or the direction of perturbation for that specific trial. Due to safety concerns, if at all the interaction handle is out of the workspace at any time during the trial, the robot was programmed to stop; in such a scenario, the trial was repeated. The presence of a background stiffness controller helped the subjects maintain their hand inside the workspace; the stiffness controller was, however, briefly turned off during the time of perturbation. Each trial took approximately 20 seconds. The top view sketch of the entire experimental setup and the ideal starting pose for each trial is shown in Figure 1.

The decision on the magnitude of background stiffness (75 N/m^2, the magnitude of force perturbation (3N), and the subject's visual feedback condition (eyes closed) were taken based on our previous investigation on the overground pHRI experiments [17].

Here onward, a trial can be referred with respect to the direction of perturbation – as 'lateral' for -y perturbation and 'forward' for -x perturbation, and with respect to the trajectory – as 'before' for straight trajectory (the perturbation happened before the midway) and 'after' for deviated trajectory (the perturbation happened after the midway) (see Figure 1a). 'after-T' and 'after-A' will be used for trials with trajectory deviation towards the subject or away from the subject, respectively, whenever needed. In this view, we have six different trial types depending on the direction of trajectory deviation (3 levels) and the direction of force perturbation (2 levels). The experiment was designed as a randomized complete block (RCB) design. Each block consisted of eight randomly distributed trials

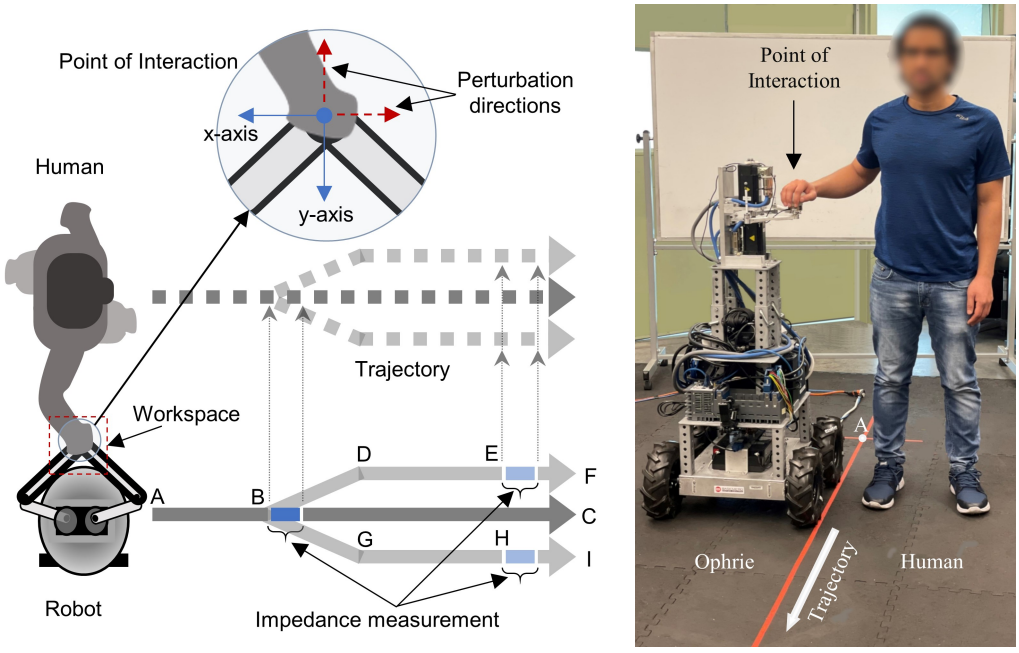

(a) (b)

Figure 1. (a) Schematics of the overground pHRI experiment setup (top view). The horizontal length of AB, BC, BD/BG, DE/GH, and EF/HI are 1.5m, 3.95m, 1.25m, 1.85m, and 0.85m, respectively. The DEF/GHI part of the trajectory ABDEF/ABGHI is separated by the perpendicular distance of 0.5m. (b) A human participant mimicking the experimental setup before the beginning of a trial.

(2 'after-T' trials, 2 'after-A' trials, and 4 'before' trials; each of these group had an equal number of forward and lateral trials). The 'before' trials were repeated within a block to balance the number with 'after' trials. There were 5 blocks totaling the number of trials per subject to 40.

2.3. DATA ACQUISITION AND ANALYSIS

The interaction dynamics is the function of arm movement and its derivative. A simplified model, as used previously in [17] will be used in this study where we assume the interaction dynamics in task space as passive, linear, and time-invariant second-order dynamics.

$$f - f_0 = m\,(\ddot{x} - \ddot{x}_0) + b\,(x - \dot{x}) + k\,(x - x_0) \tag{1}$$

where f is the interaction force measured after the onset of force perturbation, x, $\dot{x}$, and $\ddot{x}$ are the position, velocity and acceleration of the hand after the perturbation, respectively and m, b, and k are the characteristics of the interaction dynamics namely inertia, damping, and stiffness, respectively. x_0, $\dot{x}_0$, and $\ddot{x}_0$ are the mean hand position, velocity, and acceleration of the interaction point before the perturbation, respectively. Likewise, f_0 is the average interaction force before the perturbation. The data of 0.1-second window before the perturbation onset was used for averaging.

When the force perturbation is applied, we may respond to the push by either moving just the arm or the entire body during an overground pHRI task. In this view, the x in the above Equation 1 should represent the arm length – defined as the magnitude of a vector from the shoulder to the hand – rather than the hand position. However, we will use the coordinate of the hand position as x, as mentioned earlier, because our prior investigation revealed that the change in hand position was identical to the change in arm length [17].

The hand position in 2D (which is identical to the manipulator's endpoint displacement) can be calculated using the motors' encoder position with the help of forward kinematics. The motor shaft position was measured with the single-turn absolute Biss sine encoder (2048 LPR) embedded in the servo motors (AKM32E-ANCNAA00: Kollmorgen Corp, VA, USA). The kinematic details of the robot arm can be found in [18]. The interaction forces were measured using the mini45 force/torque sensor (ATI Industrial Automation, NC, USA), which is lodged between the endpoint of the robotic arm and the interaction handle. The data were recorded with a sampling rate of 1KHz. After recording, the hand position and force data were filtered using Butterworth low-pass zero-lag filter with 40Hz cutoff frequency in Matlab (MathWorks Inc., MA, USA).

The method of estimating arm stiffness in the direction of force perturbation during overground pHRI experiments was proposed in our previous work [17], and the same will be used in this article. To do so, the hand velocity versus time graph was plotted in Matlab and the time instant of the second peak on the velocity-vs-time plot was manually identified

and noted. The multi-variable linear regression was applied using Matlab fitlm function to estimate m, b, and k in Equation 1. The interaction force and the hand position data from the onset of the perturbation (t = 0ms) to the time at which the velocity-time graph showed the second peak was fitted on Equation 1. The stiffness (k) is the main outcome of interest, whereas the inertia (m) and the damping (b) will not be analyzed. Lastly, the equilibrium point for each trial was calculated by substituting m, b, and k values estimated from Equation 1 in Equation 2, which represents the interaction dynamics right before the perturbation.

$$f_0 = m\,\ddot{x}_0 + b\,\dot{x}_0 + k\,(x_0 - x_{eq}) \tag{2}$$

where x_{eq} is the position of the equilibrium point of the arm at that instant.

Each trial from the experiment fetched one scalar stiffness value. It can be considered as the arm's resistance to an external perturbation towards the axis of the perturbation. In our experiment, the perturbation was either towards the lateral direction or towards the forward direction. Out of 400 trials performed by 10 different subjects, 17 were discarded because the stiffness estimated was negative. From the remaining data, outliers – defined as the values 3 times the interquantile range past the 25^{th} and the 75^{th} quantiles – were screened out using JMP statistical software (SAS Institute Inc., NC, USA). 11 outliers were excluded from the data for further analysis. ANOVA was performed using JMP in the remaining 372 stiffness values to test whether humans modulate arm stiffness when listening to haptic cues compared to when they are not listening. A significance level of p = 0.05 was used.

3. RESULTS

The average interaction force among all the subjects and all the trials due to background stiffness right before the perturbation onset was observed to be 2.215±0.976N at 0.202±1.030rad counterclockwise from the interacting subject's mediolateral direction (i.e., -y in Figure 1a). That is, on average, the subjects were pushing the robot away from their

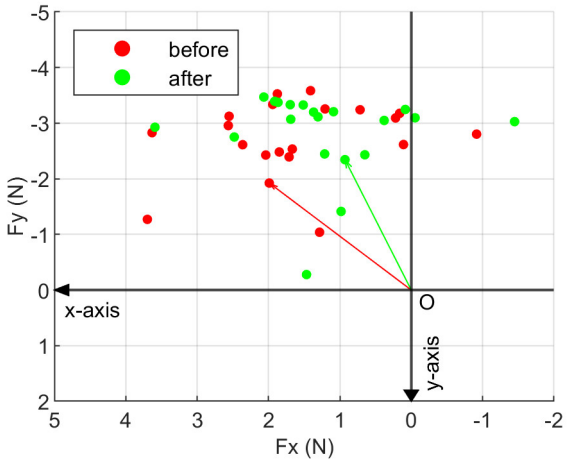

Figure 2. The interaction forces due to background stiffness for all trials performed by a representative subject. The red dots represent the trials having 'before' trajectory, and the green dots represent the trials having 'after' trajectory.

trunk at approximately 2N of force. This result aligns with the one observed in our prior investigation [17]. The interaction force right before the perturbation initiation for all the trials performed by subject 1 is shown in Figure 2. The interaction forces during the entire trial for the two representative 'after' trials (one 'lateral' trial and one 'forward' trial) performed by subject 1 are shown in Figure 3. The hand movement trajectory for 300ms after the perturbation initiation for the first block of the trials performed by subject 1 is shown in Figure 4.

The interaction dynamics were estimated using linear regression as discussed in the Section 2.3. The mean and standard deviation of the R^2 values of all 40 trials for each subject were 0.568±0.108 (subject 1), 0.567±0.087 (subject 2), 0.533±0.078 (subject 3), 0.578±0.084 (subject 4), 0.528±0.047 (subject 5), 0.559±0.062 (subject 6), 0.539±0.072 (subject 7), 0.516±0.040 (subject 8), 0.520±0.071 (subject 9), and 0.582±0.175 (subject 10). These values are in a similar range to the R^2 values reported in our earlier work on overground pHRI [17]. The mean arm stiffness and the standard deviation for the individual subjects based on the perturbation type is shown in Figure 5, and based on the trajectory type is shown in Figure 6. The linear regression also fetched inertia and damping for each

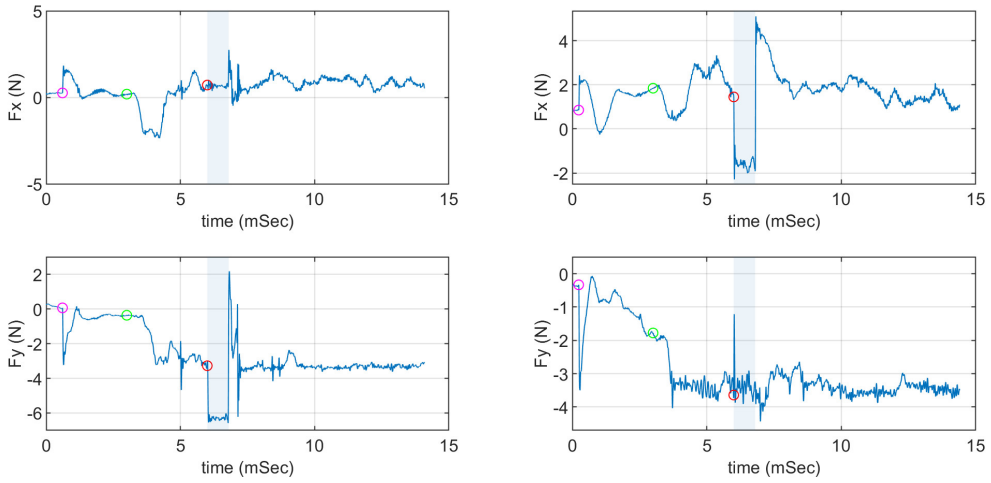

(a) (b)

Figure 3. The interaction forces during the entire trial of the two representative trials performed by the subject 1. The position-based background stiffness controller was activated at the pink circle marker. The instant when the robot started moving and the subject followed is represented by the green circle marker. The red circle marker represents the instant when the force perturbation was initiated; the blue shaded region shows the 800ms window of the force perturbation. (a) is the representative 'before'-'lateral' trial and (b) is the representative 'before'-'forward' trial

trial. The average of inertia estimated from all 40 trials of all the subjects was found to be 0.207±0.275 kg. The average damping was observed to be 9.114±8.321 Ns/m. The low positive values of inertia and damping are in alignment with our previous work [17]. The mean equilibrium point of the arm was estimated to be at 0.027±0.045 m (averaged over all trials and all subjects) away from the workspace center towards the robot. The statistics presented earlier in this section and afterward only include the trials excluding outliers and negative stiffness values (n = 372).

The skewness and the excess kurtosis were 1.275 and 1.472, respectively. [19] pointed out that either the skewness other than the one between -3 and +3 and the excess kurtosis larger than 4 can be used as reference values for determining substantial non-normality. In this view, the distribution of our data cannot be considered substantially non-normal. Hence, we can proceed to analyze the data with the help of parametric

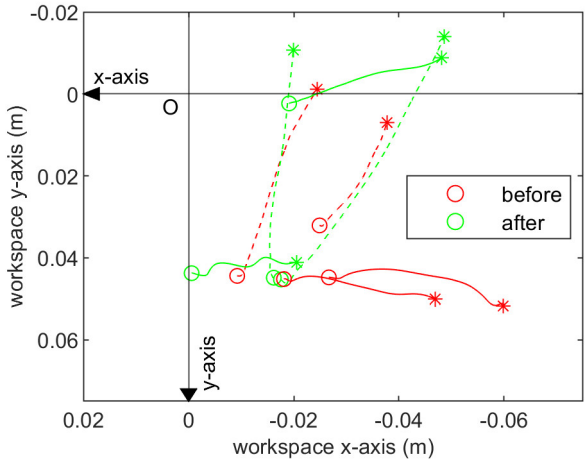

Figure 4. The figure shows the hand movement trajectory of all the trials in block 1 performed by subject 1. The red-colored lines represent the 'before' trials, whereas the green-colored lines represent the 'after' trials. The dashed lines represent the 'lateral' trials, whereas the continuous lines represent the 'forward' trials. 'o' represents the handle location when the perturbation was initiated, and '*' represents the handle location after 300ms of the perturbation initiation.

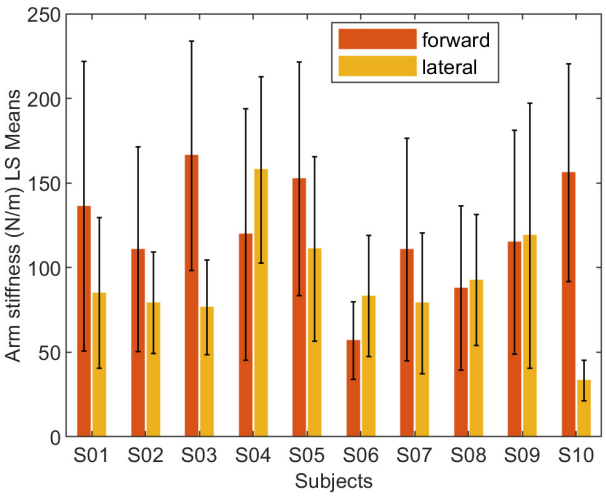

Figure 5. The mean and the standard deviation of individual subject's arm stiffness based on perturbation direction.

tests.When a paired t-test was performed between the members of the 'after' trials – 'after-T' trials vs 'after-A' trials, it was observed that the arm stiffness between those two trial

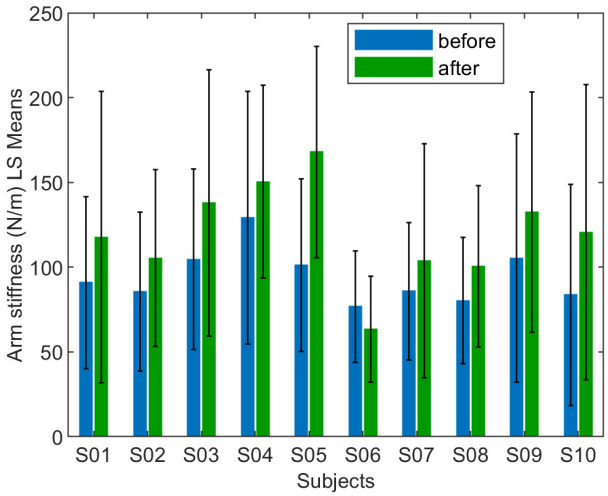

Figure 6. The mean and the standard deviation of individual subject's arm stiffness based on trajectory type.

types was not significantly different from each other (p>0.780; 'after-T' least square mean = 120.099N/m, 'after-A' least square mean = 127.174N/m). Hence, both the 'after-T' trials and the 'after-A' trials will be grouped and labeled as 'after' trials for further analysis.

We performed a three-way ANOVA with the following factors: subject – 10 levels, trajectory – 2 levels ('before,' and 'after'), and perturbation direction – 2 levels ('lateral' and 'forward'). The omnibus test (Table 1) showed that the mean of at least one combination in the ANOVA model is significantly different from others (p<0.0001). Next, the main and interaction effects were analyzed, which can be found in Table 2. The three-way interaction of the included factors is not significant (p>0.090). Likewise, there is no significant interaction between the subject and the trajectory (p>0.179, see Figure 6). In contrast, a strong interaction between the subjects and the perturbation direction was observed to affect the arm stiffness (p<0.0001), which implies that the trend in variation of the arm stiffness in lateral to forward direction is not consistent among subjects (see Figure 5). Likewise, a significant interaction between the experiment design parameters (perturbation direction and trajectory) is observed (p<0.0001). This suggests that the arm stiffness in different directions varies differently based on when it is measured – that is, before or after the

Table 1. Analysis of Variance of the model

Source	DF	Sum of Squares	Mean Square	F Ratio
Model	39	605320.2	15521.0	5.7126
Error	332	902033.6	2717.0	**Prob>F**
C. Total	371	1507353.8		<**0.0001***

deviation in Figure 7. However, the focus of the experiment design was to identify whether the arm stiffness is significantly different in the 'after' trials compared to the 'before' trials without worrying much about how the arm stiffness is influenced by the interaction between the experimental design parameters. Hence, the main effect of the factors was analyzed next. The main effect of the subject was significant ($p<0.0001$), implying that, like most biomechanics experiments, large inter-subject variability exists. Likewise, arm stiffness is significantly different based on the perturbation direction ($p<0.0001$). Arm stiffness is generally represented as an ellipse due to its direction dependency, and the outcome obtained in this study aligns with that. It is interesting that the arm stiffness is higher in the forward perturbation trials than in lateral perturbation trials and will be discussed in detail later in Section 4. More importantly, the human arm stiffness during the overground pHRI task is significantly different in the trials with the 'before' trajectory compared to those with the 'after' trajectory ($p<0.0001$). The arm stiffness means for the trials with 'before' trajectory was 95.530±54.661 N/m, and for those with 'after' trajectory was 118.604±70.247 N/m. Lastly, when the subjects were asked to tell the perceived trajectory type after each trial ended, they reported the trajectory deviation correctly in 386 out of 400 trials.

4. DISCUSSION

The trajectories were specially designed to capture the contrast in overground arm stiffness between (a) when the subjects would actively listen to the haptic cues from the robot and (b) when they would not. The former represented the 'before' trial where the

Table 2. The main and interaction effects of the factors

Source	Nparm	DF	Sum of Squares	F Ratio	Prob>F
Subject	9	9	165466.11	6.7668	**<.0001***
Trajectory	1	1	56182.72	20.6785	**<.0001***
Perturbation Direction	1	1	85846.42	31.5964	**<.0001***
Subject∗Trajectory	9	9	34697.11	1.4189	0.1785
Subject∗Perturbation Direction	9	9	174534.85	7.1376	**<.0001***
Trajectory∗Perturbation Direction	1	1	69678.12	25.6455	**<.0001***
Subject∗Trajectory∗ Perturbation Direction	9	9	41356.29	1.6913	0.0899

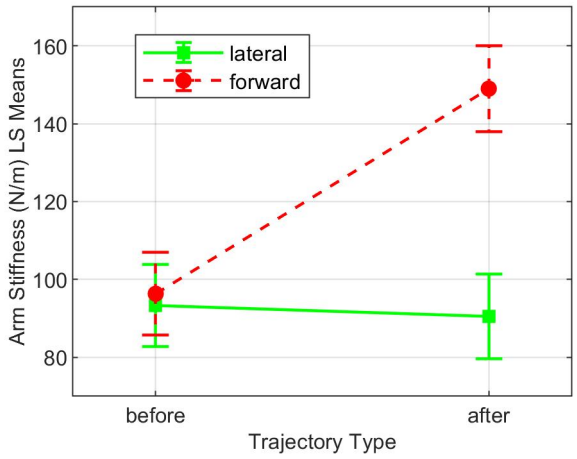

Figure 7. The effects of perturbation direction on the arm stiffness (N/m) (least square means, confidence interval of 95%) based on the trajectory type.

subjects were perturbed at the exact location where they would turn, had it been an 'after' trial. In this scenario, we expected the subjects to actively listen to the robot through hand because (a) they were not told whether the robot would turn or not for that specific trial, and hence had to entirely rely on the robot for turning if in case it turns, and (b) since their eyes were closed, the only way they could get the speed information to synchronize with the robot was from their interacting hand. Because the linear velocity of the robot was constant, the need to synchronize was only expected during the earlier phase of the

trial. Furthermore, every time the trial was completed, the participants were asked to tell the study team the type of trajectory they had just finished. This could have acted as an additional factor compelling the subjects to be more conscious until the robot turned. In the 'after' trials, though, the arm stiffness was measured long after the robot completed the turn, which means that the subjects did not have any compelling reason to listen to the haptic information from the robot.

In the Section 3, we observed that the arm stiffness was significantly different in 'before' trials compared to 'after' trials ($p<0.0001$). This indicates that humans can modulate arm stiffness during overground physical interaction tasks. The decision seems to be based on whether they have to listen to haptic information (i.e. 'before' trajectory) or not (i.e. 'after' trajectory). In addition, the subjects reported the trajectory deviation correctly in 386 trials out of 400, which further strengthens that subjects were actively listening to haptic information from the robot, at least before the trajectory deviation. The arm stiffness mean for the trials where they might have been listening was 95.530±54.661 N/m, and in those where they might not have been listening was 118.604±70.247 N/m. This indicates that the humans maintained comparatively lower arm stiffness while listening to motor commands than while not listening.

In this view, considering the overall arm stiffness during the overground interaction tasks, based on the ANOVA results, it is clear that, whatever the reasons are, the arm stiffness was lower for the 'before' trials compared to the 'after' trials. This suggests that humans can modulate arm stiffness and, more importantly, lower their arm stiffness to facilitate an efficient exchange of the haptic information during an overground physical interaction.

During overground interactions, like the one in this experiment, the participants had the complete freedom to move both the upper arm and the forearm. Forward movements cannot be completed without moving both the upper arm and the forearm. Hence, while listening to haptic information in the forward direction, it could be beneficial to lower the stiffness of both the upper arm and the forearm to capture the motion information sensitively.

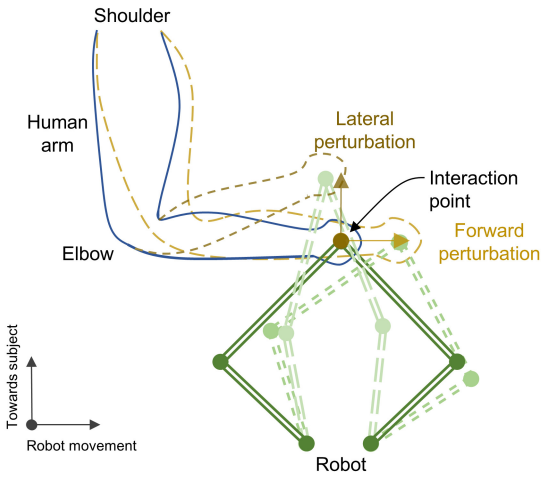

Figure 8. Sketch showing how the interaction proceeds after the perturbation in the 'forward' trial and the 'lateral' trials.

However, the movement in the lateral direction can be accomplished solely by moving the lower arm around the elbow, and the entire arm does not need to move. Furthermore, while listening to the haptic information, letting the forearm capture the motion information (by reducing its stiffness) could be more effective than lowering the arm stiffness of both. In such a case, the upper arm can act as a very high impedance link, and the stiffness of the lower arm could be decreased, resulting in the overall arm stiffness not changing a lot. This could be the reason why we observed significantly lower arm stiffness in 'forward' + 'before' trials compared to 'forward' + 'after' trials, but at the same time did not see any significant difference of the arm stiffness between 'lateral' + 'before' trials and 'lateral' + 'after' trials (see Figure 7). The sketch in Figure 8 depicts the discussed scenario of the arm movement.

The main effect of the subjects is significant, which was expected because every individual is different and might respond to similar perturbation differently. It is not uncommon to have higher inter-subject variability in the experiments involving humans. More uncertainty could have been added due to the nature of the experiment itself (i.e., overground scenario). A similar effect was observed in our previous study involving the

overground pHRI experiment [17]. Some of the other factors that could have introduced variation within subjects in this study are the difference in the participants' walking habits (posture), which could have resulted in different arm postures within individuals while walking, the difference in their arm build (muscle cross-sectional area), etc.

Further, the structure of the arm might affect the stiffness differently in different directions. For example, stronger triceps would lead to higher arm stiffness in the forward direction than less strong triceps. However, it might not matter to the arm stiffness in the lateral direction if, as explained earlier, the stiffness of the lower arm contributes significantly to the overall arm stiffness. Because of this reason, we might have seen a significant interaction between the subjects and the perturbation direction.

REFERENCES

[1] Burdet, E., Osu, R., Franklin, D. W., Milner, T. E., and Kawato, M., 'The central nervous system stabilizes unstable dynamics by learning optimal impedance,' Nature, 2001, **414**(6862), pp. 446–449.

[2] Burdet, E., Tee, K. P., Mareels, I., Milner, T. E., Chew, C.-M., Franklin, D. W., Osu, R., and Kawato, M., 'Stability and motor adaptation in human arm movements,' Biological cybernetics, 2006, **94**(1), pp. 20–32.

[3] Franklin, D. W., Liaw, G., Milner, T. E., Osu, R., Burdet, E., and Kawato, M., 'Endpoint stiffness of the arm is directionally tuned to instability in the environment,' Journal of Neuroscience, 2007, **27**(29), pp. 7705–7716.

[4] Lacquaniti, F., Carrozzo, M., and Borghese, N., 'Time-varying mechanical behavior of multijointed arm in man,' Journal of neurophysiology, 1993, **69**(5), pp. 1443–1464.

[5] Gomi, H. and Kawato, M., 'Human arm stiffness and equilibrium-point trajectory during multi-joint movement,' Biological cybernetics, 1997, **76**(3), pp. 163–171.

[6] Scott, S. H., 'Apparatus for measuring and perturbing shoulder and elbow joint positions and torques during reaching,' Journal of neuroscience methods, July 1999, **89**(2), pp. 119–127.

[7] Selen, L. P., Beek, P. J., and Van Dieën, J. H., 'Impedance is modulated to meet accuracy demands during goal-directed arm movements,' Experimental Brain Research, 2006, **172**(1), pp. 129–138.

[8] Piovesan, D., Pierobon, A., DiZio, P., and Lackner, J. R., 'Experimental measure of arm stiffness during single reaching movements with a time-frequency analysis,' Journal of neurophysiology, 2013, **110**(10), pp. 2484–2496.

[9] Reed, K. B. and Peshkin, M. A., 'Physical collaboration of human-human and human-robot teams,' IEEE Transactions on Haptics, July 2008, **1**(2), pp. 108–120.

[10] Stefanov, N., Peer, A., and Buss, M., 'Role determination in human-human interaction,' in 'World Haptics 2009-Third Joint EuroHaptics conference and Symposium on Haptic Interfaces for Virtual Environment and Teleoperator Systems, Slat Lake City, UT, USA , March 18-20,' IEEE, March 2009 pp. 51–56.

[11] Sylos-Labini, F., d'Avella, A., Lacquaniti, F., and Ivanenko, Y., 'Human-human interaction forces and interlimb coordination during side-by-side walking with hand contact,' Frontiers in physiology, March 2018, **9**, p. 179.

[12] Franklin, D. W., So, U., Burdet, E., and Kawato, M., 'Visual feedback is not necessary for the learning of novel dynamics,' PloS one, 2007, **2**(12), p. e1336.

[13] Batcho, C., Gagné, M., Bouyer, L., Roy, J., and Mercier, C., 'Impact of online visual feedback on motor acquisition and retention when learning to reach in a force field,' Neuroscience, 2016, **337**, pp. 267–275.

[14] Sawers, A., Bhattacharjee, T., McKay, J. L., Hackney, M. E., Kemp, C. C., and Ting, L. H., 'Small forces that differ with prior motor experience can communicate movement goals during human-human physical interaction,' Journal of neuroengineering and rehabilitation, January 2017, **14**(1), p. 8.

[15] Chen, T. L., Bhattacharjee, T., McKay, J. L., Borinski, J. E., Hackney, M. E., Ting, L. H., and Kemp, C. C., 'Evaluation by expert dancers of a robot that performs partnered stepping via haptic interaction,' PloS one, May 2015, **10**(5), p. e0125179.

[16] Mussa-Ivaldi, F. A., Hogan, N., and Bizzi, E., 'Neural, mechanical, and geometric factors subserving arm posture in humans,' Journal of Neuroscience, 1985, **5**(10), pp. 2732–2743.

[17] Regmi, S., Burns, D., and Song, Y. S., 'A robot for overground physical human-robot interaction experiments,' Submitted to PLOS One, xxyy, **xxyy**(xxyy), p. xxyy.

[18] Regmi, S. and Song, Y. S., 'Design Methodology for Robotic Manipulator for Overground Physical Interaction Tasks,' Journal of Mechanism and Robotics, August 2020, **12**(4), p. 041002.

[19] Kim, H.-Y., 'Statistical notes for clinical researchers: assessing normal distribution (2) using skewness and kurtosis,' Restorative dentistry & endodontics, 2013, **38**(1), pp. 52–54.

SECTION

3. DYNAMICS OF THE INTERACTIVE ARM

Previously, in the Paper II and the Section 4 of the Paper I, we mentioned about using a simulation model of Ophrie's interactive arm. This section presents the detailed derivation of the mathematics behind the simulation model.

Apart from its usage as a simulation model, the detailed dynamic model can be a valuable asset while designing the advanced model-based controllers such as impedance control, non-linear control, etc. In our case, we chose to use a proportional-integral-derivative (PID) controller because since the inherent inertia and damping were pretty low for our robotic arm – as found out in [17], the non-linearity induced due to them is expected to be negligible. In our robot, while implementing a stiffness controller, a position based PID force controller was used, whereas during force perturbation, a separate PID force controller was used.

The top-view schematic diagram of the arm is shown in Figure 3.1.

Let, M_1ACBM_2 represents the closed loop five link interactive arm of the robot Ophrie. The length of the proximal (M_1A and M_2B) and the distal (AC and BC) are represented by L_1, L_2, L_3, and L_4 respectively. C is the end effector of the arm on top of which the interaction handle is lodged, and $T_1T_2T_3T_4$ is the desired end-effector workspace (square area of $d \times d$). P is a point on M_1ACBM_2 plane. M_1 and M_2 represent the position where the motors are located; the motors are responsible for generating control signal τ_1 and τ_2. θ_1 and θ_2 are the angles formed by the links L_1 and L_2 in clockwise and counterclockwise direction with respect to y-axis respectively. $\psi_{(XYZ)}$ represents an angle

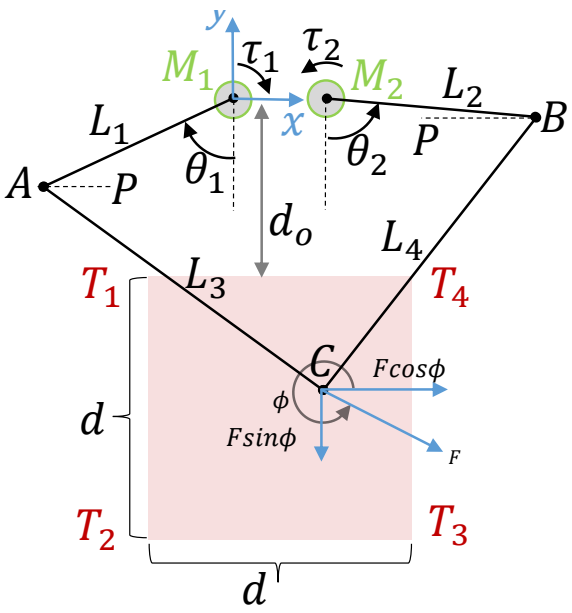

Figure 3.1. Top-view schematic representation of Ophrie's interactive arm

formed by three points X, Y and Z. F is the force applied by the robot to the environment in ϕ direction measured CCW with respect to the positive x-axis. d_0 is the distance between the motor M_1 and the nearest side of the workspace $T_1T_2T_3T_4$ (i.e. T_1T_4).

3.1. DYNAMICS OF THE INTERACTIVE ARM IN JOINT SPACE

The Cartesian coordinate of the joint positions A and B, and the end-effector C can be represented be (A_x, A_y), (B_x, B_y), and (C_x, C_y), respectively.

$$A_x = -L_1 \sin\theta_1 \tag{3.1}$$

$$A_y = -L_1 \cos\theta_1 \tag{3.2}$$

$$B_x = x_1 + L_2 \sin\theta_2 \tag{3.3}$$

$$B_y = y_1 - L_2 \cos\theta_2 \tag{3.4}$$

$$\overline{AB} = \sqrt{(A_x - B_x)^2 + (A_y - B_y)^2} \tag{3.5}$$

$$\psi_{ABP} = \arctan\left(\frac{B_y - A_y}{B_x - A_x}\right) \tag{3.6}$$

$$\psi_{BAC} = \arccos\left(\frac{\overline{AB}^2 + L_3^2 - L_4^2}{2\,\overline{AB}\,L_3}\right) \tag{3.7}$$

$$\psi_{PCA} = \psi_{BAC} - \psi_{ABP} \tag{3.8}$$

Likewise,

$$\psi_{ABC} = \arccos\left(\frac{\overline{AB}^2 + L_4^2 - L_3^2}{2\,\overline{AB}\,L_4}\right) \tag{3.9}$$

$$\psi_{PBC} = \psi_{ABC} + \psi_{PBA} \tag{3.10}$$

Hence,

$$C_x = A_x + L_4 \cos(\psi_{PCA}) \tag{3.11}$$

$$C_y = A_y - L_4 \sin(\psi_{PCA}) \tag{3.12}$$

Using Equations (3.1), (3.2) and (3.8) in Equation (3.11) and Equation (3.12), we get:

$$C_x = -L_1 \sin\theta_1 + L_4 \cos(\psi_{BAC} - \psi_{ABP}) \tag{3.13}$$

$$C_y = -L_1 \cos\theta_1 - L_4 \sin(\psi_{BAC} - \psi_{ABP}). \tag{3.14}$$

The Jacobian matrix can, now, be obtained by performing the partial derivative of C_x and C_y with respect to θ_1 and θ_2. It requires partial differentiation of ψ_{ABP} and ψ_{BAC} with respect to θ_1 and θ_2. Using Equation (3.6), we first define

$$\psi_{ABP} = \arctan(\alpha(\theta_1, \theta_2))$$

where

$$\alpha(\theta_1, \theta_2) = \frac{\alpha_n(\theta_1, \theta_2)}{\alpha_d(\theta_1, \theta_2)} = \frac{B_y - A_y}{B_x - Ax} = \frac{y_1 - L_2 \cos\theta_2 + L_1 \cos\theta_1}{x_1 + L_2 \sin\theta_2 + L_1 \sin\theta_1} \tag{3.15}$$

where α_n and α_d are both the functions of θ_1 and θ_2.

Now, let's find the partial differentiation of ψ_{ABP} with respect to θ_1 and θ_2 as in Equations (3.16) and (3.17).

$$\frac{\partial \psi_{ABP}}{\partial \theta_1} = \frac{\partial(\arctan(\alpha(\theta_1, \theta_2)))}{\partial \theta_1} = \frac{1}{1 + (\alpha_n/\alpha_d)^2} \frac{-\alpha_n L_1 \cos\theta_1 - \alpha_d L_1 \sin\theta_1}{\alpha_d^2} \tag{3.16}$$

$$\frac{\partial \psi_{ABP}}{\partial \theta_2} = \frac{\partial(\arctan(\alpha(\theta_1, \theta_2)))}{\partial \theta_2} = \frac{1}{1 + (\alpha_n/\alpha_d)^2} \frac{-\alpha_n L_2 \cos\theta_2 + \alpha_d L_2 \sin\theta_2}{\alpha_d^2} \tag{3.17}$$

Next, to get the partial differentiation of ψ_{BAC}, lets define Equation (3.7) as

$$\psi_{BAC} = \arccos(\beta(\theta_1, \theta_2))$$

where

$$\beta(\theta_1, \theta_2) = \frac{\beta_n(\theta_1, \theta_2)}{\beta_d(\theta_1, \theta_2)} = \frac{\overline{AB}^2 + L_3^2 - L_4^2}{2\,\overline{AB}\,L_3} = \frac{\alpha_n^2 + \alpha_d^2 + L_3^2 - L_4^2}{2\sqrt{\alpha_n^2 + \alpha_d^2}\,L_3} \tag{3.18}$$

where, β_n and β_d are both function of θ_1 and θ_2.

Then, we find the partial differentiation of ψ_{BAC} with respect to θ_1 and θ_2 as shown in Equations (3.19) and (3.20).

$$\frac{\partial \psi_{BAC}}{\partial \theta_1} = \frac{\partial(\arccos(\beta(\theta_1, \theta_2)))}{\partial \theta_1} = \frac{-1}{\sqrt{1 - (\beta_n/\beta_d)^2}} \frac{1}{\beta_d^2} \left(\frac{\partial \beta_n}{\partial \theta_1} \beta_d - \frac{\partial \beta_d}{\partial \theta_1} \beta_n \right) \tag{3.19}$$

$$\frac{\partial \psi_{BAC}}{\partial \theta_2} = \frac{\partial(\arccos(\beta(\theta_1, \theta_2)))}{\partial \theta_2} = \frac{-1}{\sqrt{1 - (\beta_n/\beta_d)^2}} \frac{1}{\beta_d^2} \left(\frac{\partial \beta_n}{\partial \theta_2} \beta_d - \frac{\partial \beta_d}{\partial \theta_2} \beta_n \right) \tag{3.20}$$

where

$$\frac{\partial(\beta_n)}{\partial \theta_1} = -2\,L_1\,(\alpha_n\,\sin\theta_1 - \alpha_d\,\cos\theta_1) \tag{3.21}$$

$$\frac{\partial(\beta_n)}{\partial \theta_2} = 2\,L_2\,(\alpha_n\,\sin\theta_2 + \alpha_d\,\cos\theta_2) \tag{3.22}$$

and

$$\frac{\partial \beta_d}{\partial \theta_1} = L_3(\alpha_n^2 + \alpha_d^2)^{-\frac{1}{2}} \left(\frac{\partial(\alpha_n^2)}{\partial \theta_1} + \frac{\partial(\alpha_d^2)}{\partial \theta_1} \right) \tag{3.23}$$

$$\frac{\partial \beta_d}{\partial \theta_2} = L_3(\alpha_n^2 + \alpha_d^2)^{-\frac{1}{2}}\Big(\frac{\partial(\alpha_n^2)}{\partial \theta_2} + \frac{\partial(\alpha_d^2)}{\partial \theta_2}\Big). \tag{3.24}$$

The differential term inside Equations (3.23) and (3.24) can be represented as

$$\frac{\partial(\alpha_n^2)}{\partial \theta_1} = -2\,L_1^2\,\sin\theta_1\,\cos\theta_1 - 2\,y_1\,L_1\,\sin\theta_1 + 2\,L_1\,L_2\,\sin\theta_1\cos\theta_2 \tag{3.25}$$

$$\frac{\partial(\alpha_n^2)}{\partial \theta_2} = -2\,L_2^2\,\sin\theta_2\,\cos\theta_2 + 2\,y_1\,L_2\,\sin\theta_2 + 2\,L_1\,L_2\,\sin\theta_2\cos\theta_1 \tag{3.26}$$

$$\frac{\partial(\alpha_d^2)}{\partial \theta_1} = 2\,L_1^2\,\sin\theta_1\,\cos\theta_1 + 2\,x_1\,L_1\,\cos\theta_1 + 2\,L_1\,L_2\,\sin\theta_2\cos\theta_1 \tag{3.27}$$

$$\frac{\partial(\alpha_d^2)}{\partial \theta_2} = 2\,L_2^2\,\sin\theta_2\,\cos\theta_2 + 2\,x_1\,L_2\,\cos\theta_2 + 2\,L_1\,L_2\,\sin\theta_1\cos\theta_2. \tag{3.28}$$

Given Equations (3.16), (3.17), (3.19), and (3.20), we can finally compute the Jacobian matrix, $J(\theta_1, \theta_2)$ as,

$$J(\theta_1, \theta_2) = \begin{bmatrix} \frac{\partial C_x}{\partial \theta_1} & \frac{\partial C_x}{\partial \theta_2} \\ \frac{\partial C_y}{\partial \theta_1} & \frac{\partial C_y}{\partial \theta_2} \end{bmatrix} \tag{3.29}$$

where

$$\frac{\partial C_x}{\partial \theta_1} = -L_1\cos\theta_1 - L_4\sin(\psi_{BAC} - \psi_{ABP})\Big(\frac{\partial \psi_{BAC}}{\partial \theta_1} - \frac{\partial \psi_{ABP}}{\partial \theta_1}\Big) \tag{3.30}$$

$$\frac{\partial C_x}{\partial \theta_2} = -L_4\sin(\psi_{BAC} - \psi_{ABP})\Big(\frac{\partial \psi_{BAC}}{\partial \theta_2} - \frac{\partial \psi_{ABP}}{\partial \theta_2}\Big) \tag{3.31}$$

$$\frac{\partial C_y}{\partial \theta_1} = L_1\sin\theta_1 - L_4\cos(\psi_{BAC} - \psi_{ABP})\Big(\frac{\partial \psi_{BAC}}{\partial \theta_1} - \frac{\partial \psi_{ABP}}{\partial \theta_1}\Big) \tag{3.32}$$

$$\frac{\partial C_y}{\partial \theta_2} = -L_4\cos(\psi_{BAC} - \psi_{ABP})\Big(\frac{\partial \psi_{BAC}}{\partial \theta_2} - \frac{\partial \psi_{ABP}}{\partial \theta_2}\Big). \tag{3.33}$$

Finally, we can represent the dynamics of the closed loop five link interactive arm of Ophrie as

$$M(\theta)\ddot{\theta} + V_m(\theta, \dot{\theta})\dot{\theta} + \tau_r(\dot{\theta}) + G(\theta) + \tau_d = \tau + J^T(\theta)\lambda, \tag{3.34}$$

where $\theta(t)\epsilon R^2$ is the joint space coordinate vector, $\tau(t)\epsilon R^2$ is the control input vector, $M(\theta)$ is the inertial matrix, $V_m(\theta,\dot{\theta})$ is the Coriolis/Centripetal matrix, $\tau_r(\dot{\theta})$ represents the friction terms, $G(\theta)$ is the gravity vector, and $\tau_d(t)$ represents the disturbances. $J(\theta)$ is a Jacobian matrix associated with the contact surface geometry, and λ (the 'Lagrange multiplier') is a vector of contact forces exerted from the external environment. Ophrie's interactive arm is a planar 2D robot and is always aligned parallel to the ground. Hence the effect due to $G(\theta)$ will be ignored here-onwards.

In Equation (3.34), $\theta = \begin{bmatrix}\theta_1 & \theta_2\end{bmatrix}^T$, $\tau = \begin{bmatrix}\tau_1 & \tau_2\end{bmatrix}^T$, and

$$M(\theta) = \begin{bmatrix} E_3(\theta) & E_1(\theta) \\ E_2(\theta) & E_4(\theta) \end{bmatrix} \tag{3.35}$$

$$V_m(\theta,\dot{\theta}) = \begin{bmatrix} E_5(\theta)\,\dot{\theta}_1 + \frac{1}{2}E_7(\theta)\,\dot{\theta}_2 & E_6(\theta)\,\dot{\theta}_2 + \frac{1}{2}E_7(\theta)\,\dot{\theta}_1 \\ E_{11}(\theta)\,\dot{\theta}_1 + \frac{1}{2}E_{13}(\theta)\,\dot{\theta}_2 & E_{12}(\theta)\,\dot{\theta}_2 + \frac{1}{2}E_{13}(\theta)\,\dot{\theta}_1 \end{bmatrix} \tag{3.36}$$

$$\tau_r(\theta) = \begin{bmatrix} E_8(\theta) & E_9(\theta) \\ E_9(\theta) & E_{10}(\theta) \end{bmatrix}. \tag{3.37}$$

The Jacobian matrix in Equation (3.29) can be expanded by substituting respective terms from Equations (3.30) - (3.33) as

$$J(\theta) = \begin{bmatrix} -L_4 \sin\theta_4\left(\frac{\partial\psi_{BAC}}{\partial\theta_1} - \frac{\partial\psi_{ABP}}{\partial\theta_1}\right) - L_1\cos\theta_1 & -L_4\sin\theta_4\left(\frac{\partial\psi_{BAC}}{\partial\theta_2} - \frac{\partial\psi_{ABP}}{\partial\theta_2}\right) \\ -L_4\cos\theta_4\left(\frac{\partial\psi_{BAC}}{\partial\theta_1} - \frac{\partial\psi_{ABP}}{\partial\theta_1}\right) + L_1\sin\theta_1 & -L_4\cos\theta_4\left(\frac{\partial\psi_{BAC}}{\partial\theta_2} - \frac{\partial\psi_{ABP}}{\partial\theta_2}\right) \end{bmatrix}$$

with θ_3 and θ_4 representing the angles given by

$$\theta_3 = \psi_{PBC} = \psi_{PBA} + \psi_{ABC} \qquad \theta_4 = \psi_{CAP} = \psi_{BAC} + \psi_{ABP}.$$

The Lagrange multiplier in Equation (3.34) can be represented as

$$\lambda = \begin{bmatrix} F\ \cos\phi \\ F\ \sin\phi \end{bmatrix}. \tag{3.38}$$

Lastly, the functions $E_i(\theta)$ for $i = 1, 2...13$ in Equations (3.35) - (3.37) are listed in Equations (3.39) - (3.51). Let, m_i represents the mass of the the proximal links ($i = 1, 2$) and the distal links ($i = 3, 4$). b represents the width of the links, and C represents the coefficient for angular viscous damping. The moment of inertia due to motor shaft can be estimated as $\frac{1}{2}m_{ms}r_{ms}^2$ where m_{ms} is the mass of motor shaft and r_{ms} is the radius of the motor shaft.

$$\begin{aligned} E_1(\theta) = \Big[& -\frac{1}{2}m_3 L_2 L_3 \sin(\theta_2 - \theta_3)\Big(\frac{\partial\psi_{ABP}}{\partial\theta_1} + \frac{\partial\psi_{BAC}}{\partial\theta_1}\Big) + \frac{1}{3}m_3\Big(L_3^2 + \frac{1}{4}b^2\Big) \\ & \Big(\frac{\partial\psi_{ABP}}{\partial\theta_1} + \frac{\partial\psi_{BAC}}{\partial\theta_1}\Big)\Big(\frac{\partial\psi_{ABP}}{\partial\theta_2} + \frac{\partial\psi_{BAC}}{\partial\theta_2}\Big) - \frac{1}{2}m_4 L_1 L_4 \sin(\theta_1 - \theta_4)\Big(\frac{\partial\psi_{BAC}}{\partial\theta_2} - \frac{\partial\psi_{ABP}}{\partial\theta_2}\Big) \\ & + \frac{1}{3}m_4\Big(L_4^2 + \frac{1}{4}b^2\Big)\Big(\frac{\partial\psi_{BAC}}{\partial\theta_1} - \frac{\partial\psi_{ABP}}{\partial\theta_1}\Big)\Big(\frac{\partial\psi_{BAC}}{\partial\theta_2} - \frac{\partial\psi_{ABP}}{\partial\theta_2}\Big)\Big] \end{aligned} \tag{3.39}$$

$$\begin{aligned} E_2(\theta) = \Big[& -\frac{1}{2}m_3 L_2 L_3 \sin(\theta_2 - \theta_3)\Big(\frac{\partial\psi_{ABP}}{\partial\theta_1} + \frac{\partial\psi_{BAC}}{\partial\theta_1}\Big) + \frac{1}{3}m_3\Big(L_3^2 + \frac{1}{4}b^2\Big) \\ & \Big(\frac{\partial\psi_{ABP}}{\partial\theta_1} + \frac{\partial\psi_{BAC}}{\partial\theta_1}\Big)\Big(\frac{\partial\psi_{ABP}}{\partial\theta_2} + \frac{\partial\psi_{BAC}}{\partial\theta_2}\Big) - \frac{1}{2}m_4 L_1 L_4 \sin(\theta_1 - \theta_4)\Big(\frac{\partial\psi_{BAC}}{\partial\theta_2} - \frac{\partial\psi_{ABP}}{\partial\theta_2}\Big) \\ & + \frac{1}{3}m_4\Big(L_4^2 + \frac{1}{4}b^2\Big)\Big(\frac{\partial\psi_{BAC}}{\partial\theta_1} - \frac{\partial\psi_{ABP}}{\partial\theta_1}\Big)\Big(\frac{\partial\psi_{BAC}}{\partial\theta_2} - \frac{\partial\psi_{ABP}}{\partial\theta_2}\Big)\Big] \end{aligned} \tag{3.40}$$

(Note that E_1 and E_2 are identical.)

$$E_3(\theta) = \Big[\frac{1}{3}m_3\Big(L_3^2 + \frac{1}{4}b^2\Big) + \frac{1}{2}\Big(\frac{1}{2}m_{ms}r_{ms}^2\Big) + m_4L_1^2 - m_4L_1L_4\sin(\theta_1 - \theta_4)$$
$$\Big(\frac{\partial\psi_{BAC}}{\partial\theta_1} - \frac{\partial\psi_{ABP}}{\partial\theta_1}\Big) + \frac{1}{3}m_3\Big(L_3^2 + \frac{1}{4}b^2\Big)\Big(\frac{\partial\psi_{ABP}}{\partial\theta_1} + \frac{\partial\psi_{BAC}}{\partial\theta_1}\Big)^2 + \frac{1}{3}m_4\Big(L_4^2 + \frac{1}{4}b^2\Big)$$
$$\Big(\frac{\partial\psi_{BAC}}{\partial\theta_1} - \frac{\partial\psi_{ABP}}{\partial\theta_1}\Big)^2\Big] \tag{3.41}$$

$$E_4(\theta) = \Big[\frac{1}{3}m_2\Big(L_2^2 + \frac{1}{4}b^2\Big) + \frac{1}{2}\Big(\frac{1}{2}m_{ms}r_{ms}^2\Big) + m_3L_2^2 - m_3L_2L_3\sin(\theta_2 - \theta_3)$$
$$\Big(\frac{\partial\psi_{ABP}}{\partial\theta_2} + \frac{\partial\psi_{BAC}}{\partial\theta_2}\Big) + \frac{1}{3}m_3\Big(L_3^2 + \frac{1}{4}b^2\Big)\Big(\frac{\partial\psi_{ABP}}{\partial\theta_2} + \frac{\partial\psi_{BAC}}{\partial\theta_2}\Big)^2 + \frac{1}{3}m_4\Big(L_4^2 + \frac{1}{4}b^2\Big)$$
$$\Big(\frac{\partial\psi_{BAC}}{\partial\theta_2} - \frac{\partial\psi_{ABP}}{\partial\theta_2}\Big)^2\Big] \tag{3.42}$$

$$\begin{aligned} E_5(\theta) = \Big[&\frac{1}{3}m_3\Big(L_3^2 + \frac{1}{4}b^2\Big)\Big(\frac{\partial\psi_{ABP}}{\partial\theta_1} + \frac{\partial\psi_{BAC}}{\partial\theta_1}\Big)\Big(\frac{\partial^2\psi_{ABP}}{\partial\theta_1^2} + \frac{\partial^2\psi_{BAC}}{\partial\theta_1^2}\Big) \\ &- \frac{1}{2}m_4L_1L_4\sin(\theta_1 - \theta_4)\Big(\frac{\partial^2\psi_{BAC}}{\partial\theta_1^2} - \frac{\partial^2\psi_{ABP}}{\partial\theta_1^2}\Big) \\ &+ \frac{1}{3}m_4\Big(L_4^2 + \frac{1}{4}b^2\Big)\Big(\frac{\partial\psi_{BAC}}{\partial\theta_1} - \frac{\partial\psi_{ABP}}{\partial\theta_1}\Big)\Big(\frac{\partial^2\psi_{BAC}}{\partial\theta_1^2} - \frac{\partial^2\psi_{ABP}}{\partial\theta_1^2}\Big) \\ &- \frac{1}{2}m_4L_1L_4\cos(\theta_1 - \theta_4)\Big(1 + \frac{\partial\psi_{ABP}}{\partial\theta_1} - \frac{\partial\psi_{BAC}}{\partial\theta_1}\Big)\Big(\frac{\partial\psi_{BAC}}{\partial\theta_1} - \frac{\partial\psi_{ABP}}{\partial\theta_1}\Big)\Big] \end{aligned} \tag{3.43}$$

$$\begin{aligned} E_6(\theta) = \Big[&-\frac{1}{2}m_3L_2L_3\cos(\theta_2 - \theta_3)\Big(\frac{\partial\psi_{ABP}}{\partial\theta_1} + \frac{\partial\psi_{BAC}}{\partial\theta_1}\Big) \\ &- \frac{1}{2}m_4L_1L_4\sin(\theta_1 - \theta_4)\Big(\frac{\partial^2\psi_{BAC}}{\partial\theta_2^2} - \frac{\partial^2\psi_{ABP}}{\partial\theta_2^2}\Big) \\ &+ \frac{1}{3}m_3\Big(L_3^2 + \frac{1}{4}b^2\Big)\Big(\frac{\partial\psi_{ABP}}{\partial\theta_1} + \frac{\partial\psi_{BAC}}{\partial\theta_1}\Big)\Big(\frac{\partial^2\psi_{ABP}}{\partial\theta_2^2} + \frac{\partial^2\psi_{BAC}}{\partial\theta_2^2}\Big) \\ &+ \frac{1}{3}m_4\Big(L_4^2 + \frac{1}{4}b^2\Big)\Big(\frac{\partial\psi_{BAC}}{\partial\theta_1} - \frac{\partial\psi_{ABP}}{\partial\theta_1}\Big)\Big(\frac{\partial^2\psi_{BAC}}{\partial\theta_2^2} - \frac{\partial^2\psi_{ABP}}{\partial\theta_2^2}\Big) \\ &+ \frac{1}{2}m_4L_1L_4\cos(\theta_1 - \theta_4)\Big(\frac{\partial\psi_{BAC}}{\partial\theta_2} - \frac{\partial\psi_{ABP}}{\partial\theta_2}\Big)^2\Big] \end{aligned} \tag{3.44}$$

$$
\begin{aligned}
E_7(\theta) = \Big[&+ \frac{1}{3}m_3\Big(2L_3^2 + \frac{1}{2}b^2\Big)\Big(\frac{\partial\psi_{ABP}}{\partial\theta_1} + \frac{\partial\psi_{BAC}}{\partial\theta_1}\Big)\Big(\frac{\partial^2\psi_{ABP}}{\partial\theta_1\partial\theta_2} + \frac{\partial^2\psi_{BAC}}{\partial\theta_1\partial\theta_2}\Big) \\
&- m_4L_1L_4\sin(\theta_1-\theta_4)\Big(\frac{\partial^2\psi_{BAC}}{\partial\theta_1\partial\theta_2} - \frac{\partial^2\psi_{ABP}}{\partial\theta_1\partial\theta_2}\Big) \\
&+ m_4L_1L_4\cos(\theta_1-\theta_4)\Big(\frac{\partial\psi_{BAC}}{\partial\theta_2} - \frac{\partial\psi_{ABP}}{\partial\theta_2}\Big)\Big(\frac{\partial\psi_{BAC}}{\partial\theta_1} - \frac{\partial\psi_{ABP}}{\partial\theta_1}\Big) \\
&+ \frac{1}{3}m_4\Big(2L_4^2 + \frac{1}{2}b^2\Big)\Big(\frac{\partial\psi_{BAC}}{\partial\theta_1} - \frac{\partial\psi_{ABP}}{\partial\theta_1}\Big)\Big(\frac{\partial^2\psi_{BAC}}{\partial\theta_1\partial\theta_2} - \frac{\partial^2\psi_{ABP}}{\partial\theta_1\partial\theta_2}\Big)\Big]
\end{aligned}
\tag{3.45}
$$

$$
E_8(\theta) = \Big[6C\Big(\frac{\partial\psi_{BAC}}{\partial\theta_1}\Big)^2 + 2C\Big(\frac{\partial\psi_{ABP}}{\partial\theta_1}\Big)^2\Big] \tag{3.46}
$$

$$
E_9(\theta) = \Big[6C\Big(\frac{\partial\psi_{BAC}}{\partial\theta_1}\Big)\Big(\frac{\partial\psi_{BAC}}{\partial\theta_2}\Big) + 2C\Big(\frac{\partial\psi_{ABP}}{\partial\theta_1}\Big)\Big(\frac{\partial\psi_{ABP}}{\partial\theta_2}\Big)\Big] \tag{3.47}
$$

$$
E_{10}(\theta) = \Big[6C\Big(\frac{\partial\psi_{BAC}}{\partial\theta_2}\Big)^2 + 2C\Big(\frac{\partial\psi_{ABP}}{\partial\theta_2}\Big)^2\Big] \tag{3.48}
$$

$$
\begin{aligned}
E_{11}(\theta) = \Big[&- \frac{1}{2}m_4L_1L_4\cos(\theta_1-\theta_4)\Big(\frac{\partial\psi_{BAC}}{\partial\theta_2} - \frac{\partial\psi_{ABP}}{\partial\theta_2}\Big) \\
&- \frac{1}{2}m_3L_2L_3\sin(\theta_2-\theta_2)\Big(\frac{\partial^2\psi_{ABP}}{\partial\theta_1^2} + \frac{\partial^2\psi_{BAC}}{\partial\theta_1^2}\Big) \\
&+ \frac{1}{3}m_3\Big(L_3^2 + \frac{1}{4}b^2\Big)\Big(\frac{\partial^2\psi_{ABP}}{\partial\theta_1^2} + \frac{\partial^2\psi_{BAC}}{\partial\theta_1^2}\Big)\Big(\frac{\partial\psi_{ABP}}{\partial\theta_2} + \frac{\partial\psi_{BAC}}{\partial\theta_2}\Big) \\
&+ \frac{1}{3}m_4\Big(L_4^2 + \frac{1}{4}b^2\Big)\Big(\frac{\partial^2\psi_{BAC}}{\partial\theta_1^2} - \frac{\partial^2\psi_{ABP}}{\partial\theta_1^2}\Big)\Big(\frac{\partial\psi_{BAC}}{\partial\theta_2} - \frac{\partial\psi_{ABP}}{\partial\theta_2}\Big) \\
&+ \frac{1}{2}m_3L_2L_3\cos(\theta_2-\theta_3)\Big(\frac{\partial\psi_{ABP}}{\partial\theta_1} + \frac{\partial\psi_{BAC}}{\partial\theta_1}\Big)^2\Big]
\end{aligned}
\tag{3.49}
$$

$$
\begin{aligned}
E_{12}(\theta) = \Big[&\frac{1}{3}m_3\Big(L_3^2 + \frac{1}{4}b^2\Big)\Big(\frac{\partial^2\psi_{ABP}}{\partial\theta_2^2} + \frac{\partial^2\psi_{BAC}}{\partial\theta_2^2}\Big)\Big(\frac{\partial\psi_{ABP}}{\partial\theta_2} + \frac{\partial\psi_{BAC}}{\partial\theta_2}\Big) \\
&- \frac{1}{2}m_3L_2L_3\sin(\theta_2-\theta_3)\Big(\frac{\partial^2\psi_{ABP}}{\partial\theta_2^2} + \frac{\partial^2\psi_{BAC}}{\partial\theta_2^2}\Big) \\
&+ \frac{1}{3}m_4\Big(L_4^2 + \frac{1}{4}b^2\Big)\Big(\frac{\partial^2\psi_{BAC}}{\partial\theta_2^2} - \frac{\partial^2\psi_{ABP}}{\partial\theta_2^2}\Big)\Big(\frac{\partial\psi_{BAC}}{\partial\theta_2} - \frac{\partial\psi_{ABP}}{\partial\theta_2}\Big) \\
&- \frac{1}{2}m_3L_2L_3\cos(\theta_2-\theta_3)\Big(1 - \frac{\partial\psi_{ABP}}{\partial\theta_2} - \frac{\partial\psi_{BAC}}{\partial\theta_2}\Big)\Big(\frac{\partial\psi_{ABP}}{\partial\theta_2} + \frac{\partial\psi_{BAC}}{\partial\theta_2}\Big)\Big]
\end{aligned}
\tag{3.50}
$$

$$
\begin{aligned}
E_{13}(\theta) = \Big[& + \frac{1}{3} m_3 \Big(L_3^2 + \frac{1}{4} b^2 \Big) \Big(\frac{\partial^2 \psi_{ABP}}{\partial \theta_1 \partial \theta_2} + \frac{\partial^2 \psi_{BAC}}{\partial \theta_1 \partial \theta_2} \Big) \Big(\frac{\partial \psi_{ABP}}{\partial \theta_2} + \frac{\partial \psi_{BAC}}{\partial \theta_2} \Big) \\
& - m_3 L_2 L_3 \sin(\theta_2 - \theta_3) \Big(\frac{\partial^2 \psi_{ABP}}{\partial \theta_1 \partial \theta_2} + \frac{\partial^2 \psi_{BAC}}{\partial \theta_1 \partial \theta_2} \Big) \\
& + m_3 L_2 L_3 \cos(\theta_2 - \theta_3) \Big(\frac{\partial \psi_{ABP}}{\partial \theta_1} + \frac{\partial \psi_{BAC}}{\partial \theta_1} \Big) \Big(\frac{\partial \psi_{ABP}}{\partial \theta_2} + \frac{\partial \psi_{BAC}}{\partial \theta_2} \Big) \\
& + \frac{1}{3} m_4 \Big(L_4^2 + \frac{1}{4} b^2 \Big) \Big(\frac{\partial^2 \psi_{BAC}}{\partial \theta_1 \partial \theta_2} - \frac{\partial^2 \psi_{ABP}}{\partial \theta_1 \partial \theta_2} \Big) \Big(\frac{\partial \psi_{BAC}}{\partial \theta_2} - \frac{\partial \psi_{ABP}}{\partial \theta_2} \Big) \Big]
\end{aligned}
\tag{3.51}
$$

3.2. DYNAMICS OF THE INTERACTIVE ARM IN CARTESIAN SPACE

Let X represent the coordinate of the end-effector in Cartesian space (workspace) at any instant.

$$
X = \begin{bmatrix} C_x \\ C_y \end{bmatrix} \tag{3.52}
$$

where C_x and C_y can be obtained by using Equations (3.11) and (3.12), respectively. Hence, X is the function of joint angles (θ_i), which are themselves the function of time (t).

$$
X(t) = f(\theta(t)) \tag{3.53}
$$

with $X \epsilon R^2$ and $\theta \epsilon R^2$.

Differentiating Equation (3.53) with respect to t results,

$$
\dot{X} = J(\theta)\, \dot{\theta} \tag{3.54}
$$

$$
\therefore \;\; \dot{\theta} = J(\theta)^{-1} \dot{X} \tag{3.55}
$$

And, differentiating Equation (3.54) with respect to t results,

$$
\ddot{X} = \dot{J}(\theta)\, \dot{\theta} + J(\theta)\, \ddot{\theta} \tag{3.56}
$$

Substituting Equations (3.55) in (3.56) and rearranging

$$\ddot{\theta} = J(\theta)^{-1}\ddot{X} - J(\theta)^{-1}\,\dot{J}(\theta)\,J(\theta)^{-1}\dot{X} \tag{3.57}$$

Substituting Equations (3.55) and (3.57) in (3.34), we get

$$M(\theta)J(\theta)^{-1}\ddot{X} - M(\theta)J(\theta)^{-1}\,\dot{J}(\theta)\,J(\theta)^{-1}\dot{X} + V_m(\theta,\dot{\theta})\,J(\theta)^{-1}\dot{X} + \tau_r(\theta)\,J(\theta)^{-1}\dot{X} + G(\theta) + \tau_d = \tau + J^T(\theta)\lambda \tag{3.58}$$

Multiplying both sides by $J(\theta)^{-T}$, we get

$$J(\theta)^{-T}\,M(\theta)J(\theta)^{-1}\ddot{X} - J(\theta)^{-T}\,[M(\theta)\,J(\theta)^{-1}\,\dot{J}(\theta)\,J(\theta)^{-1}\dot{X} + V_m(\theta,\dot{\theta})\,J(\theta)^{-1}\dot{X} + \tau_r(\theta)\,J(\theta)^{-1}\dot{X} + G(\theta) + \tau_d] = J(\theta)^{-T}\,\tau + \lambda \tag{3.59}$$

Representing $M^* = J(\theta)^{-T}\,M(\theta)J(\theta)^{-1}$, $h^* = [M^*\,\dot{J}(\theta)\,J(\theta)^{-1} + J(\theta)^{-T}\,V_m(\theta,\dot{\theta})\,J(\theta)^{-1}]$, $K = J(\theta)^{-T}\,[G(\theta) + \tau_d]$, and $F_r^* = J(\theta)^{-T}\,\tau_r(\theta)\,J(\theta)^{-1}$, we get

$$M^*\,\ddot{X} + (h^* + F_r^*)\,\dot{X} + K = F + \lambda \tag{3.60}$$

where, $F = J(\theta)^{-T}\,\tau$. F has to be found out so as to apply appropriate control on actuators.

Equation (3.60) contains $\dot{J}$, which can be obtained by differentiating Equation (3.29) with respect to t.

$$\dot{J}(\theta_1,\theta_2) = \begin{bmatrix} \frac{d}{dt}\frac{\partial C_x}{\partial \theta_1} & \frac{d}{dt}\frac{\partial C_x}{\partial \theta_2} \\ \frac{d}{dt}\frac{\partial C_y}{\partial \theta_1} & \frac{d}{dt}\frac{\partial C_y}{\partial \theta_2} \end{bmatrix} \tag{3.61}$$

where

$$\frac{d}{dt}\frac{\partial C_x}{\partial \theta_1} = L_1 \sin\theta_1\,\dot{\theta}_1 - L_4 \cos(\psi_{BAC} - \psi_{ABP})\left(\frac{d\,\psi_{BAC}}{dt} - \frac{d\,\psi_{ABP}}{dt}\right)\left(\frac{\partial \psi_{BAC}}{\partial \theta_1} - \frac{\partial \psi_{ABP}}{\partial \theta_1}\right) - L_4 \sin(\psi_{BAC} - \psi_{ABP})\left(\frac{d}{dt}\frac{\partial \psi_{BAC}}{\partial \theta_1} - \frac{d}{dt}\frac{\partial \psi_{ABP}}{\partial \theta_1}\right) \tag{3.62}$$

$$\frac{d}{dt}\frac{\partial C_x}{\partial \theta_2} = -L_4 \cos(\psi_{BAC} - \psi_{ABP})\left(\frac{d\,\psi_{BAC}}{dt} - \frac{d\,\psi_{ABP}}{dt}\right)\left(\frac{\partial \psi_{BAC}}{\partial \theta_2} - \frac{\partial \psi_{ABP}}{\partial \theta_2}\right) - L_4 \sin(\psi_{BAC} - \psi_{ABP})\left(\frac{d}{dt}\frac{\partial \psi_{BAC}}{\partial \theta_2} - \frac{d}{dt}\frac{\partial \psi_{ABP}}{\partial \theta_2}\right) \tag{3.63}$$

$$\frac{d}{dt}\frac{\partial C_y}{\partial \theta_1} = L_1 \cos\theta_1\,\dot{\theta}_1 + L_4 \sin(\psi_{BAC} - \psi_{ABP})\left(\frac{d\,\psi_{BAC}}{dt} - \frac{d\,\psi_{ABP}}{dt}\right)\left(\frac{\partial \psi_{BAC}}{\partial \theta_1} - \frac{\partial \psi_{ABP}}{\partial \theta_1}\right) - L_4 \cos(\psi_{BAC} - \psi_{ABP})\left(\frac{d}{dt}\frac{\partial \psi_{BAC}}{\partial \theta_1} - \frac{d}{dt}\frac{\partial \psi_{ABP}}{\partial \theta_1}\right) \tag{3.64}$$

$$\frac{d}{dt}\frac{\partial C_y}{\partial \theta_2} = L_4 \sin(\psi_{BAC} - \psi_{ABP})\left(\frac{d\,\psi_{BAC}}{dt} - \frac{d\,\psi_{ABP}}{dt}\right)\left(\frac{\partial \psi_{BAC}}{\partial \theta_2} - \frac{\partial \psi_{ABP}}{\partial \theta_2}\right) - L_4 \cos(\psi_{BAC} - \psi_{ABP})\left(\frac{d}{dt}\frac{\partial \psi_{BAC}}{\partial \theta_2} - \frac{d}{dt}\frac{\partial \psi_{ABP}}{\partial \theta_2}\right) \tag{3.65}$$

where

$$\frac{d\,\psi_{BAC}}{dt} = -\frac{1}{\sqrt{1 - \left(\frac{\beta_n}{\beta_d}\right)^2}}\,\frac{1}{(\beta_d)^2}\left(\frac{d\beta_n}{dt}\beta_d - \frac{d\beta_d}{dt}\beta_n\right) \tag{3.66}$$

$$\frac{d\,\psi_{ABP}}{dt} = \frac{1}{\alpha_n^2 + \alpha_d^2}\left(\frac{d\alpha_n}{dt}\alpha_d - \frac{d\alpha_d}{dt}\alpha_n\right) \tag{3.67}$$

where

$$\frac{d\,\beta_n}{dt} = 2(A_x - B_x)\left(-L_1 \cos\theta_1\,\dot{\theta}_1 - L_2 \cos\theta_2\,\dot{\theta}_2\right) + 2(A_y - B_y)\left(L_1 \sin\theta_1\,\dot{\theta}_1 - L_2 \sin\theta_2\,\dot{\theta}_2\right) \tag{3.68}$$

$$\frac{d\,\beta_d}{dt} = \frac{L_3}{\overline{AB}}\frac{d\,\beta_n}{dt} \tag{3.69}$$

$$\frac{d\,\alpha_n}{dt} = L_2 \sin\theta_2\,\dot{\theta}_2 - L_1 \sin\theta_1\,\dot{\theta}_1 \tag{3.70}$$

$$\frac{d\,\alpha_d}{dt} = L_2 \cos\theta_2\,\dot{\theta}_2 + L_1 \cos\theta_1\,\dot{\theta}_1 \tag{3.71}$$

For Equations (3.62) to (3.65), we also need

$$\frac{d}{dt}\frac{\partial \psi_{BAC}}{\partial \theta_1} = \frac{\begin{array}{r} -\beta_d^2\sqrt{1-\left(\frac{\beta_n}{\beta_d}\right)^2}\left(\beta_d \frac{d}{dt}\frac{\partial \beta_n}{\partial \theta_1} + \frac{\partial \beta_n}{\partial \theta_1}\frac{d\beta_d}{dt} - \beta_n \frac{d}{dt}\frac{\partial \beta_d}{\partial \theta_1} - \frac{\partial \beta_d}{\partial \theta_1}\frac{d\beta_n}{dt}\right) \\ -\frac{\partial \psi_{BAC}}{\partial \theta_1}\left(2\beta_d^3\frac{d\beta_d}{dt} - \beta_n^2\beta_d\frac{d\beta_d}{dt} - \beta_d^2\beta_n\frac{d\beta_n}{dt}\right)\end{array}}{\beta_d^4 - \beta_n^2\beta_d^2} \tag{3.72}$$

$$\frac{d}{dt}\frac{\partial \psi_{BAC}}{\partial \theta_2} = \frac{\begin{array}{r} -\beta_d^2\sqrt{1-\left(\frac{\beta_n}{\beta_d}\right)^2}\left(\beta_d \frac{d}{dt}\frac{\partial \beta_n}{\partial \theta_2} + \frac{\partial \beta_n}{\partial \theta_2}\frac{d\beta_d}{dt} - \beta_n \frac{d}{dt}\frac{\partial \beta_d}{\partial \theta_2} - \frac{\partial \beta_d}{\partial \theta_2}\frac{d\beta_n}{dt}\right) \\ -\frac{\partial \psi_{BAC}}{\partial \theta_2}\left(2\beta_d^3\frac{d\beta_d}{dt} - \beta_n^2\beta_d\frac{d\beta_d}{dt} - \beta_d^2\beta_n\frac{d\beta_n}{dt}\right)\end{array}}{\beta_d^4 - \beta_n^2\beta_d^2} \tag{3.73}$$

$$\frac{d}{dt}\frac{\partial \psi_{ABP}}{\partial \theta_1} = \frac{\begin{array}{r}(\alpha_n^2+\alpha_d^2)\left(-L_1\cos\theta_1\frac{d\alpha_n}{dt} + \alpha_n L_1 \sin\theta_1\dot{\theta}_1 - L_1\sin\theta_1\frac{d\alpha_d}{dt} - \alpha_d L_1\cos\theta_1\,\dot{\theta}_1\right) \\ +(\alpha_n L_1\cos\theta_1 + \alpha_d L_1\sin\theta_1)\left(2\alpha_d\frac{d\alpha_d}{dt} + 2\alpha_n\frac{d\alpha_n}{dt}\right)\end{array}}{(\alpha_n^2+\alpha_d^2)^2} \tag{3.74}$$

$$\frac{d}{dt}\frac{\partial \psi_{ABP}}{\partial \theta_2} = \frac{\begin{array}{r}(\alpha_n^2+\alpha_d^2)\left(-L_2\cos\theta_2\frac{d\alpha_n}{dt} + \alpha_n L_2 \sin\theta_2\dot{\theta}_2 + L_2\sin\theta_2\frac{d\alpha_d}{dt} + \alpha_d L_2\cos\theta_2\,\dot{\theta}_2\right) \\ -(-\alpha_n L_2\cos\theta_2 + \alpha_d L_2\sin\theta_2)\left(2\alpha_d\frac{d\alpha_d}{dt} + 2\alpha_n\frac{d\alpha_n}{dt}\right)\end{array}}{(\alpha_n^2+\alpha_d^2)^2} \tag{3.75}$$

where,

$$\frac{d}{dt}\frac{\partial \beta_d}{\partial \theta_1} = \frac{L_3\sqrt{(\alpha_n^2+\alpha_d^2)}\left(\frac{d}{dt}\frac{\partial \alpha_n^2}{\partial \theta_1} + \frac{d}{dt}\frac{\partial \alpha_d^2}{\partial \theta_1}\right) - L_3\frac{\partial \beta_d}{\partial \theta_1}\left(\alpha_n\frac{d\alpha_n}{dt} + \alpha_d\frac{d\alpha_d}{dt}\right)}{\alpha_n^2+\alpha_d^2} \tag{3.76}$$

$$\frac{d}{dt}\frac{\partial \beta_d}{\partial \theta_2} = \frac{L_3\sqrt{(\alpha_n^2+\alpha_d^2)}\left(\frac{d}{dt}\frac{\partial \alpha_n^2}{\partial \theta_2} + \frac{d}{dt}\frac{\partial \alpha_d^2}{\partial \theta_2}\right) - L_3\frac{\partial \beta_d}{\partial \theta_2}\left(\alpha_n\frac{d\alpha_n}{dt} + \alpha_d\frac{d\alpha_d}{dt}\right)}{\alpha_n^2+\alpha_d^2} \tag{3.77}$$

$$\frac{d}{dt}\frac{\partial \beta_n}{\partial \theta_1} = -2L_1\left(\sin\theta_1\frac{d\alpha_n}{dt} + \alpha_n\cos\theta_1\,\dot{\theta}_1 - \cos\theta_1\frac{d\alpha_d}{dt} + \alpha_d\sin\theta_1\,\dot{\theta}_1\right) \tag{3.78}$$

$$\frac{d}{dt}\frac{\partial \beta_n}{\partial \theta_2} = 2L_2\left(\sin\theta_2\frac{d\alpha_n}{dt} + \alpha_n\cos\theta_2\,\dot{\theta}_2 + \cos\theta_2\frac{d\alpha_d}{dt} - \alpha_d\sin\theta_2\,\dot{\theta}_2\right) \tag{3.79}$$

For Equations (3.76) to (3.79), we also need

$$\frac{d}{dt}\frac{\partial \alpha_n^2}{\partial \theta_1} = -2L_1^2\, cos2\theta_1\, \dot{\theta}_1 - 2y_1 L_1 \cos\theta_1\, \dot{\theta}_1 + 2L_1 L_2(\cos\theta_1 \cos\theta_2\, \dot{\theta}_1 - \sin\theta_1 \sin\theta_2\, \dot{\theta}_2) \tag{3.80}$$

$$\frac{d}{dt}\frac{\partial \alpha_n^2}{\partial \theta_2} = -2L_2^2\, cos2\theta_2\ \dot{\theta}_2 + 2y_1 L_2 \cos\theta_2\, \dot{\theta}_2 + 2L_1 L_2(\cos\theta_1 \cos\theta_2\, \dot{\theta}_2 - \sin\theta_1 \sin\theta_2\, \dot{\theta}_1) \tag{3.81}$$

$$\frac{d}{dt}\frac{\partial \alpha_d^2}{\partial \theta_1} = 2L_1^2\, cos2\theta_1\, \dot{\theta}_1 - 2x_1 L_1 \sin\theta_1\, \dot{\theta}_1 + 2L_1 L_2(\cos\theta_1 \cos\theta_2\, \dot{\theta}_2 - \sin\theta_1 \sin\theta_2\, \dot{\theta}_1) \tag{3.82}$$

$$\frac{d}{dt}\frac{\partial \alpha_d^2}{\partial \theta_2} = 2L_2^2\, cos2\theta_2\ \dot{\theta}_2 - 2x_1 L_2 \sin\theta_2\, \dot{\theta}_2 + 2L_1 L_2(\cos\theta_1 \cos\theta_2\, \dot{\theta}_1 - \sin\theta_1 \sin\theta_2\, \dot{\theta}_2) \tag{3.83}$$

4. SUMMARY AND CONCLUSIONS

Overground pHRI experiments are essential to understanding human communication during physical interaction. Since no robot is available for such experiment, a robot was developed capable of performing overground physical interaction with humans. This dissertation details the design and development of the same robot and reports some experiments and preliminary results of overground pHRI experiments.

Knowing that we humans use our arms during physical interaction, it was clear that more attention should be given to the robotic manipulator – the interactive arm. From the existing knowledge of pHHI, the unique characteristics that the interactive arm should possess were outlined, such as boasting inherently low impedance, being capable of applying low force perturbation and measuring interaction force accurately, etc. [Paper I]. A design of the interactive arm was drafted. The proposed design's capability to meet the outlined characteristics was verified even before fabricating a prototype using a MATLAB simulation model [Paper II]. After the interactive arm was built, it was lodged on top of a custom frame, which itself sat on top of a mobile four-wheel robot.

After Ophrie was fully functional, a few trials of the pHRI experiment ensured that Ophrie was well up to the mark to what we had envisioned. It was fully capable of leading human participants in an overground pHRI task and, at the same time, was able to capture all the required dynamics to estimate human arm impedance [Paper III].

Human arm impedance has been studied for decades but has been primarily focused on seated pHRI tasks. Hence, a new arm impedance estimation method was proposed to extend the applicability of traditional and existing approaches to overground experiments [Paper III]. The proposed method might not be an ideal way to deal with the arm impedance, but this first step certainly helps analyze how the dynamical response of the human arm changes based on different situations.

The fourth paper extensively discussed how the human nervous system modulates the arm dynamics to enable smooth motor communication during overground physical interaction with an external agent. During the pHRI experiment conducted in our laboratory setting, Ophire led the blindfolded human participants in guided walking tasks and recorded the arm dynamics of the participant throughout the trials. Using the recorded information, we estimated the participant's arm impedance at two different locations in the walking path. We noticed that we, humans, tend to lower our arm impedance when we anticipate any motor information from the interacting partner – i.e., Ophire in this experiment. Based on this, we concluded that the human nervous system lowers the arm impedance to capture the motor intent (i.e., interaction forces and motion) from the interacting partner sensitively. This is significant because this implied that, during overground pHRI, communication was enabled through sensing movements rather than the interaction force itself.

Ophrie played a crucial role during pHRI experiments in a laboratory setting. It perturbed the human arm at the specified locations with accurate target force and, simultaneously, measured human arm response – i.e., interaction forces and motions. Participants completed each trial successfully as instructed, and we did not notice any hesitance or reluctance of the subjects to continue the trials during the experiments regarding experiment design or interacting with the robot. We believe that the demonstration of Ophrie's ability to perform an overground pHRI experiment and record the interaction dynamics is an important first step.

When physically interacting robots were first introduced for seated pHRI experiments, they quickly became invaluable tools not only for research but also for rehabilitation and physical therapies. We expect Ophrie to provide a similar impact not only in overground pHRI research but also in overground rehabilitation.

5. RECOMMENDATIONS

A workspace size of 0.15x0.15m^2 was one of the requirements set while designing Ophrie's interactive arm [Paper I]. It served its purpose as intended. As a safety feature, the robot was programmed to force stop if the handle goes out of the specified workspace during the overground pHRI experiment. Most of the trials were completed without the need for repetition because of the robot getting force-stopped. It might, partly, be because the participants were instructed to try to maintain their hand position around the center of the workspace. The presence of background stiffness might have also played a significant role. However, a bigger workspace is desirable if the robot is used for experiments where subjects should be asked 'not to intervene to the perturbation.' The current workspace can be widened by replacing the links following the procedures discussed in Paper I.

Even though we did not notice any hesitance or reluctance from the subjects regarding Ophrie's interactive behavior or its overall design, a lighter design would add an aesthetic appeal to the robot.

Furthermore, the mobile robot base was purchased with preinstalled wheel encoders and a motor driver. For better performance, replacing the encoders with higher resolution ones is recommended. The motor driver can also be custom developed. It will provide more flexibility to handle the encoder feedback to the motor controller and the output control command. Likewise, the trajectory tracking performance can be improved by adding lasers or camera feedback in addition to encoder feedback.

Since the wheeled base of Ophrie takes simple velocity commands (linear and angular) and executes it at a slow rate of 40 Hz, the base is not ideal for feedback control for adapting to quick changes in the commands. In addition, the wheel controllers have a predefined velocity profile along which the velocity increases or decreases. This is acceptable for when the robot is leading and the human partner is following, but may not be suitable for following an arbitrary trajectory of a human leader. In the current work where

we focused on assigning the leader role to the robot, Ophrie worked perfectly fine. This also helped reduce variability in the experimental trials that may arise from variable robot trajectories. Having Ophrie as the leader also simulates a potential pHRI task of assisting people to walk. A hierarchical controller that takes advantage of the fast and accurate robot arm control while the base slowly adjusts to the human lead may allow Ophrie to take a follower role in the future.

Last but not least, like any other mechatronics system, the robot Ophri also has room for improvements from its controller design to replacing the force/torque sensor with a higher resolution one, improving error handling technique, etc. Likewise, the power source to the mobile base, which currently is a rechargeable lithium-ion battery, can be replaced with the already available AC source, which powers the rest of the robot, using an appropriate AC to DC converter.

APPENDIX A.

SUPPLEMENTARY MATERIALS FOR PAPER III

INTERACTION DYNAMICS OF THE COMBINED HUMAN ARM-ROBOT MANIPULATOR SYSTEM

The interaction dynamics of a human arm is assumed to behave like a mass-spring-damper system, which involves passive, linear and time-invariant second-order dynamics. Figure A.1 shows a schematic representation of combined interaction dynamics of the robotic manipulator and the human arm right before the onset of perturbation (Figure A.1A), and during the perturbation (Figure A.1B).

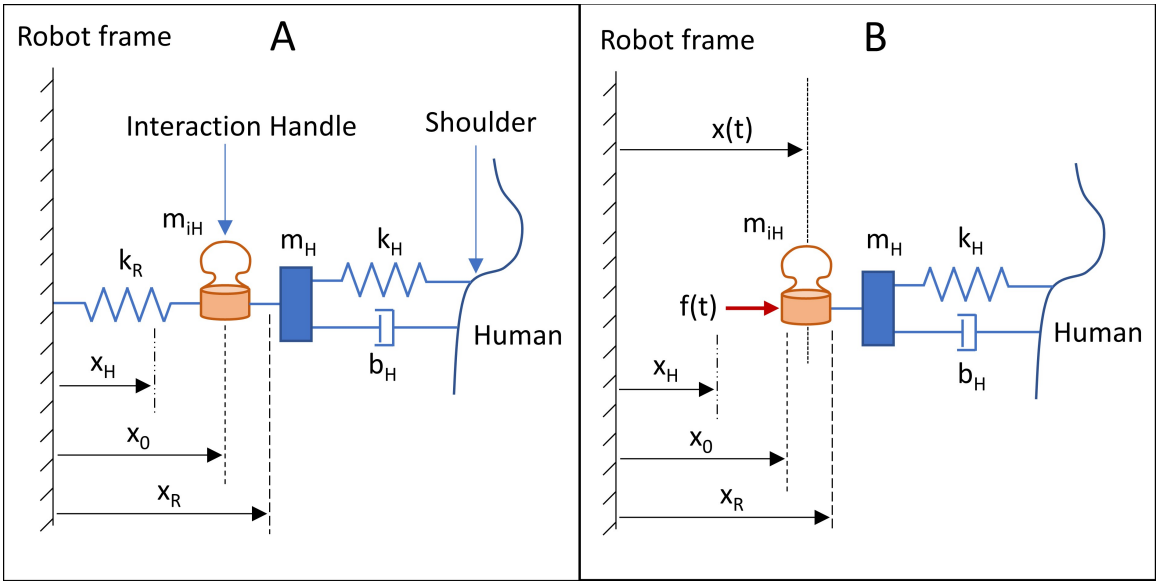

Figure A.1. The schematic representation of the interaction dynamics of the robot-human arm system during the experiment. Human arm model is characterized by mass (m_H), stiffness (k_H), and viscosity(b_H). The equilibrium point of the human arm is assumed to be at x_H. m_{iH} be the mass of the interaction handle. (A) At the instant right before the onset of the perturbation, stiffness controller with k_R stiffness is active whose equilibrium point is set at x_R. The interaction handle is at x_0 at this instant. (B) During the perturbation, the stiffness controller is replaced by interaction force controller (target force = f_{target}). The position of interaction handle at any instant during perturbation is represented by $x(t)$. The interaction force measured at that instant be $f(t)$. All the positions are represented with respect to the robot frame in this discussion.

The arm dynamics right before the onset of the perturbation can be represented as

$$f_{H0} = (m_H + m_{iH})\,\ddot{x}_0 + b_H\,\dot{x}_0 + k_H\,(x_0 - x_H) \tag{A.1}$$

where f_{H0} is the elastic restoring force of the arm right before the onset of perturbation. $\ddot{x}_0$ and $\dot{x}_0$ are the velocity and acceleration of the interaction handle at that instant, respectively.

The robotic manipulator is stiffness controlled with respect to the displacement from the workspace center (x_R). Hence, the force maintained by the stiffness controller right before the onset of perturbation is,

$$f_{R0} = k_R \, (x_0 - x_R) \tag{A.2}$$

At any instant before the perturbation onset, the force measured by force/torque sensor is equal to the elastic restoring force from the arm and the force maintained by the stiffness controller. Hence, force measured right before the onset of perturbation is

$$f_0 = f_{R0} = f_{H0}. \tag{A.3}$$

Substituting Equation A.1 in Equation A.3, we get

$$f_0 = (m_H + m_{iH}) \, \ddot{x}_0 + b_H \, \dot{x}_0 + k_H \, (x_0 - x_H) \tag{A.4}$$

The stiffness controller is deactivated when the force perturbation f_{target} is applied. The interaction dynamics after the perturbation is,

$$f(t) = (m_H + m_{iH}) \, \ddot{x}(t) + b_H \, \dot{x}(t) + k_H \, (x(t) - x_H) \tag{A.5}$$

Subtracting Equation A.4 from Equation A.5, we get

$$f(t) - f_0 = (m_H + m_{iH}) \, (\ddot{x}(t) - \ddot{x}_0) + b_H \, (\dot{x}(t) - \dot{x}_0) + k_H \, (x(t) - x_0) \tag{A.6}$$

For our experiment, all the variables except the system parameters ($m_H + m_{iH}$, b_H, and k_H) are known. Hence, the system parameters can be estimated using linear regression.

APPENDIX B.

USER MANUAL

This section describes the feature of Ophrie and contains information about mechatronics, software, and operating the robot.

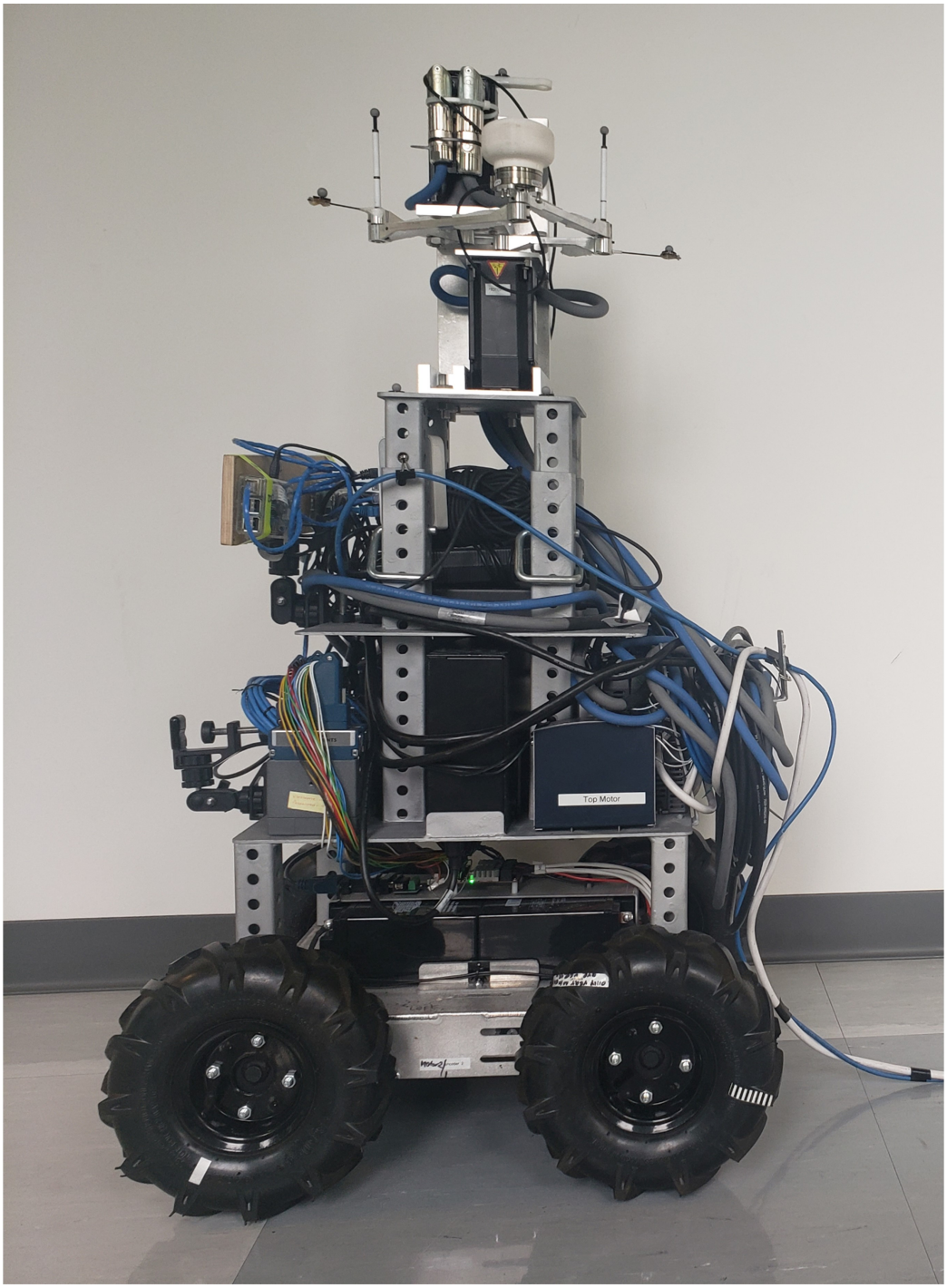

Figure B.1. Ophrie

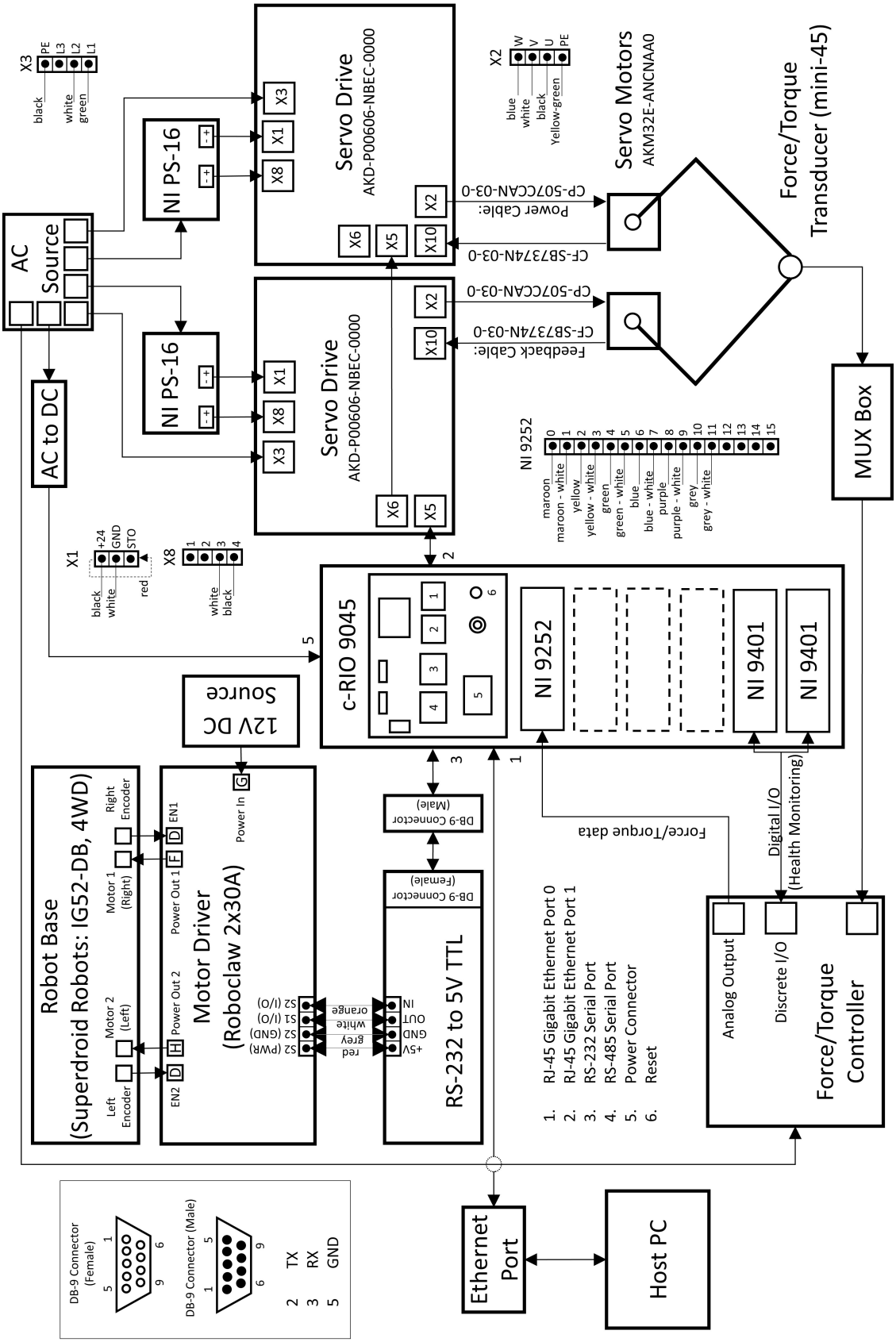

Figure B.2. Flowchart displaying a complete mechatronics system of Ophrie.

1. MECHATRONICS FRAMEWORK

1.1. CONNECTING OPHRIE TO HOST COMPUTER

You must connect Ophrie to the host computer using the Ethernet Cable. The host computer is the one where you will have a full functioning LabVIEW program ready to be deployed to Ophrie. Make sure that Ophrie is connected to an Ethernet port that shares the same subnet mask as that of your host computer. The blue cat5e cable can be seen in Figure B.1, which is wrapped around the white power cable on the right-hand side of Figure B.1.

1.2. CONNECTING THE SUB-SYSTEMS

Five mechatronics sub-systems – a NI c-RIO 9045, a force/torque transducer (mini45), two servo motors, and a four-wheel differential drive (IG52-DB 4WD, Superdroid Roobts) robot – constitute Ophrie, wired together with the necessary accessories. A detailed mechatronic framework of Ophrie is shown in Figure B.2. The flowchart shows some cable color code conventions that are currently being used in Ophrie. The convention can be changed if needed.

Each servo motor (AKM32E-ANCNAAA0) is designed to be controlled using a servo drive (AKD-P00606-NBEC-0000). A power cable (CP-507CCAN-03-0) supplies power to the motors and a feedback cable (CFSB7374N-03-0) feeds the encoder reading back to the respective servo drive. The servo drives require a separate AC input and two extra 24V DC inputs for their operation (NI PS-16).

The master real-time controller (c-RIO) is connected to the two servo drive slaves in a daisy chain fashion (Ethernet port 1 of c-RIO to X5 port of the servo drive 1, and X6 port of the servo drive 1 to X5 port of the servo drive 2) and are controlled using the EtherCAT Protocol. The controller also receives the analog voltages from the force/torque control (ATI Industrial Automation Inc.) using NI 9252 analog voltage input module. The six

different voltages correspond to forces and torques measured by the force/torque transducer (mini45, ATI Industrial Automation, Inc.) which is mounted at the end-effector. The mux board electronics connect directly to the transducer's sensing elements and provide high level output signals (F_x, F_y, F_z, T_x, T_y, and T_z). In addition, the controller accepts discrete signals from F/T controller using digital I/O module (NI 9401), here used for monitoring the health of the transducer.

The c-RIO controller also serves as the motor controller for the wheels. The mobile robot, on top of which the entire body and the interactive arm of Ophrie rests, was purchased from Superdroid Robots. It consists of two motors (of the wheels) powered by the Roboclaw 2x30A motor driver. Two 24V lithium-ion batteries power the motor driver. The motor encoders, which are powered by the motor driver (+5V), feedback the quadrature pulses to the motor driver. The c-RIO controller communicates with the motor driver through serial communication. We have used the RS-232 serial port for this purpose and have used 'RS-232, S8 Serial Cable, 10-Position Modular Plug to 9-Pin DSUB' cable from NI. The operating voltage of the c-RIO RS-232 is higher than that of the motor driver. Hence, we have used RS-232 to 5V TTL converter, which was purchased from Jeddy Ventures LLC - SerialComm.

1.3. POWERING THE SUB-SYSTEMS

The robot needs to be powered using an external AC source. The base part is powered by two 12V rechargeable lithium-ion batteries. Ensure that the batteries are adequately charged before operating the robot. A power extension has been used to provide power to six different sub-systems, namely the c-RIO controller, two power supplies, two AKD servo drives, and a force/torque controller, as shown in Figure B.2. A proper inspection is required to ensure that all the circuits are complete. The safe working voltage for the c-RIO controller is +24V, and hence, an AC to DC converter is required.

2. SOFTWARE FRAMEWORK

LabVIEW programming language is used to program the commands required to operate Ophrie. Two additional modules (LabVIEW SoftMotion module 2018 and LabVIEW Real-Time module 2018) are required to deploy the commands from the remote computer (Host) to the central controller. The designated computer and the central controller should be connected to Ethernet and maintain the same subnet mask. *NI stopped releasing a new version of the LabVIEW SoftMotion module after LabVIEW SoftMotion module 2018. Hence, it is advised not to update the LabVIEW program or any accessories to a higher version for the smooth operation of Ophrie.*

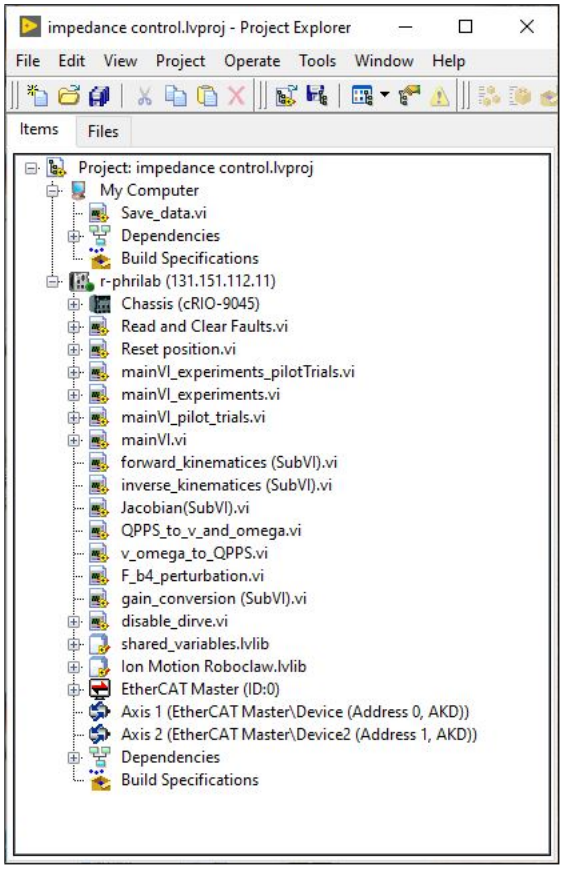

Figure B.3. LabVIEW project main tab

2.1. LABVIEW PROJECT: IMPEDANCE CONTROL.LVPROJ

All the LabVIEW programs, in host and remote c-RIO controller, are controlled by a single LabVIEW project, 'impedance control.lvproj' in this case. Figure. B.3 shows the main tab of the LabVIEW project programmed for Ophrie. The folder 'My Computer' contains all the programs that run on the host computer, and the folder 'r-phrilab(131.151.112.3)' contains the programs that runs on the central controller.

2.1.1. My Computer. In this project, the 'My Computer' folder only contain a program that receives and records the data passed from the remote controller. Figure B.4 shows the program 'save_data.vi'. Make sure to run this after all the programs on the remote computer are completed.

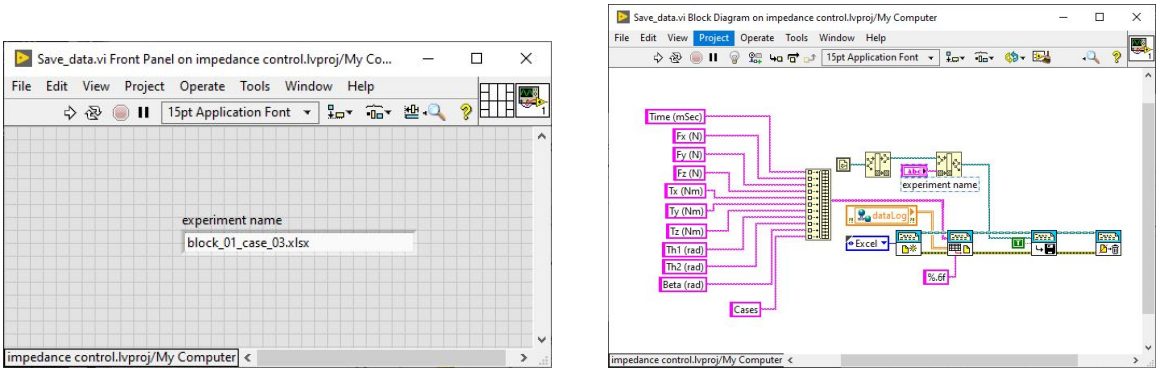

(a) (b)

Figure B.4. Save_data.vi **(a)** Front panel **(b)** Block diagram

2.1.2. r-phrilab(131.151.112.3). r-phrilab(131.151.112.3) in Figure B.3 represents the real-time controller of Ophrie. It is registered as 'r-phrilab' in the university network with an IP address of 131.151.112.3. It contains all the LabVIEW VIs, sub-VIs, libraries, and the external modules attached, such as c-RIO chassis, EtherCAT master and the slave axes. Axis 1 represents the servo motor 1 and axis 2 represents the servo motor 2. Both of these axes are controlled through two servo drives as described earlier.

The VIs whose names start with mainVI are the main programs and call different other VIs when they are functioning. Four such VIs can be seen in Figure B.3. These are very similar but might have been modified to serve different experiments and trial types. During a specific experiment design, one mainVI is self-sufficient, and there is no need to switch to a different one. The Figures B.5 and B.6 show the front panel and block diagram of 'mainVI_experiments.vi'.

The front panel of the 'mainVI____.vi' VI lets the user input the magnitude of background stiffness (75N/m in both x and y direction is used in Figure B.5a). Likewise, the user can choose the trial number ('Case') that will be conducted (default = 0). The graph to view instantaneous forces in real-time is available, as shown in the top left of Figure B.5. After the VI stops, a time series plots of the forces is generated in the bottom two plots of Figure B.5. The iteration time of the interactive arm and the base control are plotted separately as well. Ophrie starts moving only after latching 'Engage Manipulator' and 'Start Experiment' in sequence. It stops after the trial is completed or the 'disable axis & stop robot' switch is pressed.

The block diagram of the 'mainVI____.vi' VI is shown in Figures B.5a, and B.6. The program uses several subVIs, which are listed below.

- v_omega_to_QPPS: converts the asked linear and angular velocity command to required quadrature pulses for left and right wheels (Figure B.7).
- QPPS_to_v_and_omega: converts the measured right and left wheel speeds into linear and angular velocity of Ophrie (Figure B.8).
- forward_kinematics(SubVI).vi: accepts the instantaneous angular position of the two servo motors driving the interactive arm, and computes the Jacobian matrix (Figure B.9).

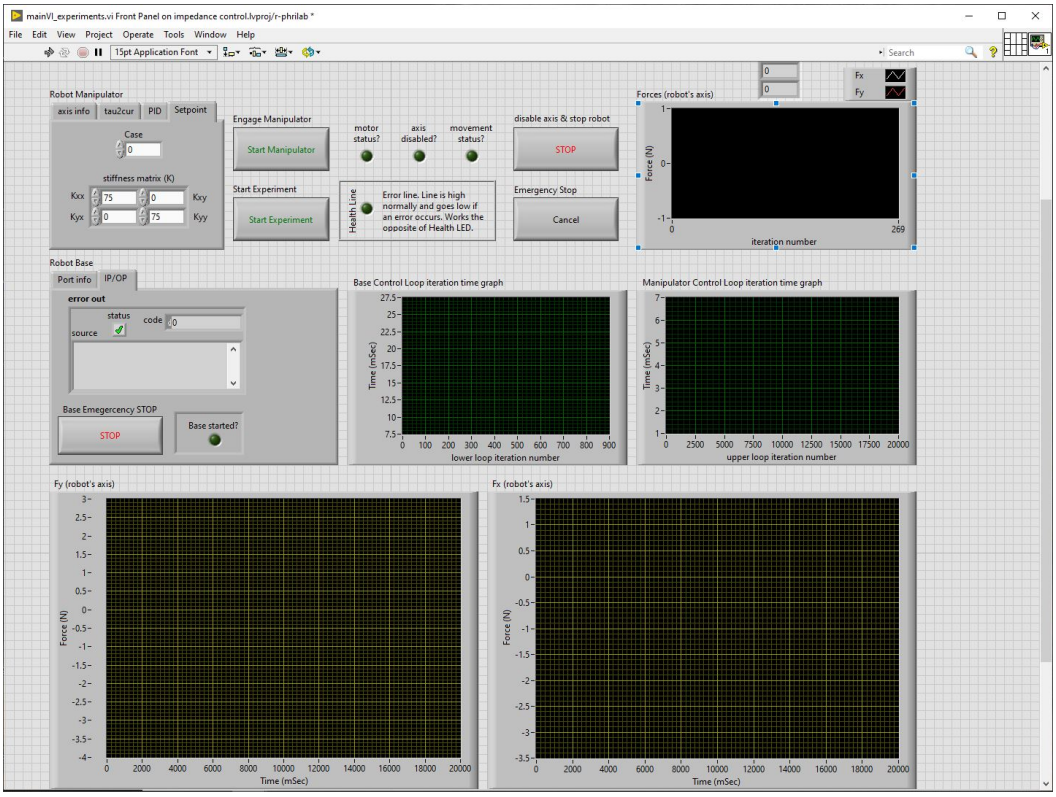

(a)

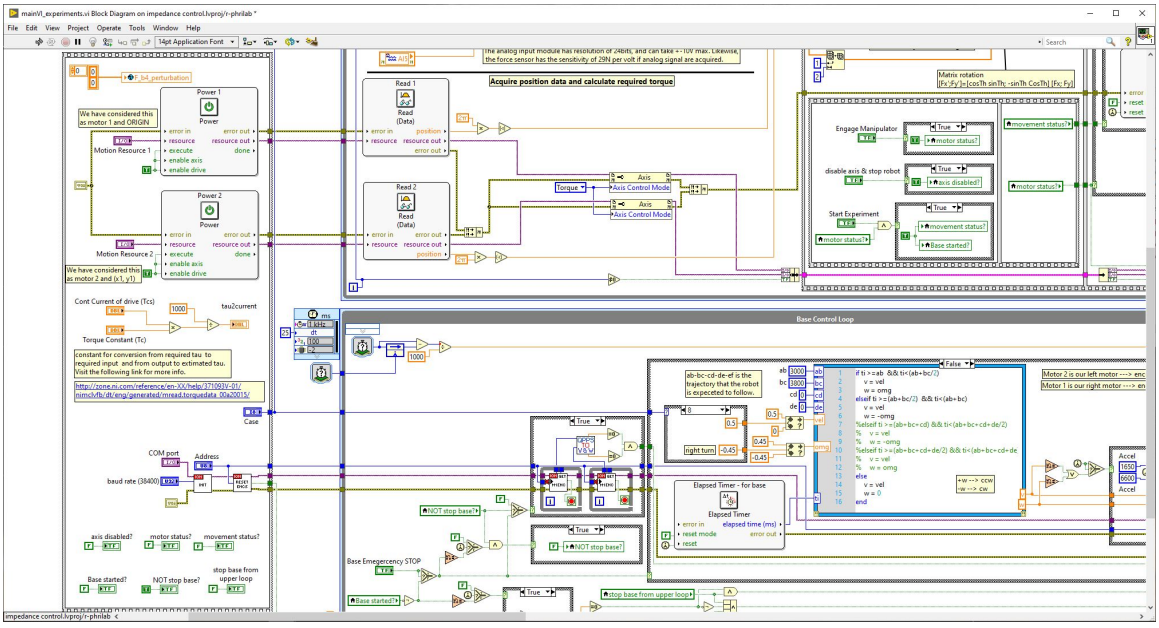

(b)

Figure B.5. mainVI_experiments.vi (part 1) **(a)** Front panel **(b)** Block diagram part 1 (left). Note: see also Figure B.6.

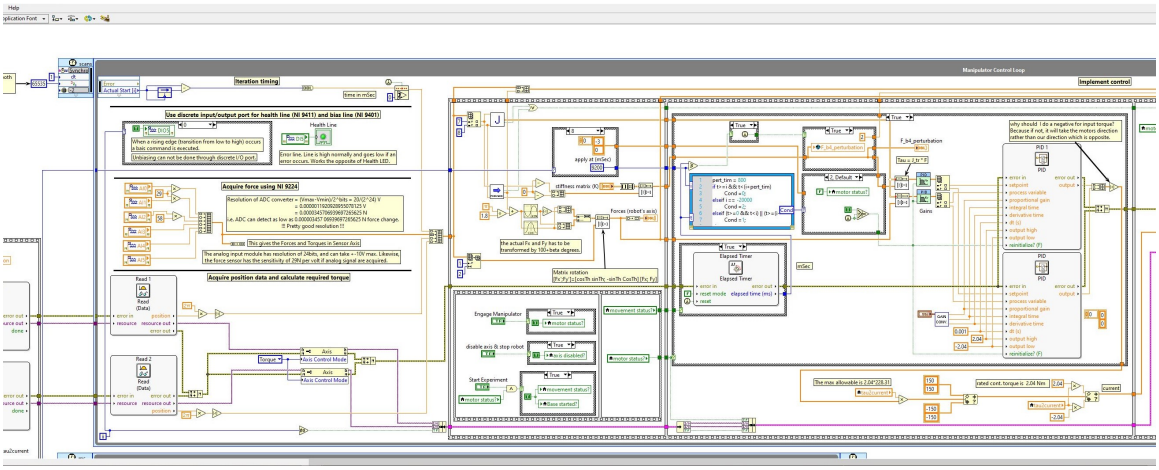

(a)

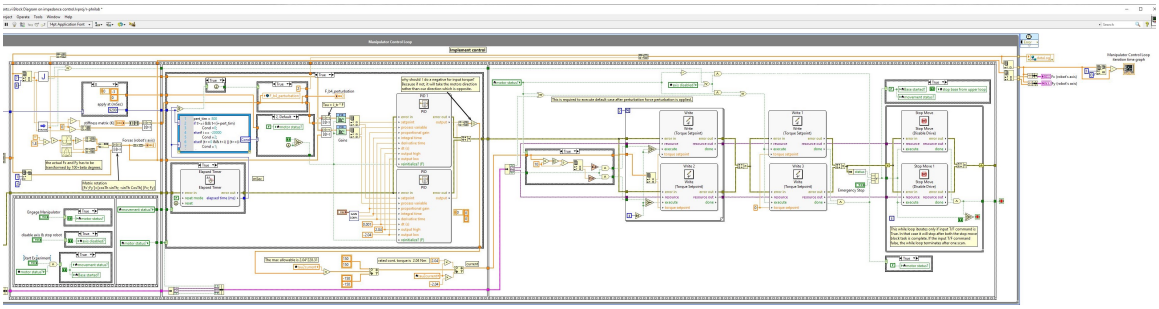

(b)

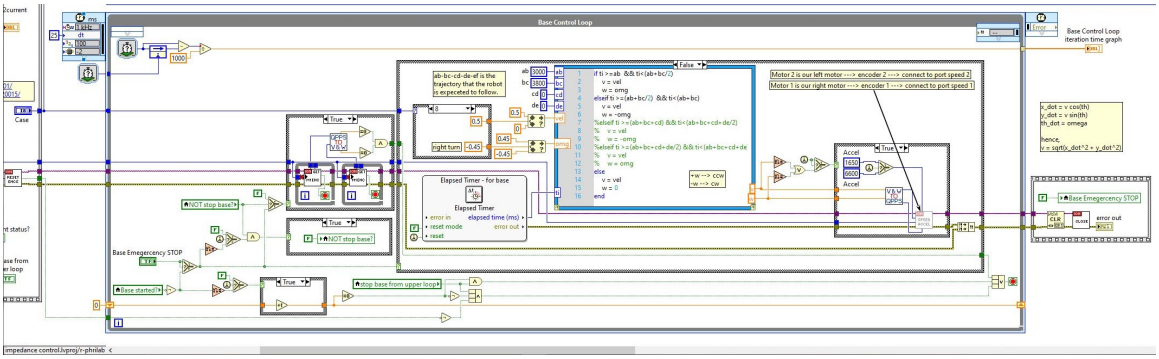

(c)

Figure B.6. mainVI_experiments.vi (part 2) **(a)** Block diagram part 2 (upper row- middle), **(b)** Block diagram part 3 (upper row –right), **c)** Block diagram part 4 (lower row) – robot control. Note: see also Figure B.5.

- Jacobian(SubVI).vi: accepts the instantaneous angular position of the two servo motors driving the interactive arm and computes the end-effector position using forward kinematics (Figure B.10).

- gain_conversion(SubVI): converts the PID gains (K_p, K_i, and K_d) to parameters that PID function block accepts, which are K_c, T_i, and T_d (Figure B.11).
- initilize.vi**: initializes the motor driver for the robot base.
- ResetEncoders.vi**: resets the wheel encoders.
- ReadSpeedM1.vi**: read speed of the right front wheel
- ReadSpeedM2.vi**: read speed of the left front wheel
- SpeedAccelerationM1M2.vi**: command the motor driver to run at the specified speed and acceleration.
- close.vi**: clears the current task.

**These subVIs are placed in the library named 'Ion Motion Roboxlaw.lvlib' (see Figure B.3). These are used to command Roboclaw 2x30A to do required tasks, and were provided by Basic Micromotions Inc.

For calibration of servo motor positions before operating Ophrie, 'Reset position.vi' has to be run. Proper instruction has to be followed. If procedures are correctly followed, this VI sets the servo motor positions to zero when the proximal links are aligned perpendicular to the robot frame towards the robot handle. The block diagram and the front panel for this VI can be seen in Figure B.12.

The VI 'Read and Clear Faults' lets user view the error message if there are any. It clears the errors as well. Make sure to understand the cause of the error. Clearing the errors without understanding why they occurred in the first place may lead to accidents. The block diagram and the front panel for this VI can be seen in Figure B.13.

The 'F_b4_perturbation.vi' VI (in Figure B.3) is a global variable and is used to record the force vector right before the perturbation onset.

The 'disable_drive.vi' VI (in Figure B.3) can be used to disable the AKD drives and stop the move if in case the servo motors have to be force stopped (see Figure B.14).

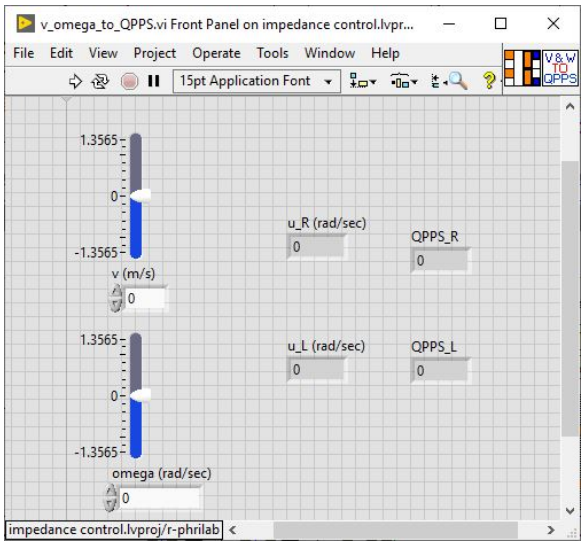

(a)

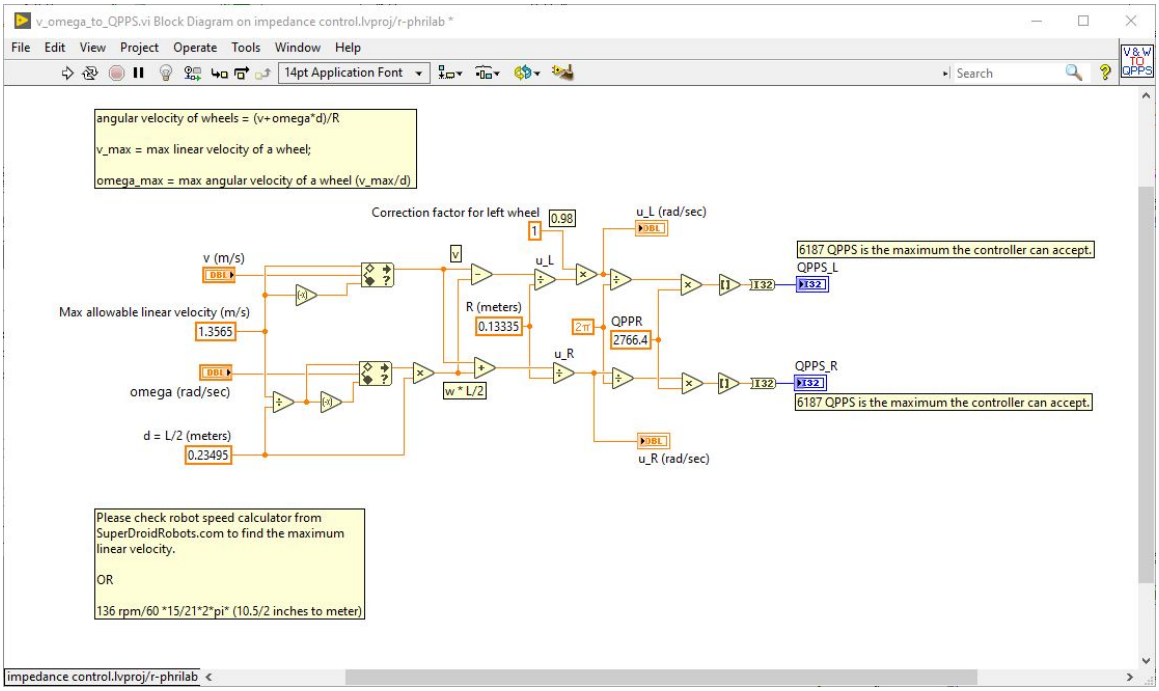

(b)

Figure B.7. v_and_omega_to_QPPS.vi **(a)** Front panel **(b)** Block diagram

The library named ‘shared_variables.lvlib’ has one shared variable block used to record and transfer the variables that have to be stored for future analysis. The sender node of this variable can be seen on the top-right position of Figure B.6b. The receiver node

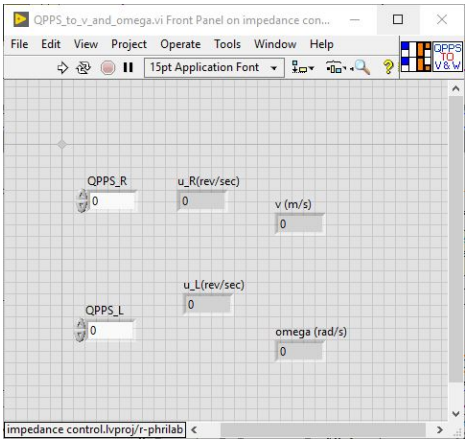

(a)

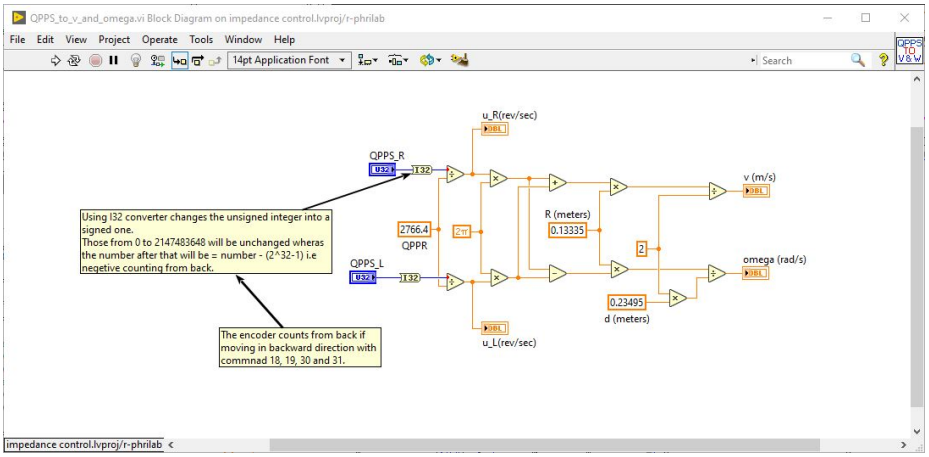

(b)

Figure B.8. QPPS_to_v_and_omega.vi **(a)** Front panel **(b)** Block diagram

of this variable can be seen in Figure B.4. After the data is loaded (inside c-RIO) in this variable, it stores it and spits out (in the host computer) whenever asked – that is, whenever 'save_data.vi' is called.

Some of the features used in the VIs discussed in these sections are available only with LabVIEW Softmotion module 2018 and LabVIEW Real-Time module 2018.

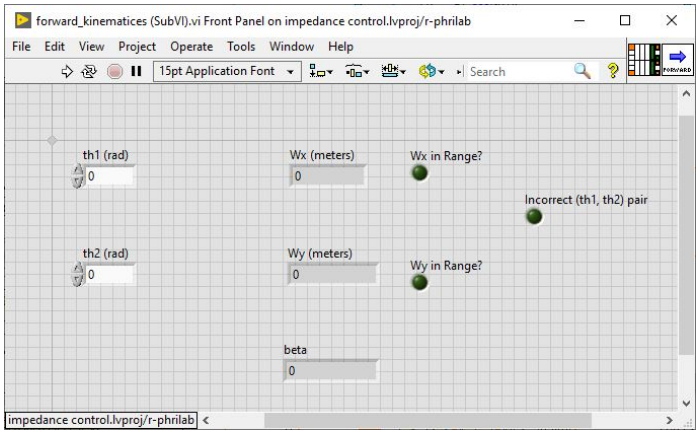

(a)

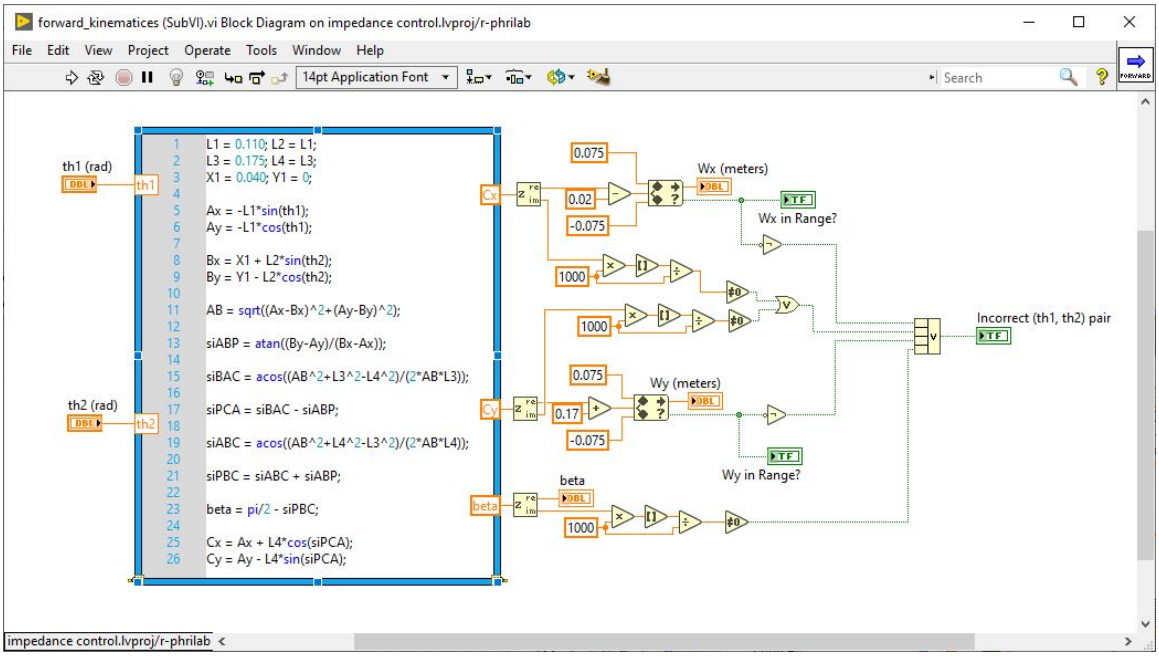

(b)

Figure B.9. forward_kinematics(SubVI).vi **(a)** Front panel **(b)** Block diagram

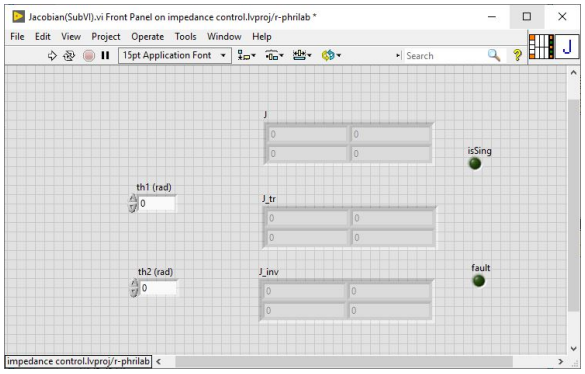

(a)

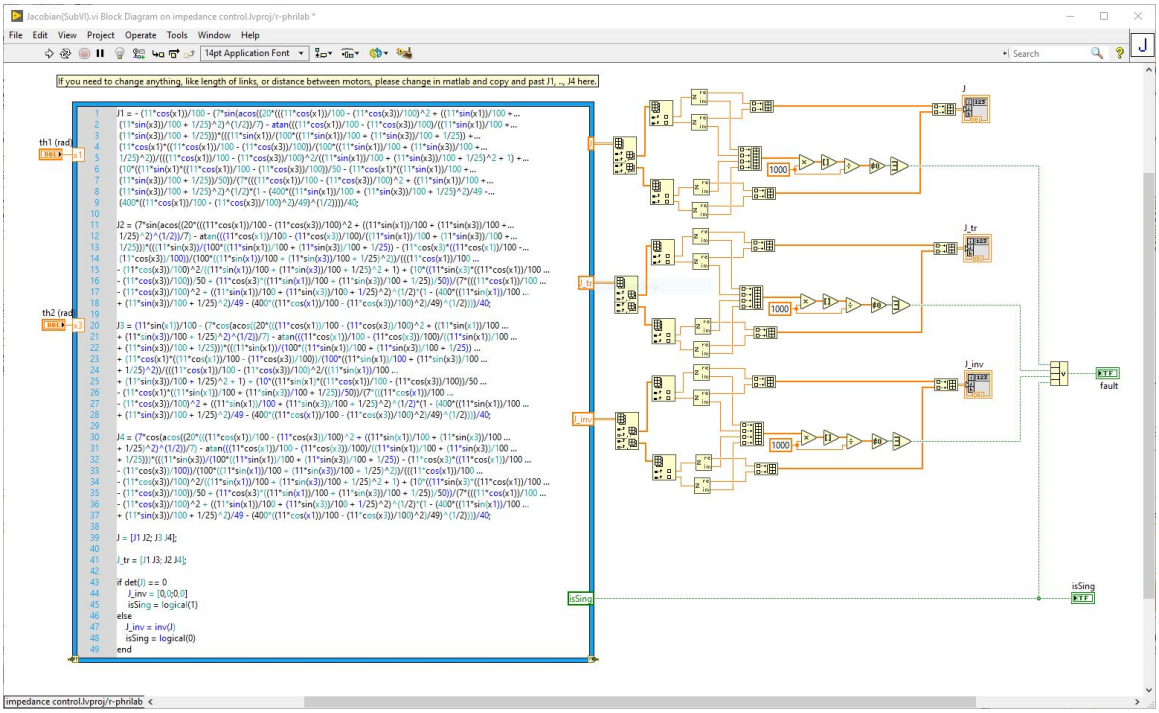

(b)

Figure B.10. Jacobian(SubVI).vi **(a)** Front panel **(b)** Block diagram

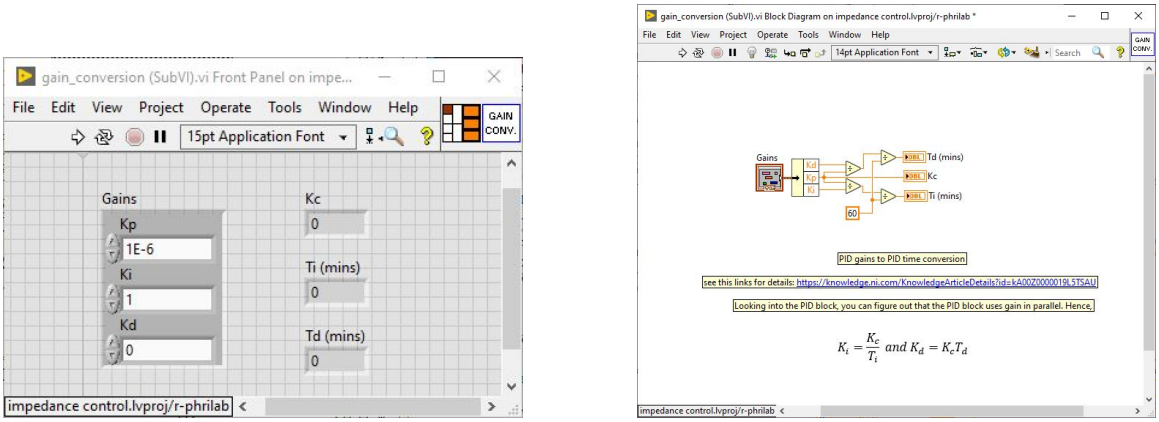

(a) (b)

Figure B.11. gain_conversion (SubVI).vi **(a)** Front panel **(b)** Block diagram

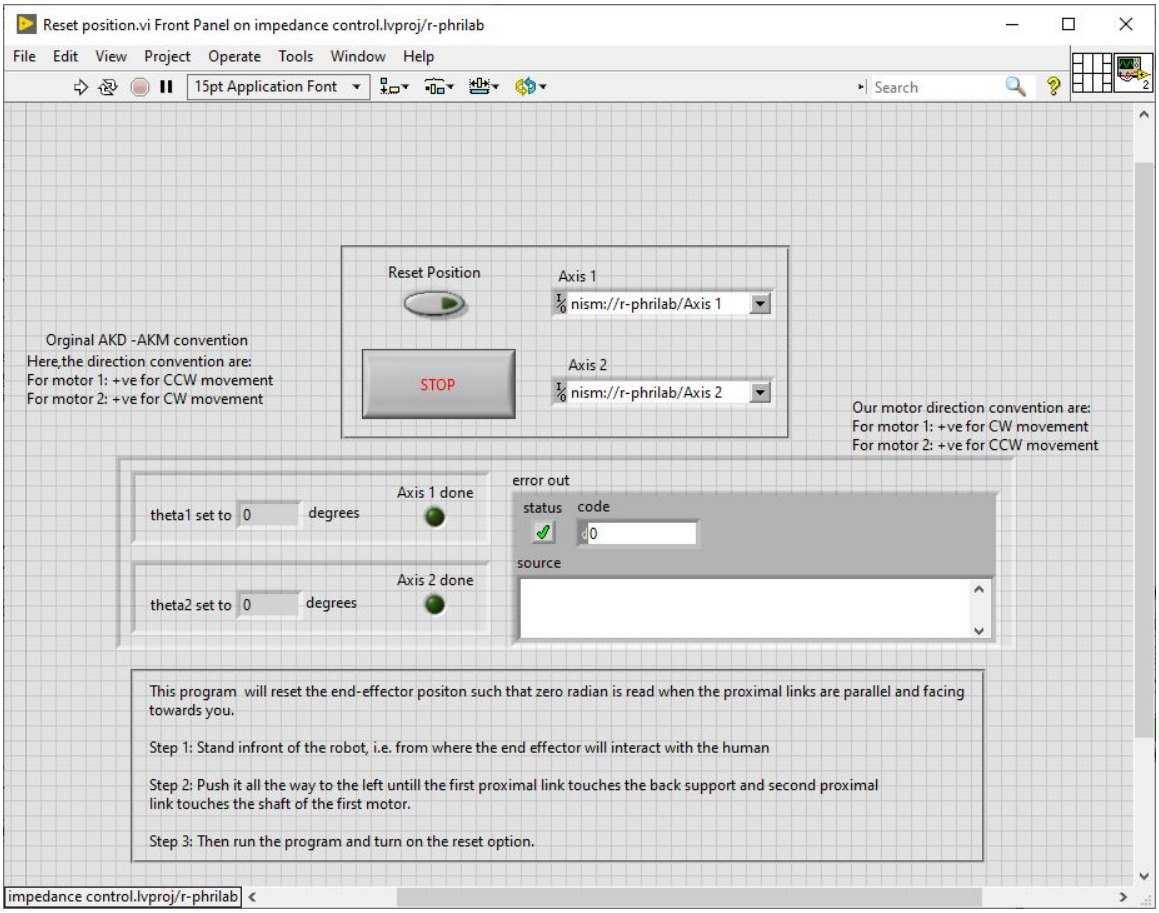

(a)

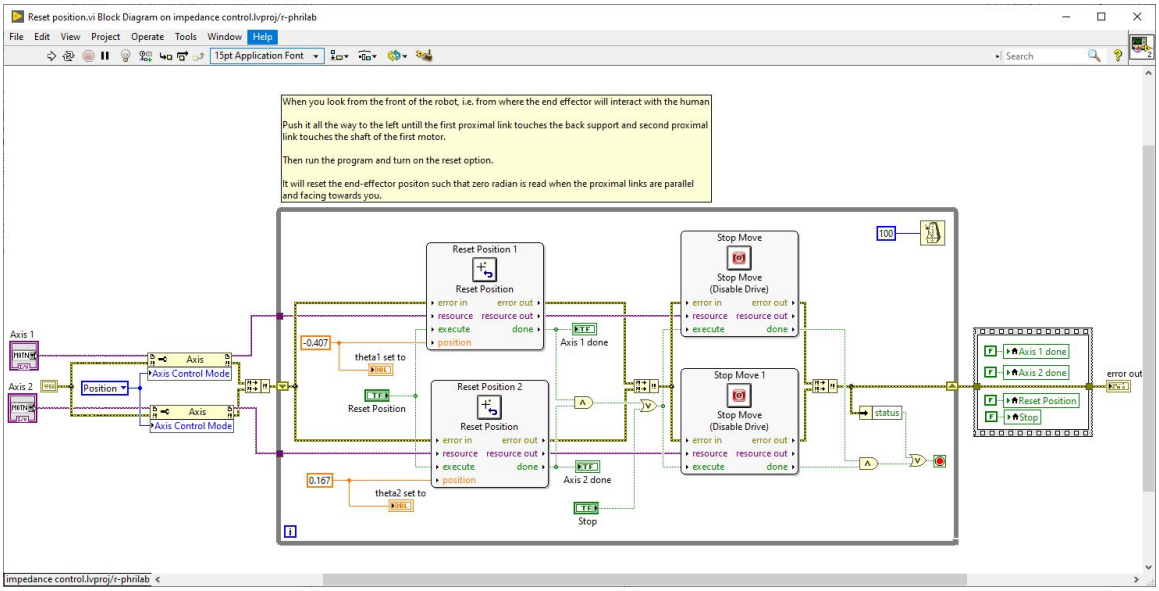

(b)

Figure B.12. Reset position.vi **(a)** Front panel **(b)** Block diagram

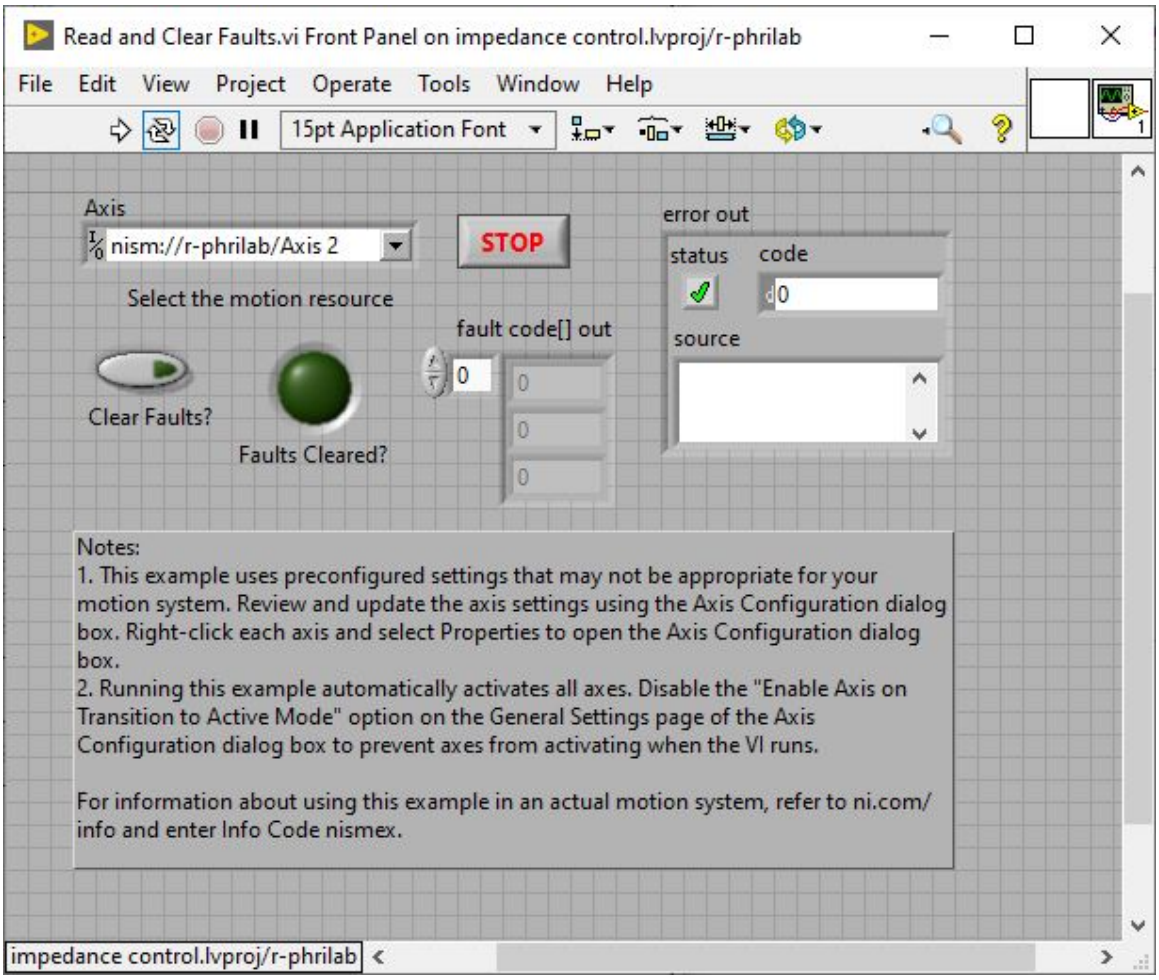

(a)

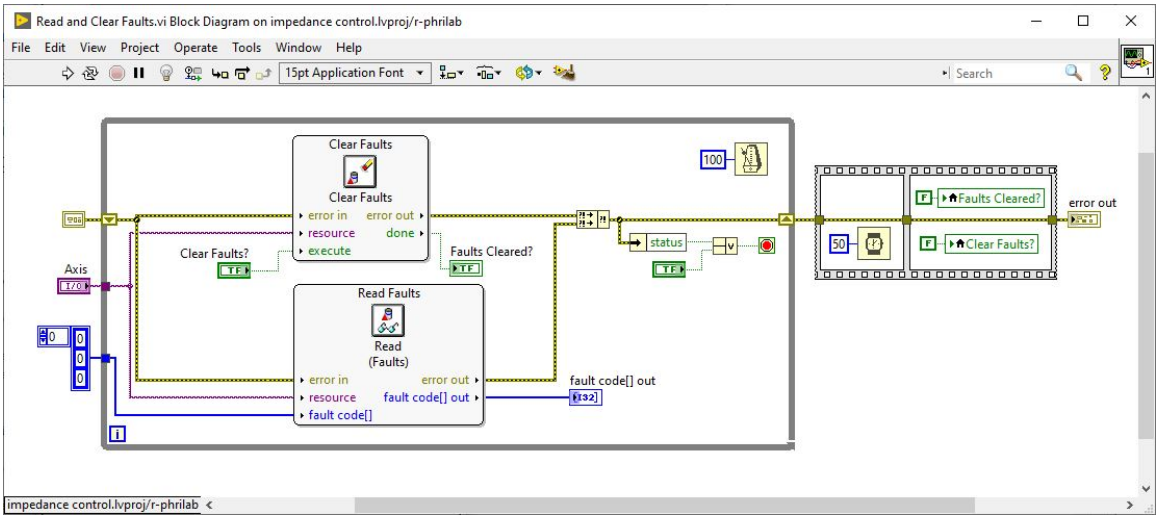

(b)

Figure B.13. Read and Clear Faults.vi **(a)** Front panel **(b)** Block diagram

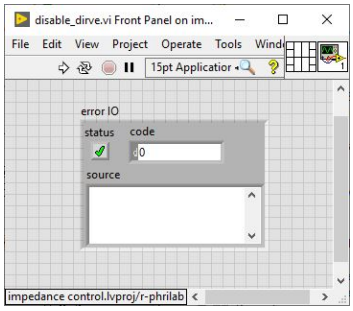

(a)

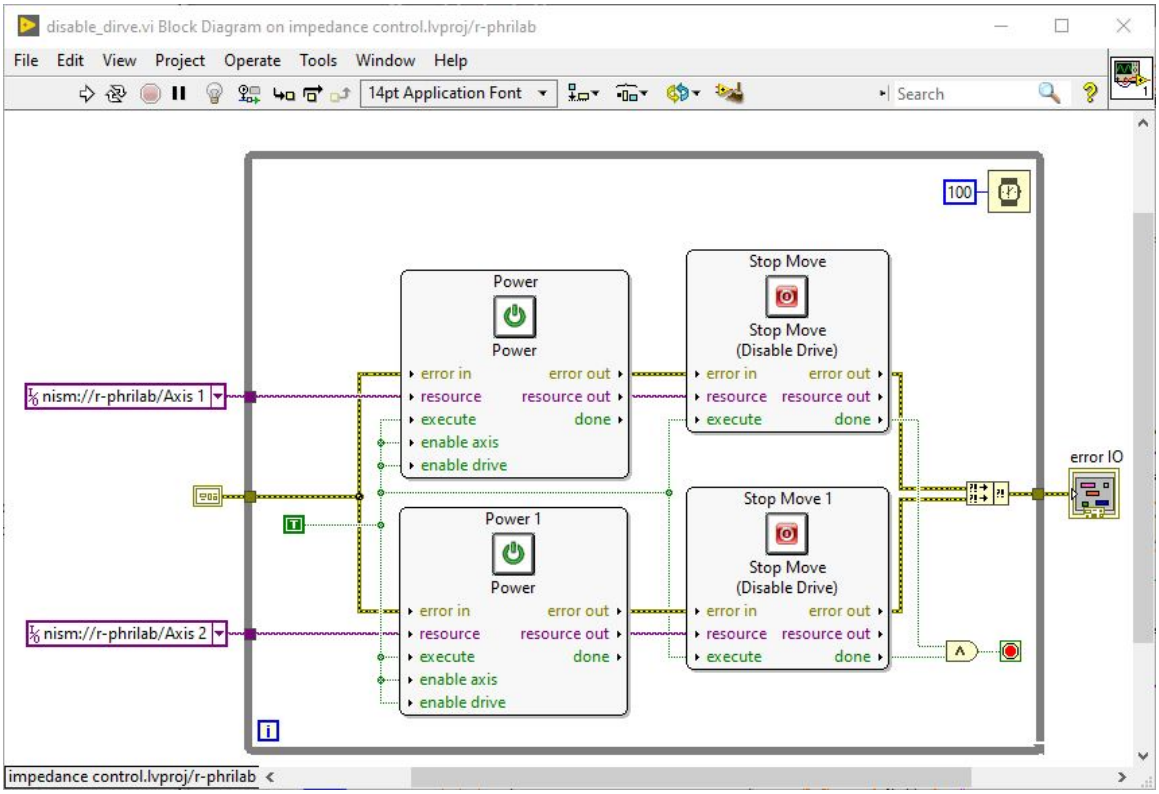

(b)

Figure B.14. disable_drive.vi **(a)** Front panel **(b)** Block diagram

3. OPERATING OPHRIE

This section provides the step-by-step procedure for operating Ophrie.

1. Ensure all the circuits are complete as shown in Figure B.2. Plug Ophrie's power cable into the AC source. Connect c-RIO to Ethernet. Ensure that the host computer shares the same subnet mask with Ophrie. Turn on the power to the base robot. Ensure all other mechatronics sub-systems are not turned off.

2. Configure cRIO (if not done already). You can use Ni Max for doing so. *Do not update LabVIEW or its modules to versions higher than 2018.* This step is only required if cRIO is being connected for the first time. The present Ophrie design is already configured, and no extra input is needed.

3. Configure and calibrate F/T controller (if not done already). For more information on performing calibration, check for the company user manual. This step is only required during the initial installation of either the F/T controller, transducer, or both. For the present Ophrie design, it is already configured and calibrated. Hence this step can be skipped.

4. Create a LabVIEW project. Right-click on the project and add 'Target and devices.' Select and add the desired device. If you are using 'impedance_control.lvproj', Real-Time CompactRIO (r-phrilab) is already added. Hence, this step can be skipped.

5. Right-click on the device named r-phrilab(131.151.112.3) and connect to the remote device. You won't be able to connect to the device if your device's IP address is input wrong. You can check your device's IP address through NI MAX. If the IP address is wrong on your project, go to the properties tab by right-clicking on the device, and you should be able to change the IP address in the 'general' tab.

6. Right click and go to properties. Set the required scan engine properties. Currently, it is set to scan period of 1ms, network publishing period of 500ms, and the scan engine priority is set to ‘above time critical.’

7. You should already see the c-RIO chassis in the list of targets and devices available to the added device.

8. Add ‘EtherCAT Master’ to your devices. To do that, right-click on your device and navigate through ‘New’ and ‘Target and devices.’ You should find ‘EtherCAT Master Device’ there. The installed software and modules can be navigated using NI MAx. In NI MAX, select your device and go to software. You should be able to spot all the software, including ‘NI-industrial Communication for EtherCAT 18.0’, which is required to work with EtherCAT protocol.

9. Add ’SoftMotion Axis.’ To do that, right-click on your device and navigate through ‘New’ and ‘SoftMotion Axis,’ and add two axes.

10. Configure the ‘Softmotion Axis’ accordingly. If you are using ‘impedance control.lvproj’ project, it is already configured. Hence, this step can be skipped.

11. After you add ‘SoftMotion Axis’, two scan engine modes will be available. Right-click on the device, go to ‘Utilities,’ navigate to ‘Scan Engine Mode’ and choose either of those two modes, as required. If LabVIEW throws the error “An error occurred while attempting to switch the I/O scan mode. NI SoftMotion: Parameter specified exceeds the valid data range. Refer to .... ranges”, the step 6 is not configured properly.

12. If you are creating a new project, right-click on your device and navigate through ‘New,’ and then ‘VI.’ If you are using ‘impedance control.lvproj’, proceed to step 13.

The steps after this will assume that the user will be using ‘impedance control.lvproj’ project.

13. Open "Read and Clear Faults.vi". Chose axis 1. Run the VI. Press ‘Clear Faults’. If there are no errors, press stop. If you get any errors in the error message, go back and change the ‘Scan engine mode’ (follow step 11).

14. If step 13 is successfully completed without any error message or the error pop-up tab, skip this step. If you get an error saying, “An error occurred while attempting to switch the I/O scan mode: LabVIEW: (Hex 0x 80DF000A) A communication error between the host and target occurred” or if NI-cRIO device disconnects, connect to the c-RIO device again and restart c-RIO. Then, repeat 13.

15. Repeat step 13 and step 14 for axis 2 using the same VI as in step 13.

Calibration of interactive arm position: Step 16 to step 19.

16. Move the manipulator Clockwise until the proximal link of Motor 1 touches the back frame. Press gently towards the Clockwise direction so that the link maintains continuous contact with the frame. At the same time, the proximal link from the motor 2 should be pressed against the motor 1 axis.

17. (a) Open "Reset Postion.vi"; (b) run the VI; (c) press reset position switch; (d) wait until program stops; (e) if no errors, close the VI and proceed to step 20.

18. If there is an error, check whether the NI scan engine is in ‘active status’ or not. If not, change it to ‘active status.’ If it is already ‘active,’ change to configuration status and revert to ‘active status.’

19. Repeat step 17 after step 18. (Note, you do not have to do step 18 and step 19 if the VI does not throw any error after step 17.)

Staring Ophrie: using mainVI____.vi

20. Open either of the four VIs (‘MainVI____.vi’) shown in Figure B.3.

21. Set the required background stiffness value and choose the trial number you want to run. Then run the VI.

22. Make sure that someone is holding the interaction handle. FAILING TO FOLLOW THIS MAY CAUSE DAMAGE TO THE INTERACTIVE ARM.

23. Engage manipulator by pressing 'Start Manipulator.' This will activate the position-based background stiffness controller.

24. Whenever ready, press 'Start Experiment' to trigger the robot base movement.

25. The entire system can be shut down by pressing 'Stop: disable axis & stop robot' at any time. To stop the robot base, the switch on the back of the robot base frame has to be turned off.

26. With the current control design, Ophrie is programmed to follow either of the 3 trajectories mentioned in Paper IV, provide 0.8ms of perturbation, and automatically stop after the trial ends. This sequence (or experiment design) can be changed through some algorithm changes inside the math script shown in Figure B.6a. A couple of changes have to be done in the robot base algorithm accordingly (that is, in Figure B.6c).

Table B.1. More information on the parts and software (and modules) used in Ophrie's current version can be found using the link provided in this table.

Parts and software (and modules)	**External link to the product page**
NI c-RIO 9045	https://www.ni.com/en-us/support/model.crio-9045.html
NI 9252 module	https://www.ni.com/en-us/support/model.ni-9252.html
NI 9401 module	https://www.ni.com/en-us/support/model.ni-9401.html
NI PS-16	https://www.ni.com/en-us/support/model.ps-16.html
'10-Position Modular Plug to 9-Pin DSUB' cable, NI	https://www.ni.com/en-us/support/documentation/product-certifications/model.rj50-db9-serial-cable.html
LabVIEW 2018	https://www.ni.com/
LabVIEW 2018 SoftMotion Module	https://www.ni.com/
LabVIEW 2018 Real-Time Module	https://www.ni.com/
Servo Motor (AKM32E-ANCNAAA0)	https://www.kollmorgen.com/en-us/service-and-support/technical/product-selectors/?shareResults=zzAKM32E&productType=Servo-Motor
AKD Drive (AKD-P00606-NBEC-0000)	https://www.kollmorgen.com/en-us/products/drives/servo/akd/
ATI F/T sensor: mini45	https://www.ati-ia.com/products/ft/ft_models.aspx?id=mini45
ATI F/T controller	https://www.ati-ia.com/app_content/documents/9620-05-CTL.pdf
Motor driver (Roboclaw 2x30A)	https://www.basicmicro.com/RoboClaw-2x30A-Motor-Controller_p_9.html
Robot base (Superdroid Robots: IG52-DB, 4WD)	https://www.superdroidrobots.com/robots/robotic-kits-platforms/wheeled-robots/product=1648
RS-232 to 5V TTL	https://www.serialcomm.com/datasheets/TTL-232-5IE.pdf

4. PRE-PROCESSING ARM MOVEMENT DATA

In our lab, it is possible to record the human biomechanics movement data with the help of the Vicon vantage cameras mounted all around the lab. Vicon Nexus software and ProCal are required to record and pre-process the data. More information about the cameras and required software and instructions on how to operate the system can be found at `https://www.vicon.com/hardware/cameras/`.

This section will briefly discuss what data was recorded and how it can be pre-processed to extract biomechanics movement information during the experiments that were reported in Paper III and Paper IV.

In both the papers, robot position and its links' positions were recorded with the help of 10 markers arranged in the same way as the template as shown in Figure B.15. The markers' positions can also be seen in Figure B.1, and more clearly on the figure included in Paper III. The markers defined 3 rigid parts of Ophrie. When viewed from the back of Ophrie towards the interactive handle, markers RA, RT, and RL represent the right proximal link (green). Likewise, markers LA, LT, and LL represent the left proximal link (red), and RBB, LBB, RFB, and LFB represent the robot's frame (blue). From the time-series data collected, we can extract the angular position of the robot links and the location of Ophrie with respect to lab origin. The naming convention for the markers can be found in Table B.2.

In the experiment reported in Paper III, we used the standard template 'PlugIn Gait FullBody ai' provided by Vicon Nexus. There are 39 markers required for this template, which requires a significant amount of time for the subject preparation. We used a custom template for the human right arm and the shoulder in the experiment reported in Paper IV. The marker positions can be seen Figure B.16. Markers LSHO, C7, and CLV represent the shoulder, RSHO, UPA and ELB represent the upper arm, FRMBB, FRMBA, and FRMF represent the forearm, and WRA, WRB, and FIN represent the hand. The naming convention for the markers can be found in Table B.3.

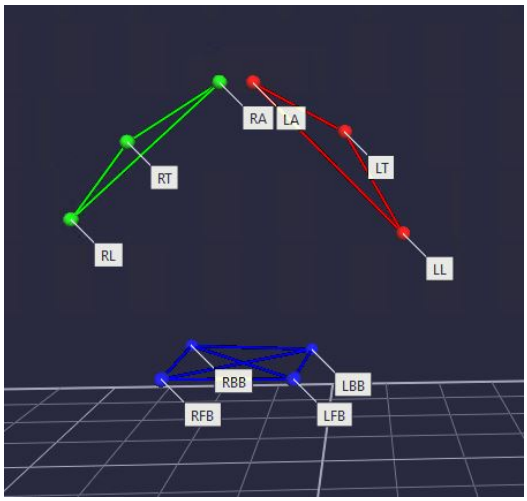

Figure B.15. Ophrie's skeleton template as captured by the camera system.

Table B.2. Marker notations for the custom build robot template that were used to record the links' positions and the robot's location.

Abbreviation	Marker notation
RA	Right (motor) Axis
RT	Right Top (the rotational joint between right proximal and distal links)
RL	Right Lower (parallel to the right proximal link)
LA	Left (motor) Axis
LT	Left Top(the rotational joint between left proximal and distal links)
LL	Left Lower (parallel to the left proximal link)
RFB	Right Forward (of the robot) Base (forward is towards handle)
RBB	Right Backward (of the robot) Base (backward is towards the motors)
LFB	Left Forward (of the robot) Base
LBB	Right Backward (of the robot) Base

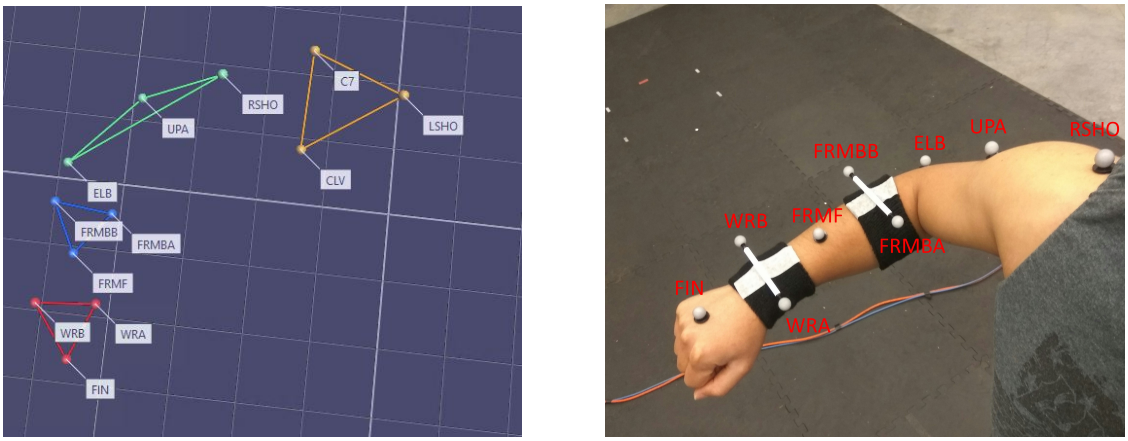

(a) (b)

Figure B.16. Right arm of the participant **(a)** captured by vicon camera system (custom arm template) **(b)** picture taken after the markers were attached to the subject.

Table B.3. Marker notations for the right arm template that was used to record the subject's right arm movement during the experiment that is reported in Paper IV.

Abbreviation	Marker notation
LSHO	Left SHOulder (on the right shoulder end of the clavicle bone)
C7	7^{th} Cervical – the largest and most inferior vertebra in the neck region
CLV	clavicle (upper end of the sternum)
RSHO	Right SHOulder
UPA	UPper Arm
ELB	Elbow (on the elbow axis)
FRMBB	FoRe arM Back B – pinky finger side
FRMBA	FoRe arM Back A – thumb finger side
FRMF	FoRe arM Front
WRB	WRist B – pinky finger side
WRA	WRist A – thumb finger side
FIN	FINger (on top of the hand)

BIBLIOGRAPHY

[1] Catani, M. and Dawson, M., 'Language processing, development and evolution,' in'Conn's transnational neuroscience,' pp. 679–692, Elsevier, 2017.

[2] Losee, R. M., 'Communication defined as complementary informative processes,'Journal of Information, Communication and Library Science, 1999, **5**(3), pp. 1–15.

[3] Hogan, N., Krebs, H. I., Charnnarong, J., Srikrishna, P., and Sharon, A., 'Mit-manus: a workstation for manual therapy and training ii,' in 'SPIE Applicationsin Optical Science and Engineering, Boston, MA, USA, March 26,' volume 1833, Telemanipulator Technology, 1993 pp. 28–34.

[4] Salisbury, J. K. and Srinivasan, M. A., 'Phantom-based haptic interaction with virtual objects,' IEEE Computer Graphics and Applications, September 1997, **17**(5), pp.6–10.

[5] Zwijgers, E.,The effect of partner performance on arm impedance modulation during haptic human-human interaction, Master's thesis, University of Twente, 2019.

[6] Reed, K. B. and Peshkin, M. A., 'Physical collaboration of human-human and human-robot teams,' IEEE Transactions on Haptics, July 2008, **1**(2), pp. 108–120.

[7] Stefanov, N., Peer, A., and Buss, M., 'Role determination in human-human interaction,'in 'World Haptics 2009-Third Joint Euro Haptics conference and Symposium on Haptic Interfaces for Virtual Environment and Teleoperator Systems, Slat Lake City, UT, USA, March 18-20,' IEEE, March 2009 pp. 51–56.

[8] Chen, T. L., Bhattacharjee, T., McKay, J. L., Borinski, J. E., Hackney, M. E., Ting,L. H., and Kemp, C. C., 'Evaluation by expert dancers of a robot that performs partnered stepping via haptic interaction,' PloS one, May 2015, **10**(5), p. e0125179.

[9] Mojtahedi, K., Whitsell, B., Artemiadis, P., and Santello, M., 'Communication and inference of intended movement direction during human–human physical interaction,' Frontiers in neurorobotics, 2017, **11**, p. 21.

[10] Takagi, A., Ganesh, G., Yoshioka, T., Kawato, M., and Burdet, E., 'Physically interacting individuals estimate the partner's goal to enhance their movements,' Nature Human Behaviour, 2017, **1**(3), pp. 1–6.

[11] Burdet, E., Tee, K. P., Mareels, I., Milner, T. E., Chew, C.-M., Franklin, D. W.,Osu, R., and Kawato, M., 'Stability and motor adaptation in human arm movements,'Biological cybernetics, 2006, **94**(1), pp. 20–32.

[12] Franklin, D. W., Liaw, G., Milner, T. E., Osu, R., Burdet, E., and Kawato, M.,'Endpoint stiffness of the arm is directionally tuned to instability in the environment,'Journal of Neuroscience, 2007, **27**(29), pp. 7705–7716.

[13] Franklin, D. W., Burdet, E., Tee, K. P., Osu, R., Chew, C.-M., Milner, T. E., and Kawato, M., 'Cns learns stable, accurate, and efficient movements using a simple algorithm,' Journal of neuroscience, 2008, **28**(44), pp. 11165–11173.

[14] Krutky, M. A., Trumbower, R. D., and Perreault, E. J., 'Effects of environmental instabilities on endpoint stiffness during the maintenance of human arm posture,' in'2009 Annual International Conference of the IEEE Engineering in Medicine and Biology Society,' IEEE, 2009 pp. 5938–5941.

[15] Kadiallah, A., Franklin, D. W., and Burdet, E., 'Generalization in adaptation to stable and unstable dynamics,' PLoS one, 2012, **7**(10), p. e45075.

[16] Regmi, S. and Song, Y. S., 'Design Methodology for Robotic Manipulator for Over-ground Physical Interaction Tasks,' Journal of Mechanism and Robotics, August 2020, **12**(4), p. 041002.

[17] Regmi, S. and Song, Y. S., 'Estimation of endpoint impedance of a 2d parallel manipulator using numerical simulation experiments,' in 'ASME International Mechanical Engineering Congress and Exposition,' volume **84522**, ASME, 2020 p.V005T05A066.

[18] Mussa-Ivaldi, F. A., Hogan, N., and Bizzi, E., 'Neural, mechanical, and geometric factors subserving arm posture in humans,' Journal of Neuroscience, 1985, **5**(10), pp.2732–2743.

[19] Regmi, S., Burns, D., and Song, Y. S.,'A Robot for Overground Physical Human-Robot Interaction Experiments,' Submitted to PLOS One.

[20] Regmi, S., Burns, D., and Song, Y. S., 'Humans Modulate Arm Stiffness to Facilitate Motor Communication during Overground Physical Interaction,' Manuscript in preparation.

[21] Rashid, F., Burns, D., and Song, Y. S., 'Sensing small interaction forces through proprioception,' Scientific Reports, 2021, **11**(1), pp. 1-10.

[22] Hammond, P., 'An experimental study of servo action in human muscular control,'in 'Proc III Int Conf Med Electron,' Institution of Electrical Engineers, 1960 pp. 190–199.

[23] Agarwal, G. C., Berman, B. M., and Stark, L., 'Studies in postural control systems part i: Torque disturbance input,' IEEE Transactions on Systems Science and Cybernetics, 1970, **6**(2), pp. 116–121.

[24] Wieneke, G. H. and van der Gon, J. D., 'Variations in the output impedance of the human motor system,' Kybernetik, 1974, **15**(3), pp. 159–178.

[25] Wadman, W. J., 'Control of fast goal-directed arm movements,' J. Human Movement Studies,1979, **5**, pp. 3–17.

[26] Cooke, J., 'Dependence of human arm movements on limb mechanical properties.'Brain Research, 1979.

[27] Bizzi, E., '7 central and peripheral mechanisms in motor control,' in 'Advances in psychology,' volume **1**, pp. 131–143, Elsevier, 1980.

[28] Fel'dman, A., 'Control of muscle length,' Biofizika, 1974, **19**(4), pp. 749–751.

[29] Fel'dman, A., 'Change of muscle length due to shift in the equilibrium points of the muscle load system,' Biofizika, 1974, **19**(4), pp. 534–538

[30] Abend, W., Bizzi, E., and Morasso, P., 'Human arm trajectory formation.' Brain: a journal of neurology, 1982, **105**(Pt 2), pp. 331–348.

[31] Vincken, M., Gielen, C., and van der Gon, J. D., 'Intrinsic and afferent components in apparent muscle stiffness in man,' Neuroscience, 1983, **9**(3), pp. 529–534.

[32] Bizzi, E., Kalil, R. E., and Tagliasco, V., 'Eye-head coordination in monkeys: evidence for centrally patterned organization,' Science, 1971, **173**(3995), pp. 452–454.

[33] Bizzi, E., Polit, A., and Morasso, P., 'Mechanisms underlying achievement of final head position,' Journal of neuro physiology, 1976, **39**(2), pp. 435–444.

[34] Feldman, A. G., 'Once more on the equilibrium-point hypothesis (λ model) for motor control,' Journal of motor behavior, 1986, **18**(1), pp. 17–54.

[35] Vincken, M., Gielen, C., and van der Gon, J. D., 'Stiffness control after fast goal-directed arm movements,' Human Movement Science, 1984, **3**(3), pp. 269–280.

[36] Hogan, N., 'The mechanics of multi-joint posture and movement control,' Biological cybernetics, 1985, **52**(5), pp. 315–331.

[37] Flash, T., 'The control of hand equilibrium trajectories in multi-joint arm movements,'Biological cybernetics, 1987, **57**(4), pp. 257–274.

[38] Dolan, J. M., Friedman, M. B., and Nagurka, M. L., 'A test-bed for measurement of human arm impedance parameters,' in '1990 IEEE International Conference on Systems Engineering,' IEEE, 1990 pp. 123–126.

[39] Dolan, J. M., Friedman, M. B., and Nagurka, M. L., 'Dynamic and loaded impedance components in the maintenance of human arm posture,' IEEE transactions on systems,man, and cybernetics, 1993, **(3)**, pp. 698–709.

[40] Tsuji, T., Goto, K., Moritani, M., Kaneko, M., and Morasso, P., 'Spatial characteristics of human hand impedance in multi-joint arm movements,' in 'Proceedings ofIEEE/RSJ International Conference on Intelligent Robots and Systems (IROS'94),' volume **1**, IEEE, 1994 pp. 423–430.

[41] Tsuji, T., Morasso, P. G., Goto, K., and Ito, K., 'Human hand impedance characteristics during maintained posture,' Biological cybernetics, 1995, **72**(6), pp. 475–485.

[42] Lacquaniti, F., Carrozzo, M., and Borghese, N., 'Time-varying mechanical behavior of multi-jointed arm in man,' Journal of neurophysiology, 1993, **69**(5), pp. 1443–1464.

[43] Bennett, D., Hollerbach, J., Xu, Y., and Hunter, I., 'Time-varying stiffness of human elbow joint during cyclic voluntary movement,' Experimental brain research, 1992, **88**(2), pp. 433–442.

[44] Milner, T. E., 'Dependence of elbow viscoelastic behavior on speed and loading involuntary movements,' Experimental Brain Research, 1993, **93**(1), pp. 177–180.

[45] Bennett, D. J., 'Torques generated at the human elbow joint in response to constant position errors imposed during voluntary movements,' Experimental Brain Research, 1993, **95**(3), pp. 488–498.

[46] Gomi, H. and Kawato, M., 'Human arm stiffness and equilibrium-point trajectory during multi-joint movement,' Biological cybernetics, 1997, **76**(3), pp. 163–171.

[47] Burdet, E., Osu, R., Franklin, D., Yoshioka, T., Milner, T., and Kawato, M., 'A method for measuring endpoint stiffness during multi-joint arm movements,' Journal of biomechanics, 2000, **33**(12), pp. 1705–1709.

[48] Gomi, H. and Osu, R., 'Task-dependent viscoelasticity of human multijoint arm and its spatial characteristics for interaction with environments,' Journal of neuroscience,1998, **18**(21), pp. 8965–8978.

[49] Rahman, M., Ikeura, R., and Mizutani, K., 'Control characteristics of two humans in cooperative task and its application to robot control,' in '2000 26th Annual Conference of the IEEE Industrial Electronics Society. IECON 2000. 2000 IEEE International Conference on Industrial Electronics, Control and Instrumentation. 21st Century Technologies,' volume **3**, IEEE, 2000 pp. 1773–1778.

[50] Burdet, E., Osu, R., Franklin, D. W., Milner, T. E., and Kawato, M., 'The central nervous system stabilizes unstable dynamics by learning optimal impedance,' Nature,2001, **414**(6862), pp. 446–449.

[51] Selen, L. P., Beek, P. J., and Van Dieën, J. H., 'Impedance is modulated to meet accuracy demands during goal-directed arm movements,' Experimental Brain Research, 2006, **172**(1), pp. 129–138.

[52] Takagi, A., Xiong, G., Kambara, H., and Koike, Y., 'Endpoint stiffness magnitude increases linearly with a stronger power grasp,' Scientific Reports, 2020, **10**(1), pp.1–9.

[53] Tee, K. P., Burdet, E., Chew, C. M., and Milner, T. E., 'Investigating motor adaptation to stable and unstable tasks using haptic interfaces, emg and fmri,' in 'SICE 2003 Annual Conference (IEEE Cat. No. 03TH8734),' volume **1**, IEEE, 2003 pp. 591–595.

[54] Tee, K. P., Burdet, E., Chew, C.-M., and Milner, T. E., 'A model of force and impedance in human arm movements,' Biological cybernetics, 2004, **90**(5), pp. 368–375.

[55] Hu, X., Murray, W. M., and Perreault, E. J., 'Biomechanical constraints on the feed-forward regulation of endpoint stiffness,' Journal of neurophysiology, 2012, **108**(8), pp. 2083–2091.

[56] Berret, B. and Jean, F., 'Stochastic optimal open-loop control as a theory of force and impedance planning via muscle co-contraction,' PLoS computational biology, 2020, **16**(2), p. e1007414.

[57] Artemiadis, P. K., Katsiaris, P. T., Liarokapis, M. V., and Kyriakopoulos, K. J., 'Human arm impedance: Characterization and modeling in 3d space,' in '2010 IEEE/RSJ International Conference on Intelligent Robots and Systems,' IEEE, 2010 pp. 3103–3108.

[58] Wu, M., Drnach, L., Bong, S. M., Song, Y. S., and Ting, L. H., 'Human-human and interactions aid balance during walking by haptic communication,' Frontiers in Robotics and AI, 2021, **8**.

[59] Piovesan, D., Pierobon, A., DiZio, P., and Lackner, J. R., 'Experimental measure of arm stiffness during single reaching movements with a time-frequency analysis,' Journal of neurophysiology, 2013, **110**(10), pp. 2484–2496.

[60] van de Ruit, M., Cavallo, G., Lataire, J., Van Der Helm, F. C., Mugge, W., van Wingerden, J.-W., and Schouten, A. C., 'Revealing time-varying joint impedance with kernel-based regression and non-parametric decomposition,' IEEE Transactions on Control Systems Technology, 2018, **28**(1), pp. 224–237.

[61] Feth, D., Groten, R., Peer, A., Hirche, S., and Buss, M., 'Performance related energy exchange in haptic human-human interaction in a shared virtual object manipulation task,' in 'World Haptics 2009-Third Joint Euro Haptics conference and Symposium

on Haptic Interfaces for Virtual Environment and Teleoperator Systems, Slat Lake City, UT, USA , March 18-20,' IEEE, March 2009 pp. 338–343.

[62] Sawers, A., Bhattacharjee, T., McKay, J. L., Hackney, M. E., Kemp, C. C., and Ting,L. H., 'Small forces that differ with prior motor experience can communicate movement goals during human-human physical interaction,' Journal of neuroengineering and rehabilitation, January 2017, **14**(1), p. 8.

[63] Sylos-Labini, F., d'Avella, A., Lacquaniti, F., and Ivanenko, Y., 'Human-human interaction forces and inter limb coordination during side-by-side walking with hand contact,' Frontiers in physiology, March 2018,**9**, p. 179.

[64] Hogan, N., 'Impedance control: An approach to manipulation: Part I Theory; part II Implementation; part III Applications,' ASME Journal of Dynamic Systems, Measurement, and Control, March 1985, **107**(1), pp. 1–24.

[65] Hogan, N., 'Stable execution of contact tasks using impedance control,' in 'Proceedings International Conference on Robotics and Automation, Raleigh, N.C, USA, March 31-April 3,' volume **4**, IEEE, Raleigh, N.C, USA, March 31-April 3 1987 pp.1047–1054.

[66] Massie, T. H., Salisbury, J. K.,et al., 'The phantom haptic interface: A device for probing virtual objects,' in 'Proceedings of the ASME winter annual meeting, symposium on haptic interfaces for virtual environment and teleoperator systems, Chicago, IL, USA, November,' volume **55**, Citeseer, 1994 pp. 295–300.

[67] Scott, S. H., 'Apparatus for measuring and perturbing shoulder and elbow joint positions and torques during reaching,' Journal of neuroscience methods, July 1999, **89**(2), pp. 119–127.

[68] Ajoudani, A., Fang, C., Tsagarakis, N., and Bicchi, A., 'Reduced-complexity representation of the human arm active endpoint stiffness for supervisory control of remote manipulation,' The International Journal of Robotics Research, 2018, **37**(1), pp. 155–167.

[69] Wang, Z., Yuan, J., and Buss, M., 'Modeling of human haptic skill: A framework and preliminary results,' in 'Proceedings of the 17th IFAC World Congress, Seoul, Korea, July 6-11,' volume **41**, 2008 pp. 14761–14766.

[70] Fayé, I. C., An impedance controlled manipulandum for human movement studies, Ph.D. thesis, Massachusetts Institute of Technology, 1986.

[71] Franklin, D. W., So, U., Burdet, E., and Kawato, M., 'Visual feedback is not necessary for the learning of novel dynamics,' PloS one, 2007, **2**(12), p. e1336.

[72] Ganesh, G., Takagi, A., Osu, R., Yoshioka, T., Kawato, M., and Burdet, E., 'Two is better than one: Physical interactions improve motor performance in humans,' Scientific reports, 2014, **4**(1), pp. 1–7.

[73] Beckers, N., van Asseldonk, E. H., and van der Kooij, H., 'Haptic human–human interaction does not improve individual visuomotor adaptation,' Scientific reports, 2020, **10**(1), pp. 1–11.

VITA

Sambad Regmi was born in Baglung, Nepal. After completing high school from Kathmandu, Nepal, he got selected to study Bachelor of Engineering with a full scholarship through an open competition under the Government of India-sponsored Nepal Aid Fund Scholarship Scheme 2012-13. He received his Bachelor of Engineering degree in Mechanical Engineering from Visvesvaraya Technological University, Karnataka, India, in 2016.

In Fall 2017, Sambad joined the Mechanical and Aerospace Engineering Department at Missouri University of Science and Technology (Missouri S&T), Rolla, MO. He worked as a graduate research assistant and a graduate teaching assistant. He received his Ph.D. degree in Mechanical Engineering from Missouri S&T in May 2022 for his work on "Development of an Interactive Robot for Overground Physical Human-Robot Interaction". He performed his research at the physical human-robot interaction (pHRI) laboratory in a group under the guidance of Dr. Yun Seong Song. His research focused on advancing human-robot interaction, neuromechanics, and robotics.

While at Missouri S&T, Sambad had contributed to the publication of three journal paper, and had presented his research work at the 41st Annual International Conference of the IEEE Engineering in Medicine and Biology Society held in July 2019 in Berlin, Germany, and at ASME 2020 International Mechanical Engineering Congress and Exposition (virtual) held in November 2020. In Fall 2020, he was awarded the John W. Claypool fund for medical research from the office of vice-chancellor of research at Missouri S&T. In Fall 2021, he presented a summary of his Ph.D. research at 3 Minutes Poster Presentation organized by the council of graduate studies at Missouri S&T and was awarded 5th place for the best presentation. In Spring 2022, he presented an overview of his research work at the 3MT competition organized by Missouri S&T and received the people's choice award.